

AFIT/GE/ENG/95M-02



Investigation of Ground Target Detection Methods  
in Fully Polarimetric Wide Angle  
Synthetic Aperture Radar Images

THESIS  
Wayne B. McLaggan  
Flight Lieutenant, Royal Australian Air Force

AFIT/GE/ENG/95M-02

Approved for public release; distribution unlimited

19950503 127

AFIT/GE/ENG/95M-02

Investigation of Ground Target Detection Methods  
in Fully Polarimetric Wide Angle  
Synthetic Aperture Radar Images

THESIS

Presented to the Faculty of the Graduate School of Engineering  
of the Air Force Institute of Technology  
Air University  
In Partial Fulfillment of the  
Requirements for the Degree of  
Master of Science in Electrical Engineering

Wayne B. McLaggan, B.Eng  
Flight Lieutenant, Royal Australian Air Force

March, 1995

Accession For	
NTIS	<input checked="checked" type="checkbox"/>
CRA&I	<input type="checkbox"/>
DTIC	<input type="checkbox"/>
TAB	<input type="checkbox"/>
Unannounced	<input type="checkbox"/>
Justification _____	
By _____	
Distribution /	
Availability Codes	
Dist	Avail and/or Special
A-1	

Approved for public release; distribution unlimited

### *Acknowledgements*

There are many people to thank for their patience, support and knowledge, without whom this research would not have been possible.

To my wife, Mandy, thank you for your love, support and hard work over the last 22 months. To my children, Leona and Matthew thank you for your understanding, and patience.

To my thesis advisor, Captain Joe Sacchini, thank you for your enthusiasm, motivation and guidance.

To Patti Ryan (WL-AARA) thank you for providing the data.

To the *Comm Guys*, Gerry Falen, Richard Sumner, Jeff Gay, Roger Claypoole, Rob Garza, Chris Eisenbies, David Jennings and Dan Zahirniak whose friendship and teamwork made this a great experience. Thanks for the memories.

Finally, to the Royal Australian Air Force my appreciation of the great opportunity afforded me.

Wayne B. McLaggan

## *Table of Contents*

	Page
Acknowledgements . . . . .	ii
List of Figures . . . . .	vii
List of Tables . . . . .	xi
List of Abbreviations . . . . .	xii
Abstract . . . . .	xiii
I. Introduction . . . . .	1
1.1 Background . . . . .	1
1.1.1 Polarimetric Processing . . . . .	3
1.1.2 Multiple Image Processing . . . . .	4
1.2 Problem and Objectives . . . . .	6
1.3 Scope . . . . .	6
1.4 Assumptions . . . . .	7
1.5 Thesis Organization . . . . .	7
II. Theory and Data Generation . . . . .	8
2.1 Overview . . . . .	8
2.2 Polarimetric Theory . . . . .	8
2.3 Polarimetric Algorithms . . . . .	11
2.3.1 Metrics . . . . .	11
2.3.2 Polarimetric Average . . . . .	13
2.3.3 Polarimetric Span . . . . .	13
2.3.4 Polarimetric Whitening Filter (PWF) . . . . .	13
2.3.5 Polarimetric Optimal Weighting (POW) . . . . .	15

	Page
2.3.6 The Polarimetric Matched Filter (PMF) . . . . .	15
2.4 Multiple Aspect Angle Algorithms . . . . .	16
2.4.1 WASAR Average . . . . .	18
2.4.2 WASAR Whitening Filter (WWF) . . . . .	19
2.4.3 Adaptive WASAR Whitening Filter (AWWF) . . . . .	20
2.4.4 WASAR Matched Filter (WMF) . . . . .	22
2.4.5 Combinations of Polarimetric and Wide Angle Algorithms	22
2.5 Target Detection Theory . . . . .	23
2.6 Statistical Analysis of Clutter and Targets . . . . .	29
2.6.1 Gaussian Distribution . . . . .	30
2.6.2 Gamma Distribution . . . . .	30
2.6.3 Weibull Distribution . . . . .	30
2.6.4 Rayleigh Distribution . . . . .	31
2.6.5 Log-Normal Distribution . . . . .	31
2.7 Method of Determining the Distribution of Target and Clutter Pixel Intensities . . . . .	32
2.8 Data Generation and Rotation . . . . .	32
2.9 Summary . . . . .	36
III. Statistical Analysis of XPATCH-ES Data and Clutter Models . . . . .	39
3.1 Introduction . . . . .	39
3.2 Statistical Analysis of Data . . . . .	39
3.2.1 Determining Target and Clutter Distributions . . . . .	40
3.2.2 Estimates of the Mean and Standard Deviation of Pixel Intensities . . . . .	43
3.2.3 Standard Deviation to Mean (S/M) Ratios . . . . .	43
3.2.4 Target to Clutter (T/C) Ratios . . . . .	44
3.2.5 Target and Clutter Polarimetric and Wide Angle Covari- ance Matrices . . . . .	44

	Page
3.2.6 Summary of Statistical Analysis . . . . .	54
3.3 Feature Extraction . . . . .	54
3.3.1 Discriminator and Specific Features Investigated . . . . .	56
3.4 Target and Clutter Analysis . . . . .	62
3.4.1 Polar Plots of Targets and Clutter . . . . .	62
3.4.2 Target and Terrain Clutter Analysis . . . . .	63
3.4.3 2-D Correlation analysis . . . . .	65
3.4.4 ROC Curves . . . . .	67
3.5 Clutter Models . . . . .	70
3.5.1 Clutter Model Theory . . . . .	70
3.5.2 Gaussian Clutter Generator . . . . .	72
3.5.3 Rayleigh Clutter Generator . . . . .	73
3.5.4 Weibull Clutter Generator . . . . .	80
3.6 Summary . . . . .	81
IV. Results . . . . .	83
4.1 Polarimetric Processing . . . . .	83
4.1.1 Polarimetric Data Set 1 . . . . .	85
4.1.2 Polarimetric Data Set 2 . . . . .	89
4.1.3 Polarimetric Data Set 3 . . . . .	95
4.1.4 Polarimetric Data Set 4 . . . . .	100
4.1.5 Target Detection of Polarimetric Algorithms . . . . .	104
4.1.6 Discussion of Polarimetric Processing . . . . .	107
4.2 Wide Angle Processing . . . . .	110
4.2.1 Wide Angle Data Set 1 . . . . .	111
4.2.2 Wide Angle Data Set 2 . . . . .	112
4.2.3 Wide Angle Data Set 3 . . . . .	118
4.2.4 Summary of Wide Angle Processing . . . . .	122

	Page
4.3 Comparison of Polarimetric and Wide Angle Processing . . . . .	126
4.4 Combination of Polarimetric and Wide Angle Algorithms . . . . .	128
4.5 Summary . . . . .	132
V. Conclusion and Recommendations . . . . .	135
5.1 Introduction . . . . .	135
5.2 Summary of Results . . . . .	135
5.2.1 Statistical Analysis . . . . .	135
5.2.2 Feature Extraction . . . . .	136
5.2.3 Clutter Models . . . . .	136
5.2.4 Polarimetric Processing . . . . .	136
5.2.5 Wide Angle Processing . . . . .	136
5.2.6 Combinations of Polarimetric and Wide Angle Algorithms	137
5.3 Conclusion . . . . .	137
5.4 Recommendations for Future Research . . . . .	138
Appendix A. Matlab Code . . . . .	140
Bibliography . . . . .	159
Vita . . . . .	161

## *List of Figures*

Figure	Page
1. SAR Image Formation . . . . .	2
2. Wide Angle SAR Image Formation . . . . .	3
3. Generation of AWWF Image . . . . .	21
4. Two methods of combining WASAR Polarimetric images (a) Combining all aspect angles and polarizations, (b) Combining Polarizations and then combining these images at the different aspect angles using either WWF or AWWF algorithms. . . . .	23
5. Probability of Detection and False Alarm . . . . .	26
6. Receiver Operating Characteristics (ROC curves) . . . . .	27
7. Reference Window of two parameter CFAR detector . . . . .	28
8. Example of pdf curve fitting to determine the distribution of targets and clutter (a) Gaussian distributed random variable (b) Rayleigh distributed random variable. . . . .	33
9. Data Set 1 Before Rotation . . . . .	34
10. Overlap of Rotated Image . . . . .	35
11. Data Set 1 After Rotation . . . . .	37
12. Legend of typical items in a target scene. . . . .	38
13. Ground truth map for Data Set 1 (6 targets). . . . .	38
14. Histograms of clutter pixel intensities. (a) Data Set 1, and (b) Data Set 2. . . . .	41
15. Histograms of the target pixel intensities. (a) Data Set 1, and (b) data Set 2. . . . .	42
16. Target and clutter pdfs for: (a) Data Set 1, and (b) Data Set 2. . . . .	42
17. Images of Specific Terrain Features: a) Target, b) Trees, and c) Grass . . . . .	47
18. Plot of Relative Return versus Aspect Angle for Targets, Trees and Grass . . . . .	52
19. Block diagram of fully polarimetric WARSAR target detection system . . . . .	55
20. Block diagram of $\rho_{hh-hv}$ standard deviation discriminator . . . . .	57
21. Binary images of: a) HH -45°, and b) Target used for testing in feature extraction . . . . .	58



Figure		Page
22.	Diagram of simple Discriminator . . . . .	59
23.	Discrimination of targets and clutter using the standard deviation and mean features. a) Image of a target in clutter, b) Plot of Mean vs STD . . . . .	60
24.	Feature plots (a) STD Vs Mean, (b) 2-D Corr Coefficient Vs Mean, (c) 2-D Corr Coefficient Vs STD , and (d) HH-HV Corr Coefficient Vs STD. . . . .	61
25.	Polar Plots of Targets in Data Set 1 . . . . .	64
26.	Polar plot of Clutter Pixels . . . . .	65
27.	Terrain Clutter and Target analysis for: a) Target, b) Targets, c) Trees, and d) Ground Clutter. . . . .	66
28.	2-D Correlation analysis for: a) Target, b) Target plus Tree, c) Trees, and d) Ground Clutter. . . . .	68
29.	2-D Correlation analysis for a single tree . . . . .	69
30.	Plots of ROC curves for Data Set 1 . . . . .	71
31.	Clean Images of T-72 Tank (a) HH, (b) VV (c) VH . . . . .	74
32.	Noisy Images of T-72 Tank (a) HH, (b) VV (c) VH. . . . .	74
33.	Histograms of pixel intensities for: (a) XPATCH-ES Clutter, and (b) Generated Clutter. . . . .	76
34.	Images and Correlation Plots: (a) XPATCH-ES clutter scene (b) Pixel to Pixel correlation, (c) Generated clutter scene , and (d) Pixel to Pixel correlation. . . . .	79
35.	Simple Schematic of a Filter . . . . .	80
36.	a) Image of Generated Weibull clutter, and b) Histogram of Pixels . . . . .	82
37.	Images of: (a) Polarimetric Data Set 1, and (b) Polarimetric Data Set 2 . . . . .	86
38.	Polarimetric Images Polarimetric Data Set 4 (AFITF1000D45 data set): (a) HH, (b) HV, (c) VV, and (d) Ground truth map. . . . .	87
39.	Clutter Pdfs of Polarimetric Data Set 1: (a) $ HH ^2$ , (b) Average, (c) Span, (d) POW, and (e) PWF. . . . .	88
40.	Target and Clutter Pdfs of Data Set 2: (a) $ HH ^2$ , (b) Average, (c) Span, (d) POW, (e) PMF, and (f) PWF. . . . .	92

Figure	Page
41. ROC curves for Polarimetric Data Set 2: (a) $ HH ^2$ (b) Average, (c) Span, (d) POW, (e) PMF, and (f) PWF. . . . .	93
42. Discriminator Results for Polarimetric Data Set 2: (a) $ HH ^2$ (b) Average, (c) Span, (d) POW, (e) PMF, and (f) PWF. . . . .	94
43. Combined Polarimetric Images of Data Set 3 using the: (a) $ HH ^2$ (b) Average, (c) Span, (d) POW, (e) PMF, and (f) PWF. . . . .	96
44. Target and Clutter Pdfs of Data Set 3: (a) $ HH ^2$ , (b) Average, (c) Span, (d) POW, (e) PMF, and (f) PWF. . . . .	98
45. ROC curves for Polarimetric Data Set 3: (a) $ HH ^2$ (b) Average, (c) Span, (d) POW, (e) PMF, and (f) PWF. . . . .	99
46. Discriminator Results for Polarimetric Data Set 3: (a) $ HH ^2$ (b) Average, (c) Span, (d) POW, (e) PMF, and (f) PWF. . . . .	101
47. Combined Polarimetric Images of Polarimetric Data Set 4 using: (a) $ HH ^2$ , (b) Average, (c) Span, (d) POW, (e) PMF, and (f) PWF. . . . .	102
48. Target and Clutter Pdfs of Data Set 4: (a) $ HH ^2$ , (b) Average, (c) Span, (d) POW, (e) PMF, and (f) PWF. . . . .	103
49. ROC curves for Polarimetric Data Set 4: (a) $ HH ^2$ (b) Average, (c) Span, (d) POW, (e) PMF, and (f) PWF. . . . .	105
50. Discriminator Results for Polarimetric Data Set 4: (a) $ HH ^2$ (b) Average, (c) Span, (d) POW, (e) PMF, and (f) PWF. . . . .	106
51. Target detection performance of polarimetric Data Set 3 using a constant threshold for: (a) HH , (b) Average, (c) Span, (d) POW, (e) PMF and (f) PWF. . . . .	108
52. Target detection performance of Data Set 3 using a constant threshold for: (a) HH , (b) Average, (c) Span, (d) POW, (e) PMF, and (f) PWF. . . . .	109
53. Images of: (a) $ HH ^2$ $0^\circ$ , and (b) AWWF (10 x 10 pixels) . . . . .	113
54. Target and Clutter Pdfs of Wide Angle Data Set 2: (a) $ HH ^2 + 15^\circ$ , (b) Average, (c) WWF, (d) AWWF (20 x 20) pixels, and (e) AWWF (10 x 10 pixels). . . . .	115
55. ROC curves for Wide Angle Data Set 2: (a) $ HH ^2 + 15^\circ$ (b) Average, (c) WWF, (d) AWWF (20 x 20 pixels), (e) AWWF (10 x 10 pixels) Filter. . .	116

Figure	Page
56. Discriminator Results for Polarimetric Data Set 4: (a) $ HH ^2$ (b) Average, (c) WWF (d) AWWF (20 x20 pixels), and (e) AWWF (10 x 10 pixels) . .	117
57. Plot of Window Size versus T/C Ratio . . . . .	120
58. Combined Wide Angle Images of Data Set 3 using the: (a) $ HH ^2$ 0°(b) Average, (c) WWF, (d)AWWF (30 x 30 pixels), and (e) AWWF (10 x 10 pixels). . . . .	121
59. Target and Clutter Pdfs of Wide Angle Data Set 3: (a) $ HH ^2 +15^\circ$ , (b) Average, (c) WWF, (d) AWWF (30 x 30) pixels, and (e) AWWF (10 x 10 pixels). . . . .	123
60. ROC curves for Wide Angle Data Set 3: (a) $ HH ^2 +15^\circ$ (b) Average, (c) WWF, (d) AWWF (30 x 30 pixels), (e) AWWF (10 x 10 pixels) Filter. . .	124
61. Discriminator Results for Polarimetric Data Set 3: (a) $ HH ^2$ (b) Average, (c) Span, (d) Optimal Weighting, (e) Polarimetric Matched Filter, and (f) Polarimetric Whitening Filter. . . . .	125
62. ROC curves of AWWF, WWF, PWF and $ HH ^2 +15^\circ$ . . . . .	126
63. Direct Comparison of Wide Angle and Polarimetric Algorithms . . . . .	128
64. Images formed from Algorithms: (a) Unprocessed HH -45°, (b) 1, (c) 2, and (d) 3. . . . .	130
65. Images formed from Algorithms: (a) 4, (b) 5, (c) 6, and (d) 7. . . . .	131
66. ROC Curves for: (a) Algorithms 1, 2, 3 and 4, (b) Algorithms 5, 6 and 7 (c) Comparison between best unprocessed image ( $ HH ^2$ 0°) and Algorithm 7	133

# *List of Tables*

Table	Page
1. Sample Estimates of Target and Clutter Means and STDs for both Data Sets	43
2. S/M Ratios for Data Set 1 . . . . .	44
3. T/C Ratios for Data Set 1 (dB) . . . . .	44
4. Correlation coefficients between polarizations . . . . .	46
5. Correlation coefficients between polarizations for Targets, Trees and Grass	49
6. Correlation coefficients between aspect angles for Clutter plus targets (whole image) . . . . .	51
7. Correlation coefficients between aspect angles for Targets only . . . . .	53
8. Correlation coefficients between aspect angles for Trees only . . . . .	53
9. Correlation coefficients between aspect angles for Grass only . . . . .	53
10. Correlation coefficients between polarizations XPATCH-ES Clutter . . . . .	77
11. S/M ratios for polarimetric Data Set 1 . . . . .	87
12. S/M and T/C ratios for Polarimetric Data Set 2 . . . . .	90
13. S/M and T/C ratios Polarimetric Data Set 3 . . . . .	97
14. S/M and T/C ratios Polarimetric Data Set 4 . . . . .	100
15. S/M ratios for Wide Angle Data Set 1 . . . . .	111
16. S/M and T/C ratios Wide Angle Data Set 2 . . . . .	113
17. S/M and T/C ratios for Wide Angle Data Set 3 . . . . .	119
18. T/C ratios for seven different polarimetric data sets . . . . .	127
19. T/C ratios for wide angle aspect angle combinations . . . . .	127
20. T/C ratios (dB) for the Seven Polarimetric and Wide Angle Combining Algorithms . . . . .	132

# *List of Abbreviations*

Abbreviation	Page
WASAR Wide Angle Synthetic Aperture Radar . . . . .	1
SAR Synthetic Aperture Radar . . . . .	1
S/M Standard Deviation to Mean Ratio . . . . .	12
T/C Target to Clutter Ratio . . . . .	12
PUF Polarimetric Whitening Filter . . . . .	13
HH Horizontal Transmit - Horizontal Receive . . . . .	15
VV Vertical Transmit - Vertical Receive . . . . .	15
HV Horizontal Transmit - Vertical Receive . . . . .	15
PMF Polarimetric Matched Filter . . . . .	15
POW Polarimetric Optimally Weighted . . . . .	16
AWWF Adaptive WASAR Whitening Filter . . . . .	16
WWF WASAR Whitening Filter . . . . .	19
WMF WASAR Matched Filter . . . . .	22
PUT Pixel Under Test . . . . .	24
ROC Receiver Operating Characteristic . . . . .	26
CFAR Constant False Alarm Rate . . . . .	27
PCM Polarimetric Covariance Matrix . . . . .	47
WACM Wide Angle Covariance Matrix . . . . .	49

*Abstract*

Target detection is a high priority of the Air Force for the purpose of reconnaissance and bombardment. This research investigates and develops methods to distinguish ground targets from clutter (i.e. foliage, landscape etc.) in Wide Angle Synthetic Aperture Radar (WASAR) images. WASAR uses multiple aspect angle SAR images of the same target scene. The WASAR data was generated from a pre-release software package (XPATCH-ES) provided by the sponsor (WL-AARA). A statistical analysis and feature extraction is performed on the XPATCH-ES data. This analysis showed that the standard deviation of *target* pixel intensities is significantly higher than for *clutter*. Using this feature and a 2-D correlation coefficient a simple discriminator that effectively separates targets from clutter false alarms is presented. Polarimetric and wide angle covariance matrices are estimated and analyzed. From an analysis of the wide angle covariance matrix it is shown that natural clutter has in general a uniform radar return for changing aspect angles, whereas the radar return for a target varies. That is, trees and ground clutter *look* the same at different angles whereas targets *look* considerably different at even small changes in aspect angle. Based on this analysis, two new wide angle algorithms, the WASAR Whitening Filter and the Adaptive WASAR Whitening Filter (AWWF) are developed. The target detection performance of polarimetric and multi aspect angle image combining algorithms are quantified using Receiver Operating Characteristic curves and target to clutter ratios. It is shown that wide angle processing provides superior target detection performance over polarimetric processing. In particular the AWWF algorithm provided

a 2-3 dB improvement in target to clutter ratio than polarimetric techniques such as the Polarimetric Whitening Filter. Combinations of wide angle and polarimetric algorithms were used to achieve a 13.7 dB processing gain in target to clutter ratio when compared to unprocessed images of the target scene. This represents a significant improvement in target detection capabilities.

Investigation of Ground Target Detection Methods  
in Fully Polarimetric Wide Angle  
Synthetic Aperture Radar Images

*I. Introduction*

The detection and identification of military targets are important Air Force missions. Synthetic Aperture Radar (SAR) images have been used extensively for the purposes of military target detection. Recently, the Gulf War highlighted: (a) the need for efficient target detection algorithms (e.g. detection of Scud missile launchers); and, (b) the success of the J-STARS system (which uses SAR). The sponsor of this research, Air Force Wright Laboratories (WL-AARA), is especially concerned with evaluating the advantages of using Wide Angle Synthetic Aperture Radar (WASAR) multiple images and, for this reason, this research was commissioned to develop and quantify the effectiveness of target detection algorithms using fully polarimetric WASAR images.

*1.1 Background*

Synthetic Aperture Radar (SAR) is used to form map-like images of the earth's surface. SAR is operated from a moving platform such as an aircraft or a satellite and the motion of the platform is used to synthesize the effect of a large antenna aperture. An image of the earth's surface, i.e. a target scene, is formed by digital signal processing algorithms contained within the SAR. Figure 1 is a simple schematic of the operation



of a SAR from an aircraft. This figure demonstrates how the ground (target scene) is illuminated with electromagnetic energy, and the scattering of this energy returned to the radar is used to form an image of the earth's surface.

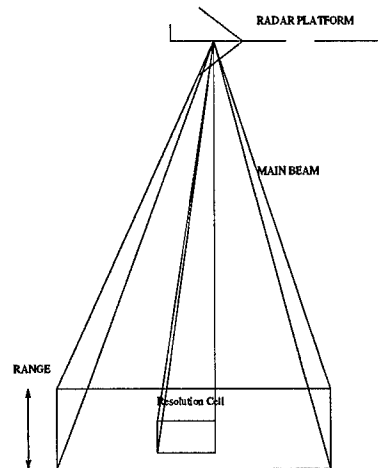


Figure 1. SAR Image Formation

A standard SAR provides only one image of the target scene from a particular aspect angle. Fully polarimetric SAR imaging, as described in [8, 24, 1], improves on this ability as it produces three images of the target scene, at the one aspect angle, by illuminating the scene with electromagnetic waves at three different polarizations. The three fully polarimetric radar returns are the: HH, HV, and VV. The HH is so named because it illuminates the scene with horizontally polarized waves and the returns are detected with a horizontally polarized antenna. Similarly, the HV signal is transmitted horizontally but received vertically; and the VV is transmitted vertically and received vertically. Fully polarimetric processing (the combination of the images produced by each polarization) shall be discussed in the following section.

Target detection capabilities could be further improved by using a fully polarimetric Wide-Angle SAR (WASAR). WASAR offers multiple images of a single target scene at different aspect angles and polarizations (as shown in Figure 2). For example, a target scene illuminated by a fully polarimetric WASAR from aspect angles of  $\pm 45^\circ$  and  $0^\circ$ ; would produce nine images. Unfortunately, WASAR is now in the early stages of the conceptual system design phase. Accordingly, one of the objectives of this research is to prove the value of WASAR and investigate its operational feasibility. The Air Force Institute of Technology (AFIT) has begun research into target detection using WASAR data. Research by Knurr [11] and Sumner [25] proved that target detection performance is enhanced by using fully polarimetric images from multiple aspect angles. Further, their research recommended continuing work in this area, specifically in statistically analyzing and developing algorithms to combine the fully polarimetric, multi-aspect angle images.

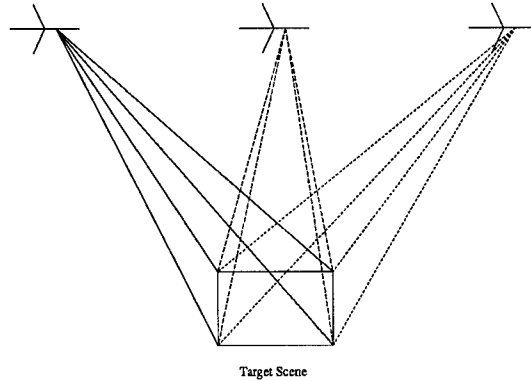


Figure 2. Wide Angle SAR Image Formation

*1.1.1 Polarimetric Processing.* Polarimetric processing is a means of optimally combining the HH, HV and VV images in order to improve target detection. Targets and clutter have differing geometrical characteristics leading to differing electromagnetic signatures. With the proper polarimetric processing, the radar return from clutter and

target can be more easily distinguished from each other [9]. Further, a complex target can be considered as comprising a multitude of independent objects that scatter energy in all directions [23]. Accordingly, the target may provide a stronger radar return or ‘*glint*’ at a different polarization. Gaussian clutter models, which characterize homogeneous clutter regions have been developed by Novak [15]. These algorithms use fully polarimetric data and optimally combine the HH, HV and VV images in some sense. In particular, the polarimetric algorithms presented by Novak include: the polarimetric span of the three complex elements (HH, HV and VV); the Polarimetric Whitening Filter (PWF); the Polarimetric Matched Filter (PMF); and the Polarimetric Optimal Weighted (POW) sum of intensities. These algorithms were developed by analyzing the covariance matrix of the polarimetric data, which characterizes the relationship between the radar returns at different polarizations. Non-Gaussian clutter models have been developed in a similar manner by Lee [12], Oliver [18] and Jakeman [10].

*1.1.2 Multiple Image Processing.* Multiple image processing is a means of combining the images taken at different aspect angles to further improve target detection. The multiple images are compared by a change detection algorithm which compares data from two or more co-registered images and looks for differences. These images are generally obtained by using multiple flight passes to image the target scene at different times. One example of a two pass change detection algorithm is presented by Li [13]. The major disadvantage of the two pass imaging method is the large variance in the target’s signature in the two images. This is caused because the aircraft cannot fly exactly the same flight path on its second pass. Therefore, targets seen in each image are not exactly correlated

on a pixel to pixel basis. Hence, the combined target's signal power is lower than if the two images were perfectly aligned. Other disadvantages with the two pass multiple image method arise in a hostile environment when: a) an aircraft may not get the chance to make a second flight over enemy territory; and b) mobile targets such as scud missile launchers could be moved prior to the second flight.

An alternative method for obtaining multiple images with a single flyover is proposed by Halverson [7]. His technique utilizes change detection algorithms to exploit differences in aspect angle dependency between target scatters and clutter scatters. The multiple images are formed from a single flight pass of a target scene that is imaged from several aspect angles. Early results of this research have shown comparable performance to that achieved by two pass change detection using co-registered images. Another two multiple image processing detection algorithms, to enhance stationary target detection, have been developed by Sechtin [21].

In Sechtin's first model, detection algorithms are applied to the individual images and then the detections are combined by forming a detection list for all the images in the data set. A target is declared in a region if a certain number of the individual image detection lists contain similar information. In the second model, the images are combined and then the detection algorithms are applied to the combined image. However, because of difficulties in collecting a sufficient amount of clutter data some of Sechtin's results are inconclusive. Overall, current research indicates that multiple aperture detection algorithms show great promise for the detection of stationary targets embedded in clutter.

### 1.2 Problem and Objectives

At this stage WASAR is a theoretical proposition. The main purpose of this research is to enhance our ability to detect a target by investigating target detection techniques using: fully polarimetric SAR images; multiple aspect angle (multi-look) SAR images (WASAR); and a combination of both.

In particular, the objectives of this research are as follows:

1. Generate SAR data sets which include clutter and ground targets using a computer code provided by the sponsor and written by Loral.
2. Examine/develop various detection techniques and evaluate their applicability to the SAR data sets.
3. Apply these techniques to the SAR data and determine their performance.
4. Justify the feasibility of WASAR based on the research results.

### 1.3 Scope

The scope of this research is confined to the list of tasks given in Section 1.2 Problem and Objectives. Within these bounds, clutter models of various statistics are developed to assist with the understanding and development of algorithms used to detect targets embedded in clutter of different statistics. However, the *focus* of this research is actually target detection using fully polarimetric multi-aspect angle images.

#### *1.4 Assumptions*

The target detection algorithms and the conclusions reached from these results are based on the WASAR data provided from the sponsor. The XPATCH-ES WASAR data and their underlying statistics have not been validated by the sponsor. Accordingly, this research assumes that the WASAR generated data from XPATCH-ES is a good model of actual wide angle SAR data.

#### *1.5 Thesis Organization*

Chapter II is a review of relevant literature relating to polarimetric processing, target detection and clutter statistics. The method used to optimally combine the multiple polarimetric WASAR images, into the one intensity image for target detection purposes, is presented. Further, the polarimetric WASAR data (provided by the sponsor) used in this research shall be discussed.

Chapter III presents a statistical analysis of the data used. In addition, clutter models of different statistics are developed and generated. Chapter IV presents the results of applying the algorithms developed in Chapter II to the XPATCH-ES data. Chapter V provides a conclusion and recommendations for further research in this area.

## *II. Theory and Data Generation*

### *2.1 Overview*

In this chapter, the theory of polarimetric and wide angle target detection is briefly reviewed. Then, the method used in this research to optimally combine the polarimetric and wide angle images into the one intensity image for target detection purposes is presented. Two metrics, the standard deviation to mean ratio and the target-to-clutter ratio, that will be used to quantify the performance of the polarimetric and WASAR target detection algorithms, are defined. Two new algorithms developed during this research to combine multi aspect angle images, the WASAR Whitening Filter (WWF) and the Adaptive WASAR Whitening Filter (AWWF), are detailed. A review of the statistics of clutter and targets are presented. The statistical characterization of clutter and targets is used to design detectors in order to determine the Uniformly Most Powerful (UMP) test for the detection of targets. Finally, the polarimetric WASAR data that will be used in this research shall be discussed. The results of using the target detection algorithms developed in this chapter with the polarimetric WASAR data provided by the sponsor are presented in Chapter IV.

### *2.2 Polarimetric Theory*

Polarimetric processing is a means of optimally combining the HH, HV and VV images in order to improve target detection and reduce speckle. Clutter refers to the terrain surrounding a target. It can be man-made such as buildings, factories, houses etc; or natural clutter such as trees, grass, desert etc. Speckle is a coherent scattering phenomenon

that is caused when the scattering volume is deeper than a wavelength. Speckle is the main reason for the lack of optical quality in high resolution SAR imagery.

Targets and clutter have differing geometrical characteristics. With the proper polarimetric processing, the radar return from clutter and target might be distinguished from each other [9]. Further, a complex target can be considered as comprising a multitude of independent objects that scatter energy in all directions [23]. Accordingly, it should be considered whether the target will provide a stronger radar return or ‘*glint*’ at a different polarization, aspect angle or frequency.

Gaussian clutter models, which characterize homogeneous clutter regions have been developed by Novak [15]. These algorithms use fully polarimetric data and optimally combine the HH, HV and VV images to reduce image speckle. In particular, the polarimetric algorithms presented by Novak include: the span of the three complex elements (HH, HV and VV); the Polarimetric Optimal Weighted (POW) sum of intensities; the Polarimetric Matched Filter (PMF); and the Polarimetric Whitening Filter (PWF). These algorithms were developed by analyzing the covariance matrix of the polarimetric data, which characterizes the relationship between the radar returns at different polarizations. The covariance matrix is defined as  $\Sigma_X = E\{XX^\dagger\}$ , where  $\dagger$  is the complex conjugate transpose and  $X$  is the radar return vector consisting of the three complex elements HH, HV and VV, defined as

$$X = \begin{bmatrix} HH_i + jHH_q \\ HV_i + jHV_q \\ VV_i + jVV_q \end{bmatrix}. \quad (1)$$



The covariance matrix has the following form

$$\sum_x = \begin{bmatrix} E\{|HH|^2\} & E\{(HH)(HV)^*\} & E\{(HH)(VV)^*\} \\ E\{(HV)(HH)^*\} & E\{|HV|^2\} & E\{(HV)(VV)^*\} \\ E\{(VV)(HH)^*\} & E\{(VV)(HV)^*\} & E\{|VV|^2\} \end{bmatrix} \quad (2)$$

where  $E$  stands for the statistical expected value and ‘\*’ is the complex conjugate. For a Gaussian polarimetric clutter model, Novak [15] has shown that the covariance matrix simplifies to the following form

$$\sum_x = \begin{bmatrix} \sigma & 0 & \rho\sqrt{\gamma} \\ 0 & \epsilon & 0 \\ \rho^*\sqrt{\gamma} & 0 & \gamma \end{bmatrix} \quad (3)$$

where  $\sigma$ ,  $\rho$ ,  $\gamma$  and  $\epsilon$  are defined as

$$\sigma = E\{|HH|^2\} \quad (4)$$

$$\rho = \frac{E\{HH \cdot VV^*\}}{\sqrt{E\{|HH|^2\}E\{|VV|^2\}}} \quad (5)$$

$$\gamma = \frac{E\{|VV|^2\}}{E\{|VV|^2\}} \quad (6)$$

$$\epsilon = \frac{E\{|HV|^2\}}{E\{|HH|^2\}}. \quad (7)$$

Non-Gaussian clutter models have been developed in a similar manner by Lee [12], Oliver [18] and Jakeman [10].

### 2.3 Polarimetric Algorithms

This section derives and details the polarimetric algorithms used in this research. These algorithms combine the polarimetric measurements (HH,HV,VV) to produce an intensity image that will minimize speckle and maximize target detection. But initially, two metrics used to quantify the performance of each algorithm (with regard to reducing speckle and improving target detection capabilities) shall be defined.

*2.3.1 Metrics.* Two metrics commonly used to measure and quantify the improvement of the polarimetric processing techniques are the standard deviation to mean ratio and the target to clutter ratio.

*2.3.1.1 Standard Deviation to Mean Ratio (S/M).* The standard deviation to mean ratio is calculated by computing an estimate of the standard deviation of the pixel intensities of the image and dividing by an estimate of the mean value of the pixel intensities of an image. Mathematically, this ratio is defined as

$$\frac{S}{M} = \frac{st.dev\{y\}}{E\{y\}} \quad (8)$$

where  $y$  is a random variable that denotes pixel intensity. The mean pixel intensity is estimated by

$$\mu_y = \frac{1}{n} \sum_{i=0}^{n-1} y_i \quad (9)$$

where  $n$  is the number of pixels in an image. The standard deviation is calculated by taking the square root of an estimate of the variance of the pixel intensities. The variance

is estimated by

$$var\{y\} = \frac{1}{n} \sum_{i=0}^{n-1} |y_i|^2 - \mu_y^2. \quad (10)$$

A low S/M ratio indicates a minimum speckle image.

*2.3.1.2 Target to Clutter Ratio (T/C).* The target to clutter ratio is defined

as

$$\frac{\sigma_T}{\sigma_C} = \frac{E\{|t^2|\}}{E\{|c^2|\}}. \quad (11)$$

This metric quantifies any improvement gained from the polarimetric processing, it is a measure of the average output power in the target region relative to the average output power in the clutter region. The T/C metric is computed by extracting the pixels in an area around the known location of the targets (i.e. 16 x 10 pixels - refer below for target window size), computing the average power of these pixels and dividing this value by the average power of the pixels remaining after the targets have been extracted. All the targets used in this research are M-35 trucks. By analyzing the images it was determined that the typical target size of the M-35 trucks is 16 pixels long and 10 pixels wide. The target pixel window can be easily adjusted to search for any size target. For example, if the objective of a search is to detect scud missile launchers then a longer narrower pixel window might be more appropriate.

*2.3.2 Polarimetric Average.* The polarimetric average of the three complex images is defined as

$$Average = \frac{1}{3}(|HH|^2 + |HV|^2 + |VV|^2). \quad (12)$$

The polarimetric average is a simple and suboptimal way of combining the three images to produce a combined intensity image.

*2.3.3 Polarimetric Span.* The polarimetric span of the three complex images is defined as

$$SPAN = |HH|^2 + 2|HV|^2 + |VV|^2. \quad (13)$$

The span is simply the addition of the intensities of the polarimetric information. The squaring operation enhances high intensity values and lower intensity values are de-emphasized. Further, phase information is not used in the span calculation and the weighting coefficients of each polarimetric image are not optimally derived. Accordingly, the span is also a suboptimal algorithm.

*2.3.4 Polarimetric Whitening Filter (PWF).* The PWF, developed by Novak, was derived to optimally combine the HH, HV, VV measurements to produce an intensity image having a minimum amount of speckle. The optimization problem involves processing the polarimetric measurement vector  $X$  ( $X = [HH, HV, VV]^T$ ) with a quadratic weighting matrix  $A$  such that the output image pixel intensity is

$$y = X^\dagger AX$$

where  $X^\dagger$  is the complex conjugate transpose of the radar measurement vector  $X$ . The objective of the optimization is to find a weighting matrix  $A$  that yields an output image having minimum speckle. The S/M ratio (given by equation 8) is the metric used to measure the speckle. Thus,

$$\frac{S}{M} = \frac{st.dev\{y\}}{E\{y\}} = \left( \frac{var(X^\dagger AX)}{E^2(X^\dagger AX)} \right)^{\frac{1}{2}}.$$

This expression is simplified by using the following two identities

$$E(X^\dagger AX) = \sum_{i=1}^3 \lambda_i$$

$$var(X^\dagger AX) = \sum_{i=1}^3 \lambda_i^2$$

where  $\lambda_i$  are the eigenvalues of the matrix  $\Sigma_X A$ . Using a Lagrange multiplier the S/M ratio is minimized so that all the eigenvalues of  $\Sigma_X A$  are equal to one [15]. Thus, the optimal weighting matrix is  $\Sigma_X A = 1$  or  $A = \Sigma_X^{-1}$ . Accordingly, the minimum speckle image is constructed as

$$y = X^\dagger \Sigma_X^{-1} X \quad (14)$$

where  $\Sigma_X^{-1}$  is the inverse covariance matrix of the polarimetric radar measurement vector  $X$ . Using a Gaussian clutter model, Novak determined that the covariance matrix simplifies to the form shown in Equation 3 and thus the PWF is defined as

$$PWF = \frac{|HH|^2 + |VV|^2}{\sigma_{HH}(1 - |\rho^2|)} + \frac{|HV|^2}{\sigma_{HH}\epsilon} - \frac{2|\rho||HH||VV|\cos(\phi_{HH} - \phi_{VV} - \phi_\rho)}{\sigma_{HH}(1 - |\rho^2|)\sqrt{\gamma}} \quad (15)$$

where  $\rho$ ,  $\gamma$  and  $\epsilon$  are defined in Equations 5, 6 and 7, and  $\phi_{HH}$ ,  $\phi_{VV}$  and  $\phi_\rho$  are the phases of the complex quantities HH, VV and  $\rho$ . As this equation was derived through a Lagrange minimization of the S/M ratio, the PWF is the optimum combination of the polarimetric measurements. The resulting intensity image has minimum speckle as will be shown in Chapter IV. The PWF combined image can be formed by either directly using Equation 15 or by estimating the polarimetric covariance matrix and using Equation 14. All PWF images in this research are formed by estimating the polarimetric covariance matrix and using Equation 14.

*2.3.5 Polarimetric Optimal Weighting (POW).* The optimal (minimum speckle) weighting algorithm, developed by Novak [15], is a simplified version of the PWF and is defined as

$$POW = |HH|^2 + \frac{1 + |\rho|^2}{\epsilon} |HV|^2 + \frac{1}{\gamma} |VV|^2 \quad (16)$$

where  $\rho$ ,  $\gamma$  and  $\epsilon$  are defined in Equations 5, 6 and 7.

*2.3.6 The Polarimetric Matched Filter (PMF).* The PMF was developed by Novak in a similar way as the PWF. However, the aim of this algorithm is to combine the HH, HV, and VV SAR returns into an intensity image that maximizes target detection. Accordingly, the PMF is derived by performing a Lagrange maximization of the T/C metric. The resulting PMF image is formed from the linear combination  $y = h^\dagger X$ . Thus, the object of the optimization is to find the complex vector  $h$  that maximizes the T/C

metric. Thus,

$$\frac{T}{C} = \frac{h^\dagger \Sigma_t h}{h^\dagger \Sigma_c h}.$$

Novak [17] shows that the optimal processor  $h$ , is the eigenvector corresponding to the maximum eigenvalue of the matrix  $\Sigma_c^{-1} \Sigma_t$ . A major disadvantage of the PMF is that both the target and clutter covariance  $\Sigma_t$  and  $\Sigma_c$  are required *a priori*. Typically, in most target detection scenarios, this information is unknown.

#### 2.4 Multiple Aspect Angle Algorithms

Fully polarimetric WASAR offers multiple images of a target scene at different aspect angles and polarizations. The objective of the multiple aspect angle algorithms is to exploit a characteristic or feature of the WASAR data that will discriminate between targets and clutter false alarms. The fully polarimetric SAR target detection algorithms (such as the PWF, SPAN, POW - discussed in Section 2.3) exploit the polarimetric properties of the data to discriminate between targets and clutter. Previous AFIT research [11, 25] into target detection using WASAR data investigated various techniques such as subtraction and exploiting the standard deviation feature. The results indicated that even the most simple WASAR methods showed an improvement over common SAR methods. This research shall derive algorithms that will optimally combine the WASAR polarimetric measurement vector  $X$  such that the combined image is of the form  $y = X^\dagger A X$ . This is the same form as the PWF. To this end, two new multi aspect angle algorithms, the WWF and the AWWF are developed. The primary objective of the optimization problem is to

find a weighting matrix  $A$  that will minimize the S/M metric or maximize the T/C metric.

The fully polarimetric WASAR measurement vector  $X$  shall have the following form

$$X = \begin{bmatrix} HH_{-45^\circ} \\ HV_{-45^\circ} \\ VV_{-45^\circ} \\ \hline HH_{-30^\circ} \\ HV_{-30^\circ} \\ VV_{-30^\circ} \\ \hline \vdots \\ \hline HH_{+30^\circ} \\ HV_{+30^\circ} \\ VV_{+30^\circ} \\ \hline HH_{+45^\circ} \\ HV_{+45^\circ} \\ VV_{+45^\circ} \end{bmatrix} \quad (17)$$

and the single polarity WASAR radar measurement vector shall have the following form

$$X = \begin{bmatrix} HH_{-45^\circ} \\ HH_{-30^\circ} \\ HH_{-15^\circ} \\ HH_{0^\circ} \\ HH_{+15^\circ} \\ HH_{+30^\circ} \\ HH_{+45^\circ} \end{bmatrix}. \quad (18)$$

The radar measurement vector  $X$  can also be modified to include frequency, polarization and multiple aspect angle by expressing  $X$  as



$$X = \begin{bmatrix} HH_{-45^\circ(8Mhz)} \\ HV_{-45^\circ(8Mhz)} \\ VV_{-45^\circ(8Mhz)} \\ \cdot \\ \cdot \\ \cdot \\ HH_{+45^\circ(8Mhz)} \\ HV_{+45^\circ(8Mhz)} \\ VV_{+45^\circ(8Mhz)} \\ \text{---} \\ \cdot \\ \cdot \\ \cdot \\ \text{---} \\ HH_{-45^\circ(10Mhz)} \\ HV_{-45^\circ(10Mhz)} \\ VV_{-45^\circ(10Mhz)} \\ \cdot \\ \cdot \\ \cdot \\ HH_{+45^\circ(10Mhz)} \\ HV_{+45^\circ(10Mhz)} \\ VV_{+45^\circ(10Mhz)} \end{bmatrix}. \quad (19)$$

For example, if data were recorded at 8, 9 and 10MHz at aspect angles of  $-45^\circ$  to  $+45^\circ$  at  $15^\circ$  increments and fully polarimetric, 63 images would be generated. Therefore,  $X$  would be a 63 x 1 measurement vector, and the resulting covariance matrix would be 63 x 63. Alternatively,  $X$  could be adjusted to include any combination of the parameters of frequency, polarization and multiple aspect angle that would maximize target detection.

*2.4.1 WASAR Average.* The WASAR average image (formed from  $y = X^\dagger AX$ ) is defined, for the single polarity (HH) case, as

$$WASAR_{AVE} = X^\dagger \begin{bmatrix} 1/7 & 0 & . & . & . & . & 0 \\ 0 & 1/7 & 0 & . & . & . & . \\ . & . & . & . & . & . & . \\ . & . & . & . & . & . & . \\ . & . & . & . & . & . & . \\ 0 & . & . & . & . & 1/7 & 0 \\ 0 & . & . & . & . & 0 & 1/7 \end{bmatrix} \begin{bmatrix} HH_{-45^\circ} \\ HH_{-30^\circ} \\ HH_{-15^\circ} \\ HH_{0^\circ} \\ HH_{+15^\circ} \\ HH_{+30^\circ} \\ HH_{+45^\circ} \end{bmatrix}. \quad (20)$$

The WASAR average algorithm is a suboptimal method of combining the WASAR images. Knurr [11] and Sumner [25] used a direct average of pixel amplitudes to form an average image (i.e.  $y = \frac{1}{N} \sum_{i=1}^N x_i$ ). An average pixel intensity algorithm is used rather than an average of pixel amplitudes because all the WASAR algorithms form intensity images. Thus, when comparing WASAR algorithms intensity images can be compared to intensity images. The WASAR average intensity algorithm is used as a benchmark for comparing the other WASAR algorithms.

*2.4.2 WASAR Whitening Filter (WWF).* Following the same derivation detailed in Section 2.3.4 for the PWF the WWF developed during the course of this research is defined as

$$WWF = X^\dagger \Sigma_X^{-1} X \quad (21)$$

where  $\Sigma_X$  is the covariance matrix of the multiple aspect measurement vector  $X$ , defined in Equation 18. Although the primary objective of the PWF is to reduce image speckle it has been shown that the PWF also improves target detection performance [16, 3]. Hence, the WWF image promises to provide better target detection performance than the WASAR average image.

*2.4.3 Adaptive WASAR Whitening Filter (AWWF).* The AWWF, also developed during the course of this research has the same form as the WWF defined at Equation 21. However, the wide angle covariance matrix is adaptively formed from local pixels.

The AWWF image is formed by segmenting the larger image of the target scene into smaller non-overlapping windows. The optimum size of the window depends on the target size, and for the XPATCH-ES data used in this research a 10 x 10 pixel sized window was determined to be the optimum window size. The method used to calculate the optimum window size for the AWWF algorithm is discussed at Section 4.2.3. For each window the wide angle covariance matrix is computed. Through an analysis of the wide angle covariance matrix (presented at Section 3.2.5.2) it was shown that the wide angle covariance matrix for clutter is a diagonal matrix with approximately uniform diagonal elements. For a target, the wide angle covariance matrix is also a diagonal matrix, however, the values of the diagonal elements vary. This analysis, as will be seen, proved the assumption that natural clutter ‘looks’ the same at different aspect angles whereas targets ‘look’ considerably different at even small changes in aspect angle. Accordingly, if the pixel window contains just clutter then the normalized (to the maximum return) wide angle covariance matrix for this image segment is simply the identity matrix. Thus, each newly formed pixel in this segment of the target scene is simply the sum of the pixel intensities from each of the individual image segments. However, if the pixel window contains a target, then the inverse normalized wide angle covariance matrix enhances the weaker aspect angle returns. Figure 3 is a schematic illustrating the formation of the AWWF image. The following mathematical example, for a three aspect angle case, demonstrates the formation of the AWWF image. Pixel windows are extracted from each of the three aspect angle images.

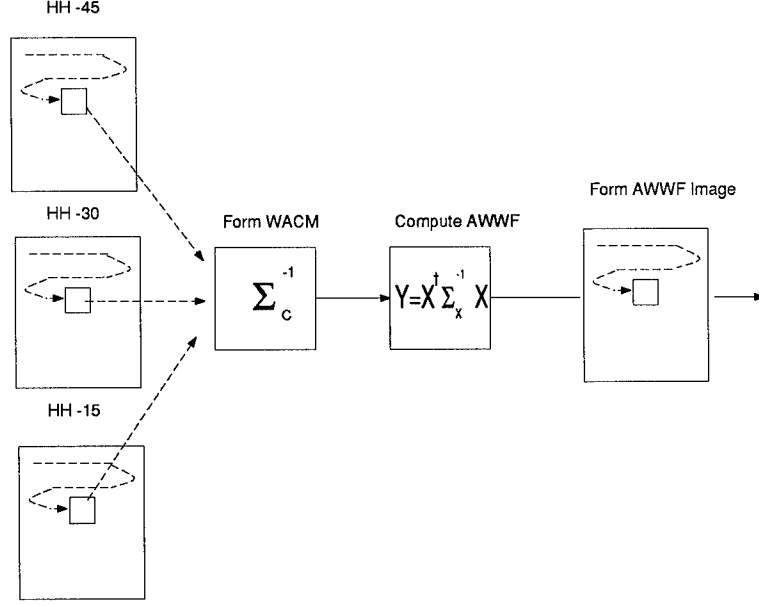


Figure 3. Generation of AWWF Image

If the pixel window contains just clutter the inverse normalized WACM for this window is approximately the identity matrix, and all the pixels within the window will be formed in the following way

$$\begin{aligned}
 Y &= \begin{bmatrix} HH_{-45^\circ} & HH_{0^\circ} & HH_{+45^\circ} \end{bmatrix}^* \begin{bmatrix} 1 & 0 & 0 \\ 0 & 1 & 0 \\ 0 & 0 & 1 \end{bmatrix} \begin{bmatrix} HH_{-45^\circ} \\ HH_{0^\circ} \\ HH_{+45^\circ} \end{bmatrix} \\
 &= |HH_{-45^\circ}|^2 + |HH_{0^\circ}|^2 + |HH_{+45^\circ}|^2
 \end{aligned}$$

where “\*” is the complex conjugate of the measurement vector. Thus, each pixel in the window is simply the sum of the pixel intensities. However, for a target, the diagonal elements of the adaptive wide angle covariance matrix vary. A typical target WACM (refer Section 3.2.5.2 for actual results) is

$$\Sigma_C = \begin{bmatrix} 0.2 & 0 & 0 \\ 0 & 1 & 0 \\ 0 & 0 & .5 \end{bmatrix}$$

the inverse wide angle covariance matrix for this example is

$$\Sigma_C^{-1} = \begin{bmatrix} 5 & 0 & 0 \\ 0 & 1 & 0 \\ 0 & 0 & 2 \end{bmatrix}$$

and the pixels within the window will be formed as

$$\begin{aligned} Y &= \begin{bmatrix} HH_{-45^\circ}^* & HH_{0^\circ}^* & HH_{+45^\circ} \end{bmatrix}^* \begin{bmatrix} 5 & 0 & 0 \\ 0 & 1 & 0 \\ 0 & 0 & 2 \end{bmatrix} \begin{bmatrix} HH_{-45^\circ} \\ HH_{0^\circ} \\ HH_{+45^\circ} \end{bmatrix} \\ &= 5|HH_{-45^\circ}|^2 + |HH_{0^\circ}|^2 + 2|HH_{+45^\circ}|^2. \end{aligned}$$

Thus, all the pixels within the target window are enhanced. This result promises to significantly enhance target detection capabilities.

**2.4.4 WASAR Matched Filter (WMF).** Following the same derivation detailed in Section 2.3.6, the WMF is defined as  $y = h^\dagger X$ , where  $h$  is the eigenvector corresponding to the maximum eigenvalue of the matrix  $\Sigma_c^{-1} \Sigma_t$ . The WMF is not implemented as this algorithm relies on *a priori* information of the targets to form the target covariance matrix.

**2.4.5 Combinations of Polarimetric and Wide Angle Algorithms.** The polarimetric WASAR images can be combined into the one image to be used for target detection in a number of ways. First, if the target scene is imaged from seven different aspect angles at three different polarizations, the 21 images can be directly combined using either the

WWF (21 x 21 covariance matrix) or the AWWF to form a single image for target detection purposes. Alternatively, the polarimetric images could first be combined using the polarimetric algorithms (i.e. Average, PWF, Span etc.) and then these seven aspect angle polarimetric images could be combined using wide angle algorithms (such as the WWF or AWWF). Figure 4 is a simple schematic showing both methods of combining the 21 polarimetric WASAR images.

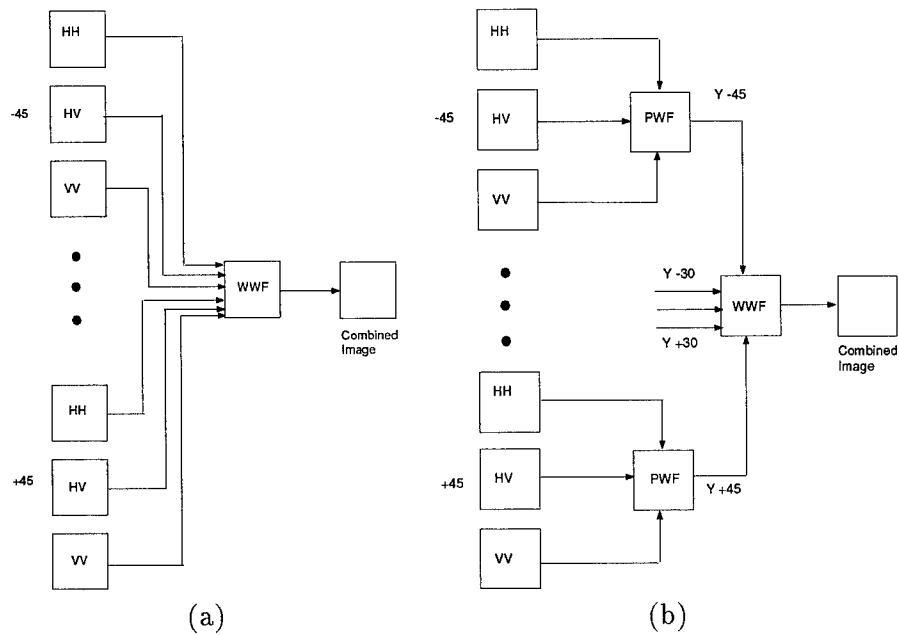


Figure 4. Two methods of combining WASAR Polarimetric images (a) Combining all aspect angles and polarizations, (b) Combining Polarizations and then combining these images at the different aspect angles using either WWF or AWWF algorithms.

## 2.5 Target Detection Theory

Target detection is the process of distinguishing targets from background clutter and noise. The detection process of a SAR is automatically performed within the SAR receiver. Accordingly, the detection criteria must be carefully specified. Target detection is specified

in terms of a threshold, and decisions are based upon the outcome of a comparison between a Pixel-Under-Test (PUT) and a threshold level. If the PUT exceeds the threshold level the pixel is said to be a target pixel. Accordingly, the detector classifies the pixels within a target scene as one of two hypothesis,  $H_0$ : no target present and  $H_1$ : target present, where

$$H_0 : \theta \in \theta_0 \text{ (No target)}$$

$$H_1 : \theta \in \theta_1 \text{ (Target)}.$$

This is a binary test of  $H_0 : \theta \in \theta_0$  versus  $H_1 : \theta \in \theta_1$  and takes the form

$$\phi(x) = \begin{cases} 1 \sim H_1, & x \in A \\ 0 \sim H_0, & x \in R \end{cases}.$$

This equation is interpreted as: the test function  $\phi(x)$  equals 1 and hypothesis  $H_1$  is accepted if the measurement  $x$  lies in the acceptance region (i.e. a target has been detected). If the measurement  $x$  lies in the rejection region the test function is assigned 0 and hypothesis  $H_0$  is accepted.

The threshold level is determined by the probability of false alarm. Incorrectly setting the threshold level can cause an error in the decision process. There are two types of errors that can be made. A type I error occurs when clutter is mistaken for a target. This type of error is referred to as a *false alarm* and occurs whenever the clutter exceeds the threshold level. A type II error is when a target is erroneously considered to be clutter. This type of error is known as a *missed detection*. A large threshold reduces the probability of a false alarm, however, the probability of missed detections increases. Accordingly, there is

a tradeoff between the two types of errors. System operational requirements determine the threshold level setting and hence the importance of the two types of errors.

If the clutter and the target plus clutter distributions are exactly known, then the Neyman-Pearson detector provides the most powerful test (as it optimizes the probability of detection for a given probability of false alarm) of size ( $\alpha$ ) for testing the simple hypothesis versus the simple alternative. Mathematically, the Neyman-Pearson detector is a likelihood ratio test of the form

$$\phi(x) = \begin{cases} 1 & l(x) > t \\ 0 & l(x) \leq t \end{cases}$$

where  $l(x)$  is the likelihood ratio defined as

$$l(x) = \frac{f_{(x|s_1)}}{f_{(x|s_0)}}.$$

and  $t$  is the threshold level.

Therefore, the probability of false alarm ( $P_{fa}$ ) also known as the size ( $\alpha$ ) is defined as

$$\begin{aligned} \alpha = P_{fa} &= P_{(x|s_0)}[l(x) > t] \\ &= \int_T^\infty f_{(x|s_0)}(l)dl. \end{aligned} \tag{22}$$

For a given  $P_{fa}$  the threshold can be calculated from Equation 22. The probability of detection ( $P_D$ ) also known as the power ( $\beta$ ) is defined as

$$\begin{aligned} \beta = P_D &= P_{(x|s_1)}[l(x) > t] \\ &= \int_T^\infty f_{(x|s_1)}(l)dl \end{aligned} \tag{23}$$



and the probability of a missed detection  $P_M$  is defined as

$$P_M = 1 - P_D.$$

Figure 5 is a plot showing the probability distributions of the two classes in the detection problem. For the detection of targets embedded in clutter,  $S_1$  could be the probability distribution of the clutter and  $S_2$  the probability distribution of the targets. Figure 5 also shows the probability of false alarm ( $P_{fa}$ ) and the probability of detection ( $P_D$ ). The probability of false alarm (as shown in Figure 5) is the area of  $S_1$  (clutter pdf) from the threshold ( $t$ ) to  $+\infty$ , and the probability of detection is the area of  $S_2$  (target pdf) from the threshold to  $+\infty$ . Plots of  $P_D$  versus  $P_{fa}$  are known as Receiver Operating Characteristics

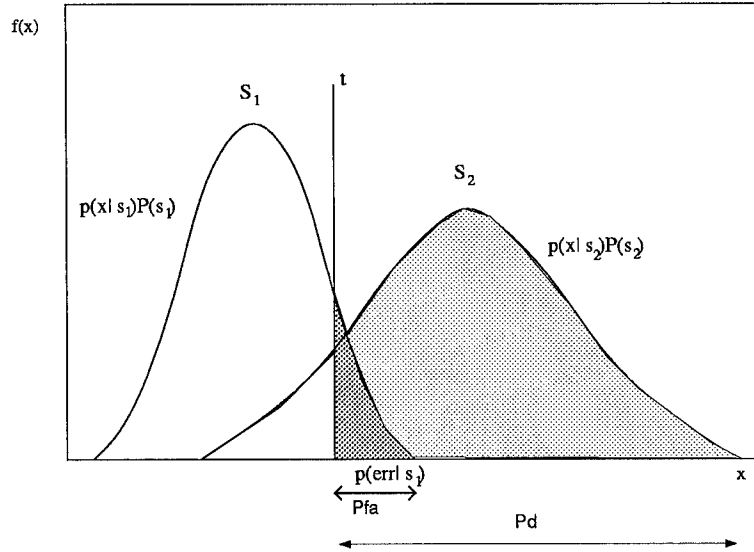


Figure 5. Probability of Detection and False Alarm

(ROC) curves and these are used to quantify the performance of a detector. Figure 6 is a typical plot of ROC curves. If the test is a good one then the curves should be above the *chance line* (which characterizes the performance of a pure guess) shown in Figure 6.

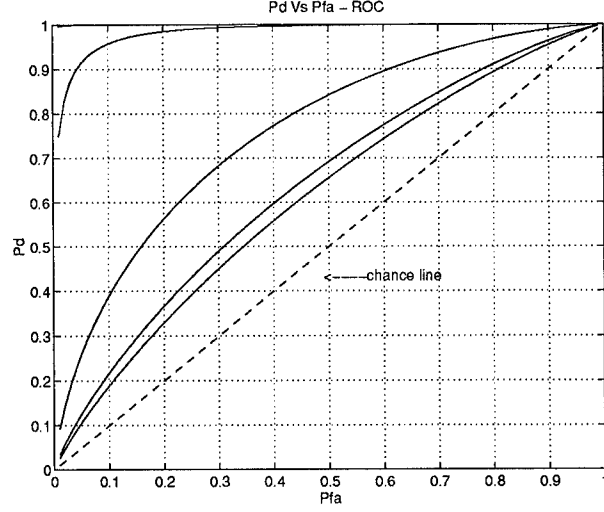


Figure 6. Receiver Operating Characteristics (ROC curves)

In a target scene the clutter: mean, variance, and type of distribution vary within the scene. For example a group of trees within a grassy field will have a different distribution, mean and variance than the grass surrounding it. Further, the distributions of the clutter and the target are not known *a priori*. In this situation the Neyman-Pearson detector, which has a constant threshold, does not produce a constant false alarm rate. Accordingly, a target detection system's performance is often degraded by a varying number of false alarms. To improve performance, a Constant False Alarm Rate (CFAR) algorithm is used. CFAR algorithms provide detection thresholds in automatic detection radar systems. These detection thresholds are relatively immune to clutter and allow target detection with a constant false alarm rate. A two parameter CFAR detector is defined by

$$\frac{x - \mu_c}{\sigma_c} > t_D \quad (24)$$

where  $x$  represents the test pixel,  $\mu_c$  and  $\sigma_c$  are estimates of the mean and standard deviation of the local clutter, and  $t_D$  is the detection threshold. A target is declared if the ratio defined in equation 24 exceeds the detection threshold.

A CFAR detector is implemented as follows. For this work a rectangular window, called a reference window, is centered around the PUT. A typically sized window is 60 pixels x 60 pixels. The statistics within this reference window are estimated and the detector is defined by the following rule

$$\frac{x_i - \mu_c}{\sigma_c} \cdot \begin{cases} > T_{CFAR} (Target) \\ \leq T_{CFAR} (No Target) \end{cases}$$

where  $x_i$  is the amplitude of the test pixel,  $\mu_c$  is an estimate of the mean of the local pixel amplitudes,  $\sigma_c$  is an estimate of the standard deviation of the local clutter and  $T_{CFAR}$  is a threshold level that defines the false alarm rate. Figure 7 is a sketch of the reference window used in the two parameter CFAR detector.

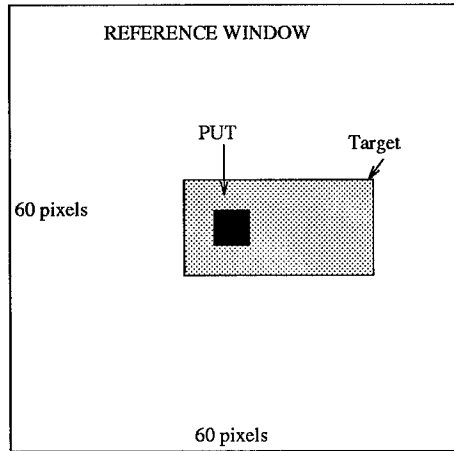


Figure 7. Reference Window of two parameter CFAR detector

As shown in Figure 7 the test pixel is in center of the defined local region and the 60 x 60 pixels surrounding the PUT are used to estimate  $\mu_c$  and  $\sigma_c$  of the local clutter. If the detection statistic exceeds  $T_{CFAR}$  the test pixel is declared a target pixel, if it is not it is declared a clutter pixel.

For a Gaussian amplitude distribution of the clutter, the CFAR detector provides a constant false alarm rate. However, clutter distributions are typically not Gaussian. In spite of this fact, the two parameter CFAR detector defined above proves to be an efficient algorithm for detecting targets in clutter and is used extensively.

## 2.6 Statistical Analysis of Clutter and Targets

The statistical characterizations of clutter and targets are used to design detectors that will differentiate between the two hypotheses ( $H_0$ :No Target and  $H_1$ :Target) in the target detection decision problem. The objective is to design an invariant detector that is Uniformly Most Powerful (UMP) of size  $\alpha$  for testing  $H_0$  versus  $H_1$ . Accordingly, the first step in solving the target detection problem is to determine the distribution of the two classes ( $H_0$  and  $H_1$ ). Clutter from different terrain and grazing angles has different statistics. For example, the log-normal distribution has been found to be a good fit for sea clutter and land clutter at low grazing angles  $\leq 5^\circ$ , whereas the Weibull clutter model is used for grazing angles between 1 and 30 degrees [20] and sparse forests observed by a high resolution radar [27]. The Rayleigh model is used for clutter whose amplitude probability distribution encompasses a limited dynamic range (i.e. bare ground surfaces, agricultural fields and dense forest canopies). In the following sections clutter of different distributions will be presented and the techniques that will be used to determine the best distribution fit

for the XPATCH-ES clutter and target data (provided by the sponsor) shall be developed. A complete statistical analysis of the XPATCH-ES data is presented in Chapter III.

*2.6.1 Gaussian Distribution.* Gaussian statistics have been assumed in many cases to model clutter [15, 17]. Typical terrain clutter distributions have a shape that is heavy tailed when compared to the Gaussian distribution. The Gamma, Weibull, K-distributed and log-normal distributions have been found to more accurately model terrain clutter [6, 22, 27]. However, a statistical analysis assuming Gaussian clutter statistics provides a way of theoretically modelling clutter. The Gaussian probability density function (pdf) is defined as

$$f(x) = \frac{1}{\sqrt{2\pi}\sigma} \exp\left\{-\frac{(x-\mu)^2}{2\sigma^2}\right\} \quad -\infty \leq x < \infty \quad (25)$$

where,  $\mu$  is the mean,  $\sigma$  is the standard deviation and  $\sigma^2$  is the variance.

*2.6.2 Gamma Distribution.* The gamma distribution provides a good fit for many types of terrain and is used in many non-Gaussian clutter models [15]. Further, the two-parameter gamma pdf provides a large number of functions from which to choose. The gamma pdf is defined as

$$f(x) = \frac{1}{x} \left(\frac{x}{\bar{x}}\right)^{\nu-1} \frac{1}{\Gamma(\nu)} \exp\left\{-\frac{x}{\bar{x}}\right\} \quad 0 \leq x < \infty \quad (26)$$

where  $\bar{x}$  and  $\nu$  are the mean and the variance of the distribution.

*2.6.3 Weibull Distribution.* The Weibull distribution has been found to be a good fit of the radar clutter returns, if the measured data is from complex terrains such as:

sea clutter [22]; land clutter at low grazing angles [2]; and sparse forests observed by a high resolution radar [27]. Other papers that have cited the Weibull distribution as a good fit for radar clutter include Novak [15, 14]; Greenstein *et al* [6]; and Trunk and George [26]. The pdf of the Weibull distribution is

$$f(x) = \frac{\eta}{\nu} \left(\frac{x}{\nu}\right)^{\nu-1} \exp\left\{-\left(\frac{x}{\nu}\right)^\eta\right\} \quad 0 \leq x < \infty \quad (27)$$

where  $\eta$  is the scale parameter and  $\nu$  is the shape parameter. The shape parameters are a function of surface condition, grazing angle, wavelength and polarization.

**2.6.4 Rayleigh Distribution.** The Rayleigh distribution is a special case of the Weibull distribution, i.e. when the Weibull scale parameter ( $\eta$ ) equals one, Equation 27 becomes the Rayleigh density function,

$$f(x) = \frac{2x}{< x^2 >_{av}} \exp\left\{-\frac{x^2}{< x^2 >_{av}}\right\} \quad 0 \leq x < \infty \quad (28)$$

where  $< x^2 >_{av}$  is the average value of  $x^2$ .

**2.6.5 Log-Normal Distribution.** The log-normal model has been found to be a good fit of the radar clutter returns, particularly if the measured data is from complex terrain categories. The pdf of the log-normal distribution is

$$f(x) = \begin{cases} \frac{1}{\sqrt{2\pi}\sigma x} \exp\left\{-\frac{(\ln(x)-\mu)^2}{2\sigma^2}\right\} & x \geq 0 \\ 0 & x < 0 \end{cases}$$

where,  $\mu = E(\ln x)$ ,  $\sigma^2 = \text{Var}(\ln x)$ .

## *2.7 Method of Determining the Distribution of Target and Clutter Pixel Intensities*

The following procedure details how the distribution of the targets and clutter shall be determined. First, for the distribution of the targets, the center co-ordinates of all the targets within a target scene shall be obtained from the XPATCH- ES program. Then, an area of 16 x 10 pixels surrounding these known locations of the targets shall be extracted from the image. These target pixels will be reshaped and formed into a vector. If there were six targets in a target scene the target vector for this image would be a 1 x 960 vector of target pixel intensities. Using Matlab, the target vector will be histogrammed. Finally, curves of pdfs such as the Weibull, gamma, log-normal etc... distributions shall be plotted over the target histogram. The distribution of the targets shall be determined according to the best fit of these curves. A clutter pixel vector will be obtained by forming a vector of all the pixels remaining in the image after the targets have been extracted. The distribution of the clutter shall be determined using the same procedure detailed for the target distribution. Figure 8 shows the curve fitting procedure of a Gaussian and Rayleigh distributed random variable. Actual target and clutter distributions from target scenes supplied from the XPATCH-ES program can be seen in Chapter III. The Matlab code used to form the clutter and target pdfs is at Appendix A.

## *2.8 Data Generation and Rotation*

The data used in this research were generated using a pre-release version of software being developed by Loral for the Wright-Labs Target Recognition Branch (XPATCH-ES). One complete WASAR data set, and three other polarimetric data sets were generated and provided by the sponsor using this software. Images of a single target scene (for

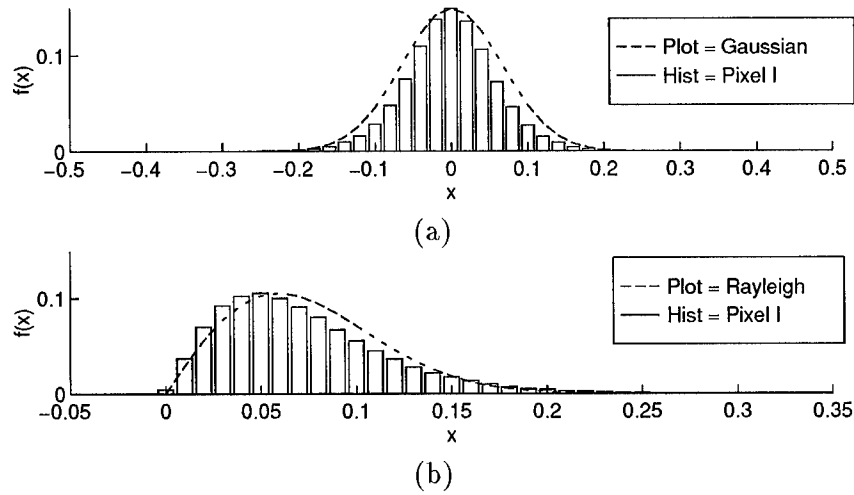


Figure 8. Example of pdf curve fitting to determine the distribution of targets and clutter (a) Gaussian distributed random variable (b) Rayleigh distributed random variable.

the complete WASAR data set) were produced for seven different view angles at three polarizations, resulting in a total of 21 images in the WASAR data set. The seven aspect angles ranged from  $-45^\circ$  to  $45^\circ$  in  $15^\circ$  degree increments. A SAR image at an aspect angle of  $45^\circ$  refers to an image generated from a swath of data whose center angle corresponds to a radar target orientation of  $45^\circ$ . The frequency, tilt angle and resolution of the WASAR data were the same for all data sets. The frequency of the WASAR data is 1000MHz, the tilt angle is  $45^\circ$ , and the resolution is 1.5ft x 1.5ft. For this research, two data sets were mainly used and these will be referred to as DATA Set 1, which is the complete fully polarimetric WASAR data set consisting of 21 images, and Data Set 2, which is a polarimetric SAR data set consisting of 3 images (HH, HV and VV) at the one aspect angle. Figure 9 shows the 21 un-processed images of the target scene of the complete WASAR data set, Data Set 1. Figure 38 in Chapter III shows the 3 (HH, HV and VV) unprocessed images and ground truth map of the target scene for Data Set 2.



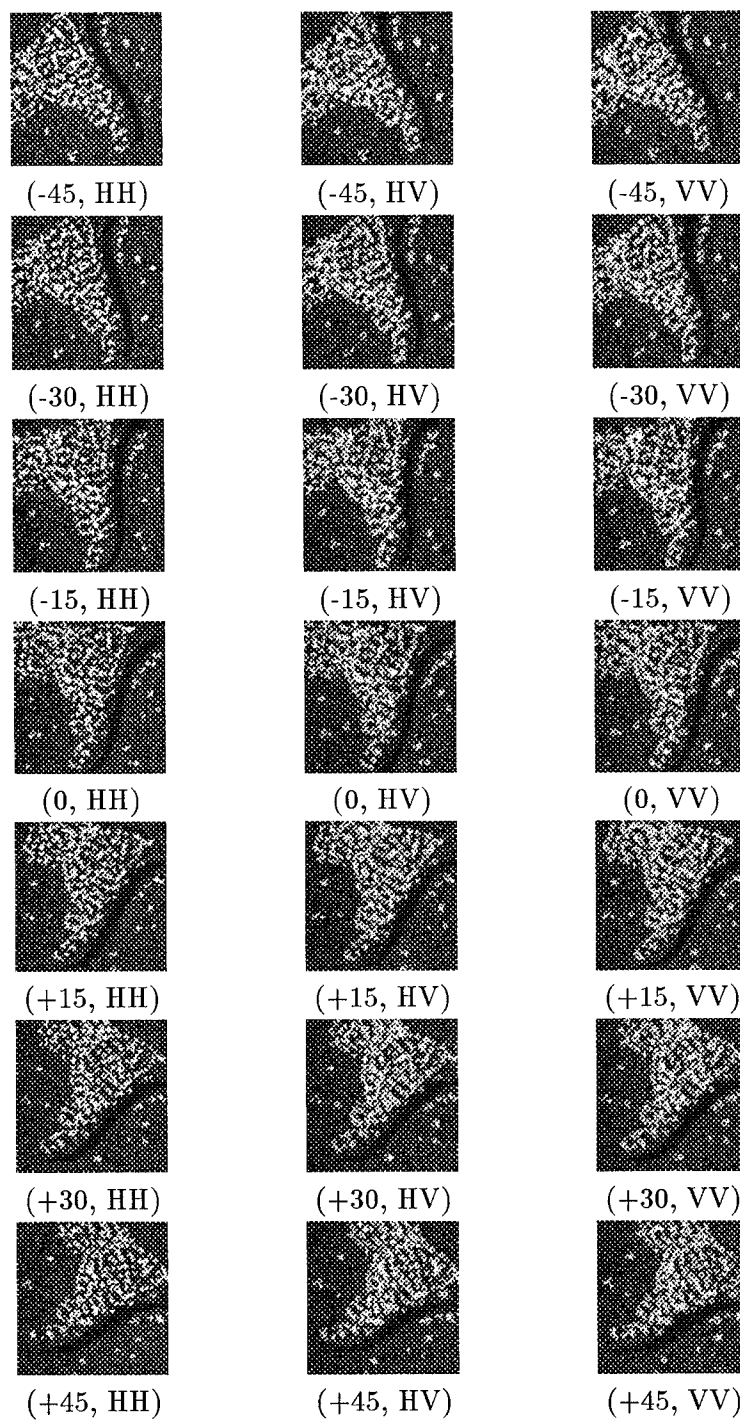


Figure 9. Data Set 1 Before Rotation

Prior to any processing and detecting, all of the images must be transformed into the same coordinate system to ensure pixel to pixel correlation between the different aspect angle images. This process is known as registration. The registration of the images into the same coordinate system was done using a nearest neighbor rotation algorithm developed by Knurr [11]. One of the unavoidable disadvantages of the rotation process is the loss of information. This occurs because the image after rotation is smaller than the original image. Unfortunately, the rotated image can only be as large as the pixels overlapping the unrotated image. For example, an unrotated image at an aspect angle of  $-45^\circ$  is 512 x 512 pixels. Rotating this to the  $0^\circ$  aspect plane results in an overlapping region of 363 x 363 pixels. Figure 10 shows this down-sizing of the images caused by rotation.

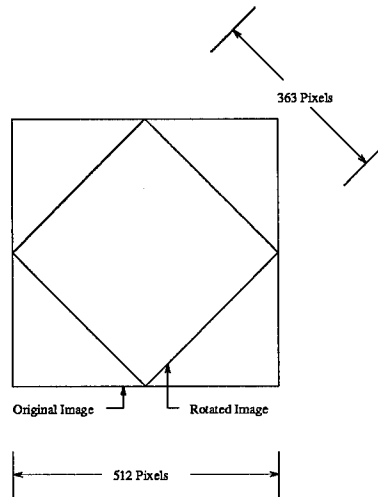


Figure 10. Overlap of Rotated Image

The second cause of information loss is due to the fact that the images are discrete and the information between samples is not available for use in rotating the images [25]. Sumner [25] developed an interpolation rotation algorithm that compensated for this lost information. However, this algorithm is computationally prohibitive and provides minimal

advantage over the nearest neighbor rotation method. Accordingly, the multiple aspect angle images of all the XPATCH-ES data sets used in this research were co-registered using the nearest neighbor rotation method. Figure 11, shows Data Set 1 after rotation.

The XPATCH-ES program generates a ground truth map for every target scene. The ground truth map shows the locations of targets, trees, roads and other elements of a target scene. Figure 12 provides a legend of these typical items. The ground truth map for Data Set 1 can be seen at Figure 13.

## *2.9 Summary*

In this chapter we reviewed the literature relating to polarimetric processing, target detection and clutter statistics. The two metrics, S/M and T/C, that will be used to quantify the performance of the polarimetric and WASAR algorithms were defined. We then reviewed the statistics and common distributions of clutter and targets. The polarimetric XPATCH-ES WASAR data was also discussed. Then we developed the algorithms that will be used to combine the polarimetric and WASAR images into the one intensity image that will be used for target detection. The multiple aspect images were co-registered to the  $0^\circ$  aspect angle using the nearest neighbor method. In Chapter IV we will apply the algorithms developed in this chapter to the XPATCH-ES WASAR data.

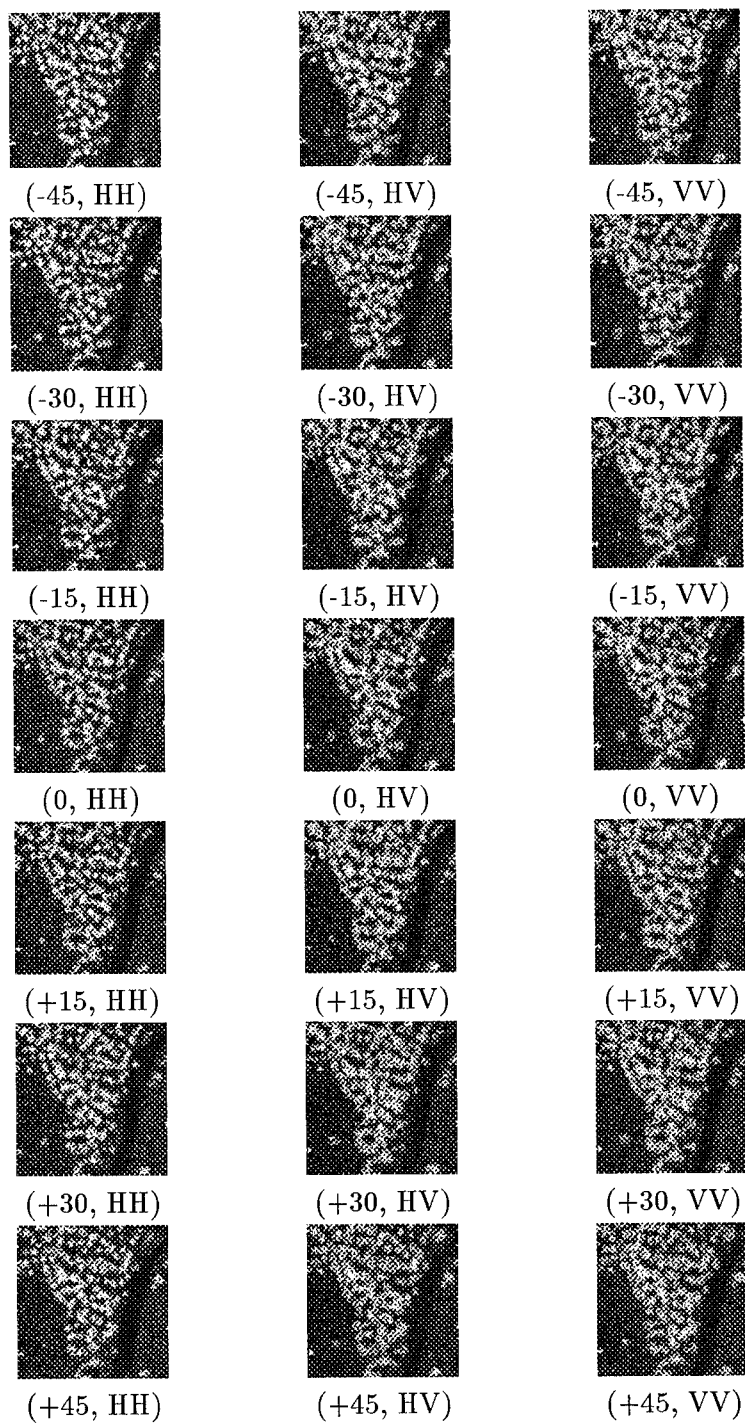


Figure 11. Data Set 1 After Rotation

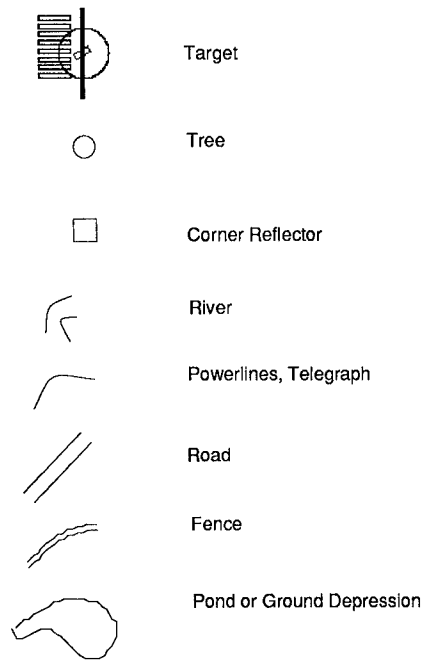


Figure 12. Legend of typical items in a target scene.

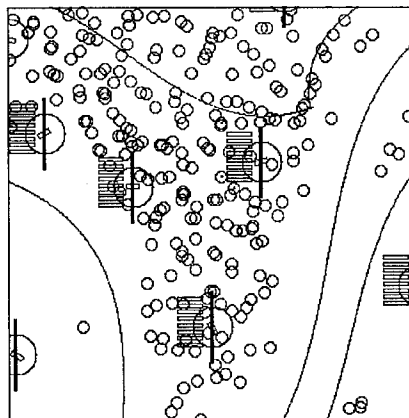


Figure 13. Ground truth map for Data Set 1 (6 targets).

### *III. Statistical Analysis of XPATCH-ES Data and Clutter Models*

#### *3.1 Introduction*

In this chapter a statistical analysis, feature extraction, and a target and clutter analysis is performed of the data used in this research. The statistical analysis involves determining the distribution of the clutter and targets and, estimating the mean, variance and covariance matrices (polarimetric and wide angle covariance matrices). In this work, feature extraction involves the characterization of attributes of the fully polarimetric WASAR data that will assist in discriminating targets from clutter, such as size, power, spatial distribution etc. The target and clutter analysis is a combination of both the feature extraction and statistical analysis. Characteristics of targets and clutter are investigated such as phase, 2-D correlation, ROC curves, distribution and different terrain categories. Polarimetric and wide angle covariance matrices are estimated for the targets and the different terrain categories, e.g. grass, trees etc. In addition, clutter models of various statistical distributions are analyzed and generated. Generating clutter of different distributions is useful for testing target detection algorithms for targets embedded in clutter of different terrain categories.

#### *3.2 Statistical Analysis of Data*

The statistical analysis performed on the data involved the following procedures. First, the distributions of the targets and clutter of each data set were determined. Next, estimates of the mean and variance of the pixel intensities were computed. Then, S/M and T/C ratios were calculated. Finally, sample estimates of the polarimetric and multiple

angle covariance matrices for the clutter ( $\Sigma_c$ ), targets ( $\Sigma_t$ ) and targets + clutter ( $\Sigma_x$ ) were computed.

*3.2.1 Determining Target and Clutter Distributions.* The pdf of each class (target and clutter) can be estimated by parametric or non-parametric methods. The parametric approach is less complicated than the non-parametric and involves the estimation of parameters such as the mean and variance. Then, if the targets or clutter have a density function that is completely characterized by a set of parameters, such as the normal and log-normal densities, which are characterized by the mean and variance, then pdfs of the target class and clutter can be formed by using estimates of the parameters that characterize the density functions. In the non-parametric approach the density function is estimated by a small number of neighboring samples. Two common types of non-parametric estimation techniques used are the Parzen density estimate and the k-nearest neighbor estimate [5]. The parametric method of estimating the pdfs was used in this work.

*3.2.1.1 Clutter Distribution.* A vector of clutter pixel intensities is formed by extracting the targets from the image using the method detailed in Section 2.7. This vector, which contains the clutter pixels for the entire image, is histogrammed with the aim of determining the distribution of the clutter. A parametric approach for estimating the density of the clutter is adopted. The sample mean and variance for both data sets are computed (refer Table 1). These values are then used to form Gaussian, Rayleigh, log-normal and Weibull pdfs. The equations for these pdfs are at Section 2.6. The pdfs are then plotted over the clutter histogram. Figure 14 shows the histograms of the clutter pixel intensities for both data sets with overlaid plots of a Weibull pdf (with shape parameters

$\eta = 1.5$  and  $\nu = 0.1$ ) and a log-normal pdf. The log-normal pdf was the best fit to the clutter histogram of the pixel intensities (especially for the tail of the histogram) of all the pdfs tested. Different images (i.e. images of the same target scenes at different aspect angles and polarizations) are tested yielding similar results. Accordingly, the distribution of the amplitude of the clutter pixel intensities for both data sets is log-normal. A plot of the log-normal clutter pdfs for both data sets are shown in Figure 16. Smaller areas within the image, that contain different types of terrain, are analyzed in Section 3.4 to determine their distribution.

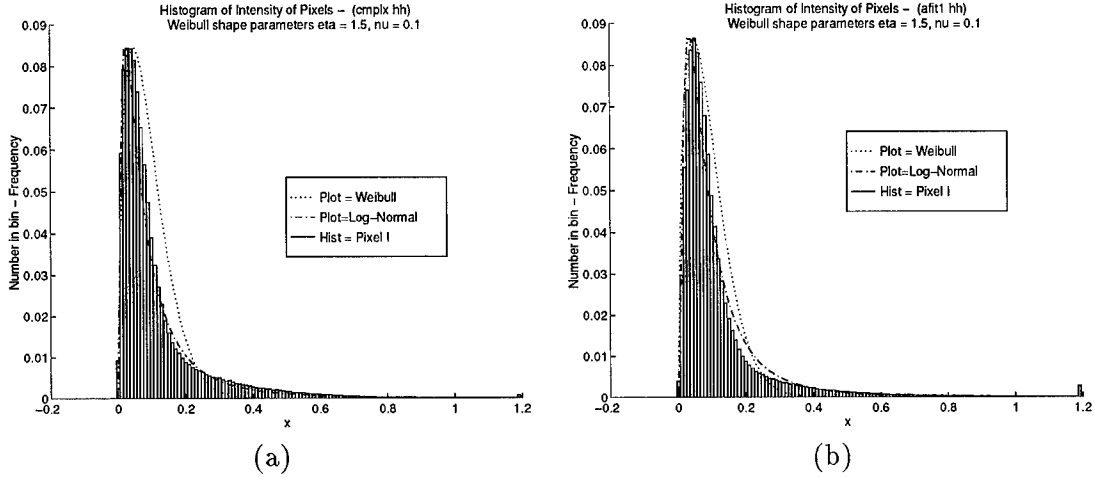


Figure 14. Histograms of clutter pixel intensities. (a) Data Set 1, and (b) Data Set 2.

### 3.2.1.2 Target Distribution.

The distribution of the targets within the target scene was determined by the same procedure outlined above and using a target template of 16 x 10 pixels around the known locations of the targets. Figure 15 shows the histograms of the target pixels with overlaid plots of Weibull and log-normal pdfs. The distribution of the target pixel intensities was also determined to be log-normal. Plots of both target and clutter pdfs for both data sets are at Figure 16. The discrimination of



targets from clutter increases ( $P_{fa}$  decreases) as the distance between target and clutter pdfs is increased. As can be seen in Figure 16, the target and clutter pdfs are almost overlaid. Accordingly, for the unprocessed images the detection of targets embedded in clutter is an important problem.

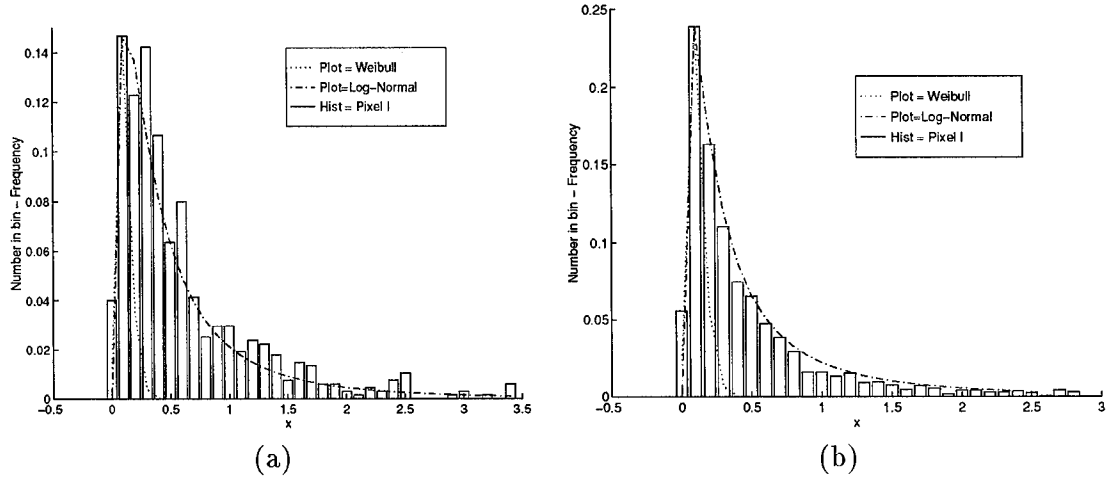


Figure 15. Histograms of the target pixel intensities. (a) Data Set 1, and (b) data Set 2.

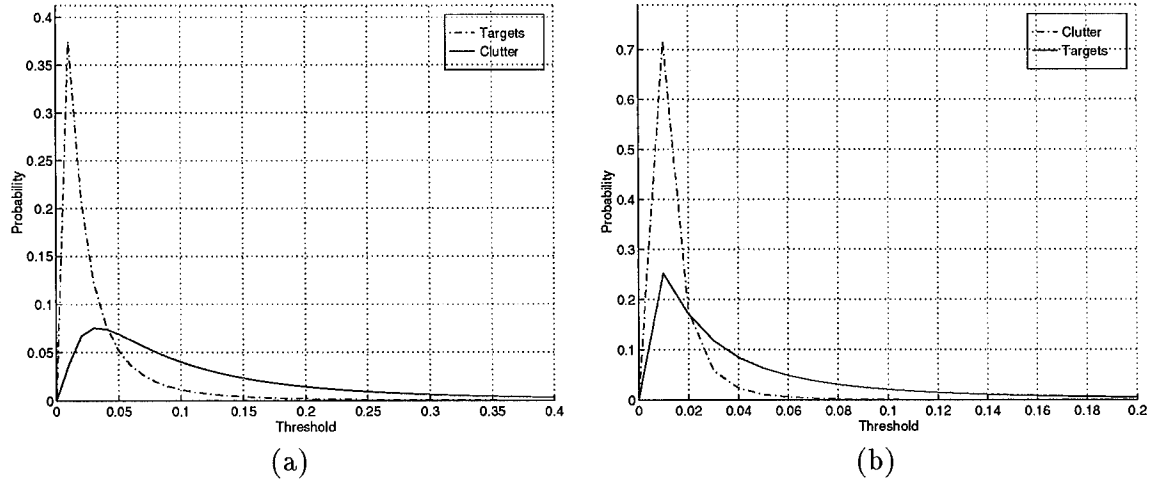


Figure 16. Target and clutter pdfs for: (a) Data Set 1, and (b) Data Set 2.

Table 1. Sample Estimates of Target and Clutter Means and STDs for both Data Sets

		Mean	STD
Data Set 1	Target	0.1437	0.1450
	Clutter	0.0294	0.0342
Data Set 2	Target	0.0548	0.1001
	Clutter	0.0095	0.0129

*3.2.2 Estimates of the Mean and Standard Deviation of Pixel Intensities.* The mean of a group of pixels in a region of interest is a statistical measure of the average pixel intensity, and the sample mean was computed using Equation 9. The standard deviation of the data within a region of interest is a measure of fluctuations of the pixel intensities, and the sample standard deviation was computed using Equation 10. Table 1 lists the estimates of the standard deviation and mean, for both target and clutter classes, for the normalized images of both data sets. These results show that both the targets' standard deviation and mean are significantly higher than the standard deviation and the mean of the clutter. Hence, the mean and standard deviation appear to be *good* discriminating features. The performance of the mean and the standard deviation as discriminating features shall be tested in Section 3.3.

*3.2.3 Standard Deviation to Mean (S/M) Ratios.* The standard deviation to mean ratios were calculated for each of the different polarimetric images at the different aspect angles using estimates for the mean and standard deviation, Equations 9 and 10. Table 2 lists the standard deviation to mean ratios for each unprocessed polarimetric image at the various aspect angles. These results show that there is a large variation in the S/M ratios of the images at different aspect angles and polarizations.

Table 2. S/M Ratios for Data Set 1

	Angle (degrees)						
Poles	- 45	- 30	-15	0	+ 15	+ 30	+ 45
HH	4.34	2.86	2.92	10.36	5.16	5.38	3.34
HV	2.62	2.76	2.36	3.62	2.37	3.88	4.56
VV	2.85	3.06	3.98	6.19	3.29	5.88	6.07

Table 3. T/C Ratios for Data Set 1 (dB)

	Angle (degrees)						
Pole	- 45	- 30	-15	0	+ 15	+ 30	+ 45
HH	13.10	10.34	9.52	16.43	13.81	14.38	10.17
HV	8.91	9.97	5.05	10.18	6.37	11.73	12.61
VV	10.06	11.04	11.24	13.21	10.24	13.88	13.7

*3.2.4 Target to Clutter (T/C) Ratios.* The target to clutter ratios were calculated for the different polarimetric images at the different aspect angles using Equation 11 and a target pixel window size of 16 pixels by 10 pixels. Table 3 lists these T/C ratios for the different images of the target scene. These results combined with the S/M ratio results (Table 2) show that target return strength is a function of angle. That is, a target might be easily detectable at one angle or polarization and obscured at another. The fully polarimetric WASAR enhances target detectability by offering multiple looks of the target scene at different aspect angles and polarizations. These early results justify further research into WASAR and reinforce the need for a radar system that provides the capability of multiple looks at a target scene.

*3.2.5 Target and Clutter Polarimetric and Wide Angle Covariance Matrices.* The covariance matrix characterizes the statistical relationship between the random variables in a multivariate process. For this research, two different covariance matrices will be used: the Polarimetric Covariance Matrix (PCM); and the Wide Angle Covariance Matrix (WACM).

The covariance matrix is defined as  $\Sigma_X = E\{XX^\dagger\}$ , where  $X$  is the measurement vector and consists of either polarimetric ( $X=[x_{hh}, x_{hv}, x_{vv}]$ ) or wide angle ( $X=[x_{-45^\circ}, x_{-30^\circ}, x_{-15^\circ}\dots]$ ) measurements. The sample estimate of the covariance matrix is

$$\Sigma_X = \frac{1}{N} \sum_{k=1}^N (X_k - \widehat{\mu}_x)(X_k^* - \widehat{\mu}_x^*)^T \quad (29)$$

where  $\widehat{\mu}_x$  is the sample mean (Equation 9). Equation 29 is a biased estimate of the covariance matrix. The unbiased estimate for the covariance matrix is  $\Sigma_X = \frac{1}{N-1} \sum_{k=1}^N (X_k - \widehat{\mu}_x)(X_k - \widehat{\mu}_x)^T$ . However, for this research  $N$  is very large, thus there is no appreciable difference in the result between the two estimates. Hence, all the estimates of the covariance matrices for this work were computed using Equation 29. The polarimetric covariance matrices have been normalized with respect to the top left element ( $E\{|HH|^2\}$ ). This was done so that any unusual features in the data such as a large return in the HV or VV images could be related to the HH return, e.g  $E\{|VV|^2\} = 1.5E\{|HH|^2\}$ .

### 3.2.5.1 Polarimetric Covariance Matrix. Estimates for the PCM for Data

Set 1 and 2, respectively, are shown below

$$\Sigma_{X-polarDS1} = 0.0436 \begin{bmatrix} 1.00 + j0.00 & -0.0011 + j0.0637 & 0.0014 + j0.1012 \\ -0.0011 - j0.0637 & 0.3194 + j0.00 & 0.0347 + j0.0221 \\ 0.0014 - j0.1012 & 0.0347 - j0.0221 & .8104 + j0.00 \end{bmatrix}$$

Table 4. Correlation coefficients between polarizations

Data set	$\rho_{hh-hv}$	$\rho_{hh-vv}$	$\rho_{hv-vv}$
Data Set 1	0.1128	0.1124	0.0808
Data Set 2	0.1131	0.1593	0.0453

$$\Sigma_{X-polarDS2} = 0.0532 \begin{bmatrix} 1.00 + j0.00 & 0.0135 - j0.0460 & -0.1008 - j0.0692 \\ 0.0135 + j0.0460 & 0.1797 + j0.00 & 0.0124 - j0.0079 \\ -0.1008 + j0.1012 & 0.0124 + j0.0079 & .5893 + j0.00 \end{bmatrix}.$$

Referring to both covariance matrices the off diagonal terms are relatively smaller than the diagonal elements. This is in line with published results. Novak [15], set the off diagonal elements to zero for a Gaussian polarimetric clutter model in the development of the polarimetric whitening filter after analyzing polarimetric SAR clutter. From the covariance matrix the correlation between the different polarizations can be calculated using the following equation

$$\rho_{i,j} = \frac{C(i,j)}{\sqrt{C(i,i).C(j,j)}} \quad (30)$$

where  $C(i,j)$  is the  $i, j$ th element of the covariance matrix. The correlation between the HH and HV returns and the other polarization combinations for both data sets were computed from Equation 30 and are listed in Table 4. These results show a small correlation exists between the different polarizations. This result is significant for developing Gaussian polarimetric clutter models. In a Gaussian process uncorrelated random variables are independant. Accordingly, three independant Gaussian clutter generators can effectively simulate HH, HV and VV clutter. More details on clutter models shall be discussed in Section 3.5.

The PCMs estimated above were computed using the entire HH, HV and VV images, and these calculations of the PCM (using the whole image targets and clutter) will be used to combine the polarimetric images using the PWF. PCMs can also be formed to analyze the targets and different terrain categories such as trees and ground clutter. A polarimetric covariance analysis of targets and clutter could reveal polarimetric features in the data that can be used to discriminate targets from clutter false alarms. Figure 17 shows images of a target (close up), trees and ground clutter.

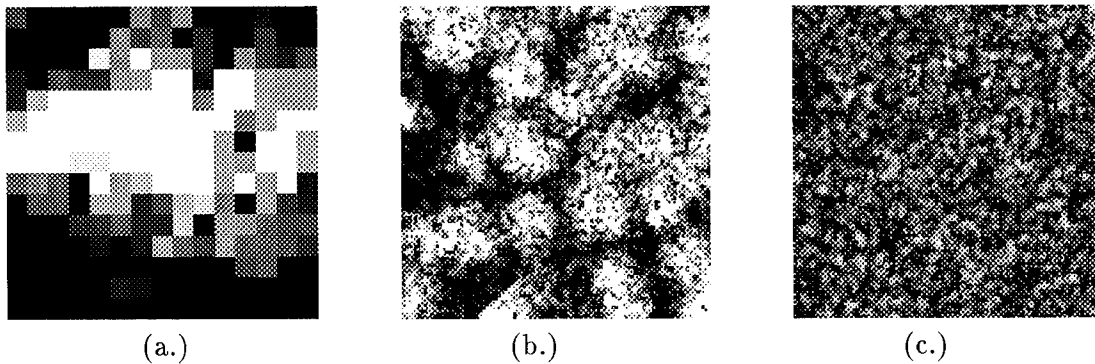


Figure 17. Images of Specific Terrain Features: a) Target, b) Trees, and c) Grass

The PCMs for targets, trees and grass were computed using Equation 29 and by using the same image segments in the HH, HV and VV images. The target polarization covariance matrix was computed by forming a target vector of all five targets for each polarization. The  $-45^\circ$  HH, HV and VV images of WASAR Data Set 1 were used to compute the target, tree and ground clutter PCMs. Other polarimetric sets (different aspect angles) within Data Set 1 were tested yielding similar results. The target, tree and

ground clutter PCMs are presented below.

$$\Sigma_{X-polarTarget} = 0.6838 \begin{bmatrix} 1.00 + j0.00 & 0.1120 + j0.1420 & 0.2447 + j0.1333 \\ 0.1120 - j0.1420 & 0.1445 + j0.00 & 0.0165 + j0.0057 \\ 0.2447 - j0.1333 & 0.0165 - j0.0057 & .4423 + j0.00 \end{bmatrix}$$

$$\Sigma_{X-polarTrees} = 0.0572 \begin{bmatrix} 1.00 + j0.00 & 0.0125 + j0.0899 & -0.0331 + j0.1379 \\ 0.0125 - j0.0899 & 0.4360 + j0.00 & 0.0582 + j0.0105 \\ -0.0331 - j0.1379 & 0.0582 - j0.0105 & .9730 + j0.00 \end{bmatrix}$$

$$\Sigma_{X-polarGround} = 0.0069 \begin{bmatrix} 1.00 + j0.00 & 0.0089 - j0.0698 & 0.2399 - j0.1846 \\ 0.0089 + j0.0698 & 0.3243 + j0.00 & 0.0345 - j0.0170 \\ 0.2399 + j0.1846 & 0.0345 + j0.0170 & .8398 + j0.00 \end{bmatrix}$$

The polarimetric covariance parameters of the man made targets are considerably different from those of trees and ground clutter. The most obvious parameter difference in the polarization-covariance matrix between targets and clutter is the  $E\{|HH|^2\}$  parameter. The targets  $E\{|HH|^2\}$  is one order of magnitude larger than trees and two orders of magnitude larger than ground clutter. Accordingly, as is expected, the detection of targets surrounded by trees is considerably more difficult than detecting a target in ground clutter. For a single image  $E\{|HH|^2\}$  is the variance. This is the square of the standard deviation. In Section 3.2.2 the standard deviation of targets was shown to be significantly larger for targets than clutter. The PCM statistically reinforces this result.

Table 5. Correlation coefficients between polarizations for Targets, Trees and Grass

Data set	$\rho_{hh-hv}$	$\rho_{hh-vv}$	$\rho_{hv-vv}$
Targets	0.4740	0.4190	0.0687
Trees	0.1375	0.1438	0.0908
Grass	0.1236	0.3304	0.0737

Another interesting observation regarding the target and clutter PCMs is the overall structure of the matrices. The target PCM has significant values for all parameters in the covariance matrix. In contrast, the off diagonal elements of the clutter PCMs (both tree and ground clutter) are almost zero. The clutter PCMs have a definite structure. (As previously stated, this result is in line with published results.)

The final observation regarding the PCM parameters of targets and clutter, is that the HV return ( $E\{|HV|^2\}$ ) is lower for targets than for clutter i.e.  $E\{|HV|^2\} = 0.14E\{|HH|^2\}$ . Other polarimetric data sets were analyzed yielding the same result. This low HV return is probably due to the physical structure of the man made targets.

The polarimetric correlation coefficients for targets, trees and grass were computed from their respective PCMs using Equation 30. The results are listed in Table 5. These results show that the HV and the VV returns for targets, trees and grass are uncorrelated. Further, the correlation coefficient for the HH-HV returns is higher for targets than both grass and trees. Accordingly, the HH-HV correlation coefficient could be a suitable feature to discriminate targets from clutter false alarms. This polarimetric discriminating feature shall be investigated in Section 3.3.

### 3.2.5.2 Wide Angle Covariance Matrix (WACM). An estimate for the

sample WACM was computed from Equation 30, where the measurement vector  $X$  was



formed from measurements taken at different aspect angles ( $X=[x_{-45^\circ}, x_{-30^\circ}, x_{-15^\circ} \dots]$ ).

The WACM of the entire image (computed using the HH data set) is shown below

$$\Sigma_{X-WACM} = 0.0436 \begin{bmatrix} 0.8996 & 0.0088 & 0.0290 & 0.0211 & 0.0057 & 0.0047 & 0.0089 \\ 0.0088 & 0.8565 & 0.0127 & 0.0101 & 0.0067 & 0.0075 & 0.0113 \\ 0.0290 & 0.0127 & 0.8885 & 0.0123 & 0.0102 & 0.0077 & 0.0064 \\ 0.0211 & 0.0101 & 0.0123 & 1.0000 & 0.0228 & 0.0117 & 0.0031 \\ 0.0057 & 0.0067 & 0.0102 & 0.0228 & 0.9222 & 0.0369 & 0.0155 \\ 0.0047 & 0.0075 & 0.0077 & 0.0117 & 0.0369 & 0.9620 & 0.0014 \\ 0.0089 & 0.0113 & 0.0064 & 0.0031 & 0.0155 & 0.0014 & 0.8289 \end{bmatrix}.$$

The WACM is a complex matrix and for all of the WASAR algorithms the complex form of the WACM was used, however for display purposes only the magnitude of the WACM is shown. The WACM has been normalized to the zero degree aspect return. The most significant feature of the angle covariance matrix, is that it is almost a diagonal matrix. That is, the off diagonal elements in all directions are almost zero (e.g. 0.0088, 0.0290 etc.). The HV and VV WASAR sets within Data Set 1 were tested yielding similar results. The correlation between angles was computed using Equation 30, and the results are listed in Table 6.

WACMs were computed for targets, trees and grass and the results are shown below.

Table 6. Correlation coefficients between aspect angles for Clutter plus targets (whole image)

Angle	Angle						
	$-45^\circ$	$-30^\circ$	$-15^\circ$	$0^\circ$	$+15^\circ$	$+30^\circ$	$+45^\circ$
$-45^\circ$	1	0.0100	0.0324	0.0222	0.0062	0.0050	0.0104
$-30^\circ$	0.0100	1	0.0145	0.0109	0.0075	0.0083	0.0134
$-15^\circ$	0.0324	0.0145	1	0.0130	0.0113	0.0083	0.0074
$0^\circ$	0.0222	0.0109	0.0130	1	0.237	0.0119	0.0034
$+15^\circ$	0.0062	0.0075	0.0113	0.0237	1	0.0391	0.0178
$+30^\circ$	0.0050	0.0083	0.0083	0.0119	0.0391	1	0.0016
$+45^\circ$	0.0104	0.0134	0.0074	0.0034	0.0178	0.0016	1

$$\Sigma_{X-WACMTargets} = 1.5684 * \begin{bmatrix} 0.4360 & 0.0187 & 0.0921 & 0.0528 & 0.0536 & 0.0483 & 0.0241 \\ 0.0187 & 0.2433 & 0.0543 & 0.0361 & 0.0413 & 0.0258 & 0.0487 \\ 0.0921 & 0.0543 & 0.2126 & 0.0422 & 0.0621 & 0.0167 & 0.0121 \\ 0.0528 & 0.0361 & 0.0422 & 1.0000 & 0.1165 & 0.0817 & 0.0492 \\ 0.0536 & 0.0413 & 0.0621 & 0.1165 & 0.5482 & 0.1811 & 0.0637 \\ 0.0483 & 0.0258 & 0.0167 & 0.0817 & 0.1811 & 0.5708 & 0.0434 \\ 0.0241 & 0.0487 & 0.0121 & 0.0492 & 0.0637 & 0.0434 & 0.2191 \end{bmatrix}$$

$$\Sigma_{X-WACMTrees} = 0.0636 * \begin{bmatrix} 0.9002 & 0.0108 & 0.0542 & 0.0062 & 0.0126 & 0.0259 & 0.0288 \\ 0.0108 & 1.0791 & 0.0420 & 0.0239 & 0.0280 & 0.0520 & 0.0151 \\ 0.0542 & 0.0420 & 1.0248 & 0.0149 & 0.0208 & 0.0248 & 0.0253 \\ 0.0062 & 0.0239 & 0.0149 & 1.0000 & 0.0289 & 0.0098 & 0.0213 \\ 0.0126 & 0.0280 & 0.0208 & 0.0289 & 0.9990 & 0.0189 & 0.0371 \\ 0.0259 & 0.0520 & 0.0248 & 0.0098 & 0.0189 & 1.0105 & 0.0305 \\ 0.0288 & 0.0151 & 0.0253 & 0.0213 & 0.0371 & 0.0305 & 0.9594 \end{bmatrix}$$

$$\Sigma_{X-WACMGrass} = 0.0062 * \begin{bmatrix} 1.1042 & 0.0270 & 0.0281 & 0.0011 & 0.0220 & 0.0231 & 0.0430 \\ 0.0270 & 1.0010 & 0.0184 & 0.0203 & 0.0219 & 0.0215 & 0.0100 \\ 0.0281 & 0.0184 & 0.9496 & 0.0168 & 0.0105 & 0.0181 & 0.0117 \\ 0.0011 & 0.0203 & 0.0168 & 1.0000 & 0.0219 & 0.0214 & 0.0160 \\ 0.0220 & 0.0219 & 0.0105 & 0.0219 & 0.9706 & 0.0259 & 0.0257 \\ 0.0231 & 0.0215 & 0.0181 & 0.0214 & 0.0259 & 1.0059 & 0.0351 \\ 0.0430 & 0.0100 & 0.0117 & 0.0160 & 0.0257 & 0.0351 & 1.0398 \end{bmatrix}$$

Referring to the WACMs of the targets, trees and grass the following observations are made. First, the  $E\{|X_0|^2\}$  (variance) of the targets is significantly larger for man

made targets than for trees and grass. This discriminating feature was also observed in the PCM analysis. Second, the return at different aspect angles relative to the  $0^\circ$  aspect angle (diagonal elements of WACM) varies considerably for targets, whereas for all clutter the returns at different aspect angles remained constant (at approximately one). An examination of the diagonals of each of the WACMs reveals that for trees and ground clutter, the diagonal elements are all approximately the same, whereas the diagonal elements of the target WACM vary. In both the trees and the grass the return at different aspect angles is the same. Figure 18 is a plot of the relative return of targets, trees and grass at different aspect angles. This result proves the assumption that clutter is invariant to changes in aspect angle. In other words, clutter has a constant return over different aspect angles, however, targets (due to their different physical properties) produce a varying return for different aspect angles. A tree looks the same from any angle, however, a target looks considerably different at even small aspect angle changes (i.e  $15^\circ$ ).

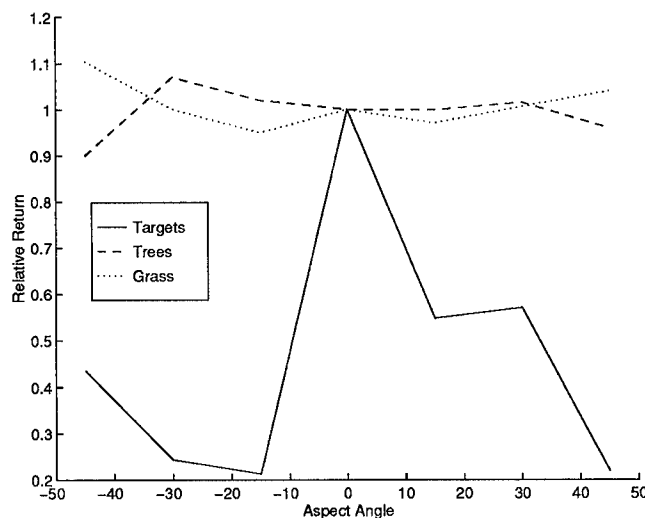


Figure 18. Plot of Relative Return versus Aspect Angle for Targets, Trees and Grass

Table 7. Correlation coefficients between aspect angles for Targets only

Angle	Angle						
	$-45^\circ$	$-30^\circ$	$-15^\circ$	$0^\circ$	$+15^\circ$	$+30^\circ$	$+45^\circ$
$-45^\circ$	1	0.057	0.303	0.080	0.110	0.100	0.078
$-30^\circ$	0.057	1	0.239	0.073	0.113	0.069	0.211
$-15^\circ$	0.303	0.239	1	0.091	0.182	0.048	0.056
$0^\circ$	0.080	0.073	0.091	1	0.157	0.108	0.105
$+15^\circ$	0.110	0.113	0.182	0.157	1	0.324	0.184
$+30^\circ$	0.097	0.069	0.048	0.108	0.324	1	0.1223
$+45^\circ$	0.078	0.211	0.056	0.105	0.184	0.123	1

Table 8. Correlation coefficients between aspect angles for Trees only

Angle	Angle						
	$-45^\circ$	$-30^\circ$	$-15^\circ$	$0^\circ$	$+15^\circ$	$+30^\circ$	$+45^\circ$
$-45^\circ$	1	0.011	0.056	0.007	0.013	0.027	0.031
$-30^\circ$	0.011	1	0.040	0.023	0.027	0.050	0.015
$-15^\circ$	0.056	0.040	1	0.015	0.021	0.024	0.026
$0^\circ$	0.007	0.023	0.015	1	0.029	0.010	0.022
$+15^\circ$	0.013	0.027	0.021	0.030	1	0.019	0.038
$+30^\circ$	0.027	0.050	0.024	0.010	0.019	1	0.031
$+45^\circ$	0.031	0.015	0.026	0.022	0.038	0.031	1

The correlation between aspect angles for targets, trees and grass were computed and are listed in Tables 7, 8 and 9. From these it can be seen that the clutter returns (both trees and grass) are uncorrelated between the different aspect angles, whereas the targets are slightly correlated between aspect angles.

Table 9. Correlation coefficients between aspect angles for Grass only

Angle	Angle						
	$-45^\circ$	$-30^\circ$	$-15^\circ$	$0^\circ$	$+15^\circ$	$+30^\circ$	$+45^\circ$
$-45^\circ$	1	0.025	0.027	0.001	0.021	0.022	0.040
$-30^\circ$	0.026	1	0.019	0.020	0.022	0.021	0.009
$-15^\circ$	0.027	0.019	1	0.017	0.011	0.019	0.012
$0^\circ$	0.001	0.020	0.017	1	0.022	0.021	0.016
$+15^\circ$	0.021	0.022	0.011	0.022	1	0.026	0.026
$+30^\circ$	0.022	0.021	0.019	0.021	0.026	1	0.034
$+45^\circ$	0.040	0.009	0.012	0.016	0.026	0.034	1

*3.2.6 Summary of Statistical Analysis.* The statistical analysis performed on the data highlighted many discriminating features that would assist in the separation of targets from clutter. From the limited amount of data processed the following conclusions appear to hold. The standard deviation was found to be the most promising discriminating feature. It was shown through a direct computation of the standard deviation, that a target's standard deviation was significantly larger than the standard deviation for clutter (refer Table 1).

Further, the large difference between clutter and a target's standard deviation was highlighted in the analysis of polarimetric and wide angle covariance matrices. The distribution of targets and clutter for both data sets was shown to be log-normal. The polarimetric covariance parameters of the targets were shown to be different to that of clutter. The form of the polarimetric covariance matrix of the XPATCH-ES data was in line with published results [15]. The wide angle covariance analysis showed that the relative return strength for clutter was constant at different aspect angles, whereas the returns from the targets varied considerably at different aspect angles. That is, a tree looks the same at different aspect angles, however, a target looks considerably different.

### *3.3 Feature Extraction*

Feature extraction or feature selection is generally used in target recognition systems and is a process of mapping the original measurements into more effective features. The focus of this research is target detection. Notwithstanding, to discriminate targets from clutter, attributes of the fully polarimetric WASAR data that will effectively separate the two classes in the target detection problem must be investigated and exploited. Typical

attributes include size, shape, power, polarimetric properties and spatial distribution [4]. To select a suitable discriminating feature each feature is tested on the data to see if it effectively separates targets from clutter false alarms. The feature may be a good one if it separates the two classes.

To discriminate is a front end process, i.e. it is one of the first steps involved in a target detection or target recognition system. The ability to discriminate will significantly reduce the number of clutter false alarms. Figure 19 is a block diagram of the WASAR target detection system developed for this research. The system comprises four stages:

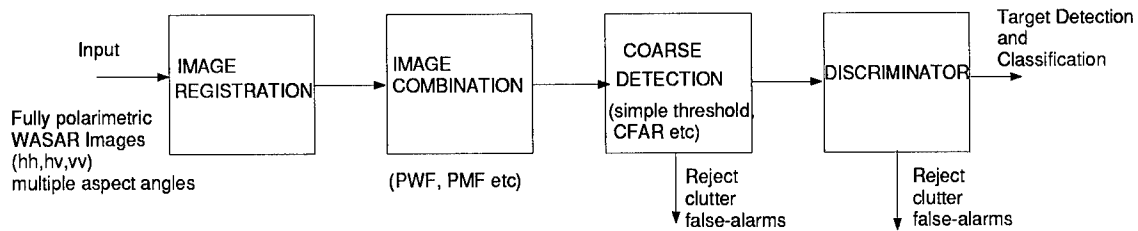


Figure 19. Block diagram of fully polarimetric WARSAR target detection system

1) image registration, 2) image combination, 3) coarse detection, and 4) discrimination. At the input there are 21 images of different polarizations and aspect angles. The first stage registers all the images to the one aspect angle. A full description of this stage was provided in Chapter II. The second stage combines the polarimetric images into the one image for coarse target detection and discrimination. The polarimetric and WASAR algorithms used to combine the registered images were derived in Chapter II. The results of detecting an image formed from different combinations of combining polarimetric and WASAR images are presented in Chapter IV. Since the function of the discriminator is to exploit characteristics of the data a description of its operation and some of the features of the registered images investigated is presented in this data analysis chapter. Specific results

of combining different combinations of polarizations and WASAR images are provided in Chapter IV.

*3.3.1 Discriminator and Specific Features Investigated.* The discriminator examines smaller regions of the registered, combined and detected image. The coarse detector isolates possible target locations and rejects lower level clutter false alarms. These smaller regions are then analyzed with respect to a number of features in order to separate the targets from the clutter. The main purpose of the discriminator, in this research, is as another method of quantifying the improvements of combining either the polarimetric or WASAR images into the one image for target detection purposes. Accordingly, the features investigated had to satisfy the following two goals: 1) clearly separate target and clutter classes, and 2) be easily and quickly computed. The features investigated included the mean, the standard deviation, the 2-Dimensional correlation co-efficient and the HH-HV correlation. The discriminating attributes of the mean and the standard deviation features were outlined in Section 3.2.2, where it was shown that both the mean and the standard deviation were larger for targets than clutter.

In Section 3.2.5.1 it was shown by an analysis of the polarimetric covariance matrix that the HH-HV correlation coefficient was larger for targets than clutter. The HH-HV correlation coefficient ( $\rho_{hh-hv}$ ) was computed by forming a 2 x 2 covariance matrix of all the segmented sub-images and  $\rho_{hh-hv}$  was calculated using Equation 30. Figure 20 illustrates the  $\rho_{hh-hv}$  standard deviation discriminator.

The 2-D correlation coefficient is the measure of correlation of a test target with a region of the target scene under test. This feature was computed by forming a binary image

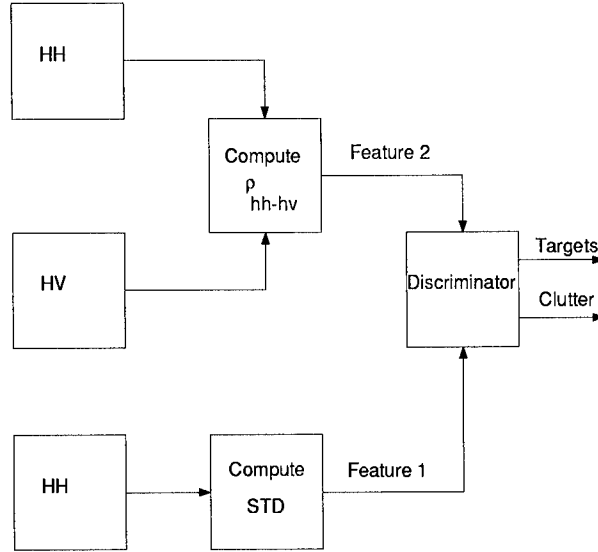


Figure 20. Block diagram of  $\rho_{hh-hv}$  standard deviation discriminator

of the original image and cross correlating the target with similar sized non-overlapping windows across the entire digital image. This process of cross correlating the image of the target over regions of interest is called matched filtering. In a more complex discriminator or target recognition system, the target would be rotated through all possible angles and cross correlated with the test image. The process of rotating the target and cross correlating with the image was avoided by making the test target a 16 x 16 matrix of ones. Thus, a 16 x 10 pixel target at any rotation angle should be detected using this larger target template. The main purpose of the 2-D correlation coefficient feature is to detect pixel clusters similar to that of the test target in order to separate targets and clutter false alarms. In this instance the focus is on target detection not recognition. The binary image was formed by thresholding the normalized image at the mean pixel intensity plus one standard deviation (0.0666) and, assigning all values below the threshold at 0 and those values above the threshold to 1. Figure 21 shows binary images of the HH image at an aspect angle of  $-45^\circ$  and a close up binary image of the target used as the target test



vector for feature extraction. The size of the test target, in the data analyzed, is 16 pixels

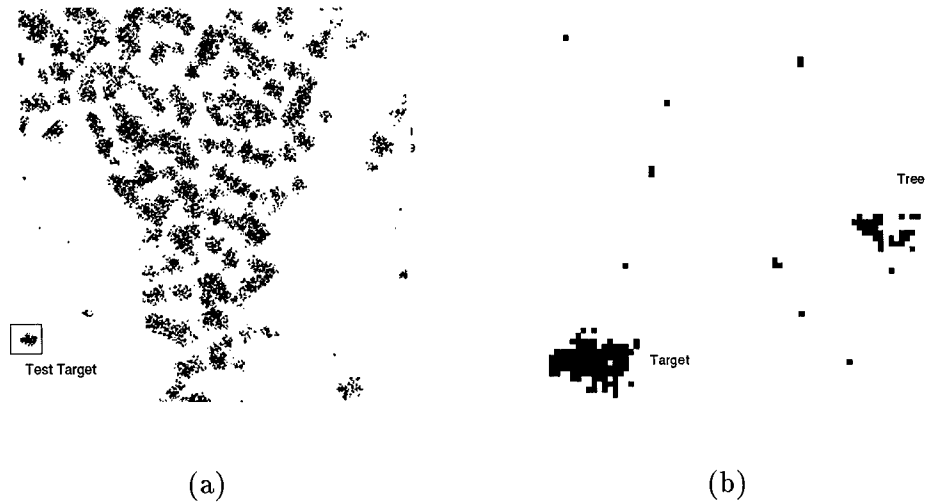


Figure 21. Binary images of: a) HH  $-45^\circ$ , and b) Target used for testing in feature extraction

long and 10 pixels wide, however, any size window can be used in the discriminator. The choice of window size depends on the size and shape of the targets being detected. Many different window sizes were tested and it was found that a smaller window, 6 x 6 was the best window size for the 2-D correlation coefficient (detect square pixel clusters), however, the standard deviation feature gave better results with larger window sizes. After testing various window sizes an engineering tradeoff between the two features was reached and a window size of 12 x 8 pixels was selected. The process of using a 12 x 8 matrix of ones (i.e. the correlator was searching for solid squares within the target scene) is a simplified version of using the fractal dimensions of an object. The fractal dimension of the pixels within a region of interest is an ideal feature that provides information about the spatial distribution of the brightest scatters of the detected objects. Forming a binary image is

the first step in computing the fractal dimension of regions under test. The computation of the fractal dimension was begun but this task is beyond the scope of this research.

As previously stated, the method of determining a *good* feature is to test it on the data to see if it effectively separates targets from clutter false alarms. The results are displayed on a plot of one feature against another. A target training vector is tested and other possible target regions that are close to the center of the target training vector, in feature space, are designated targets. Figure 22 [4] demonstrates this concept.

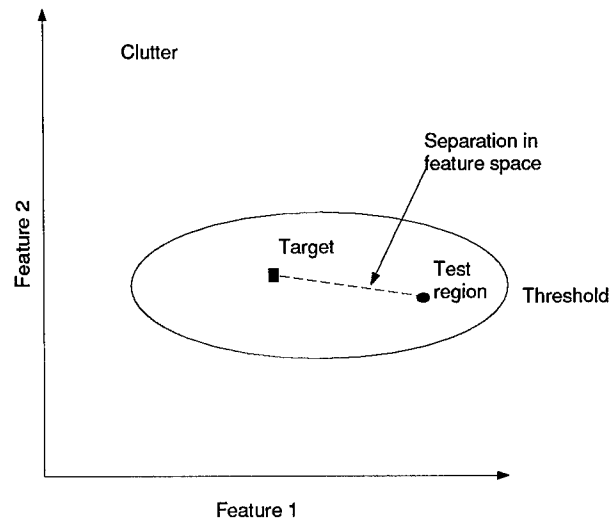


Figure 22. Diagram of simple Discriminator

The test target vector used to locate the position of the target cluster in feature space is shown in Figure 23. The image consists of a target in a grassy field (ground clutter) and one tree. The image was segmented into non-overlapping windows of 12 x 8 pixels and for each window the mean and standard deviation were computed. The plot of the mean versus the standard deviation (refer Figure 23(b)) shows that the grass, tree and target were successfully separated. On the plot the '\*' indicates the mean and variance of the region being tested, the 'x' shows the actual standard deviation and mean of the target,

the '+' shows the actual mean and standard deviation of the tree, and the 'o' (obscured) shows the actual mean and standard deviation of the ground clutter. The other feature pair combinations were tested on this same sub-image with similar promising results i.e. targets were clearly discriminated from clutter false alarms.

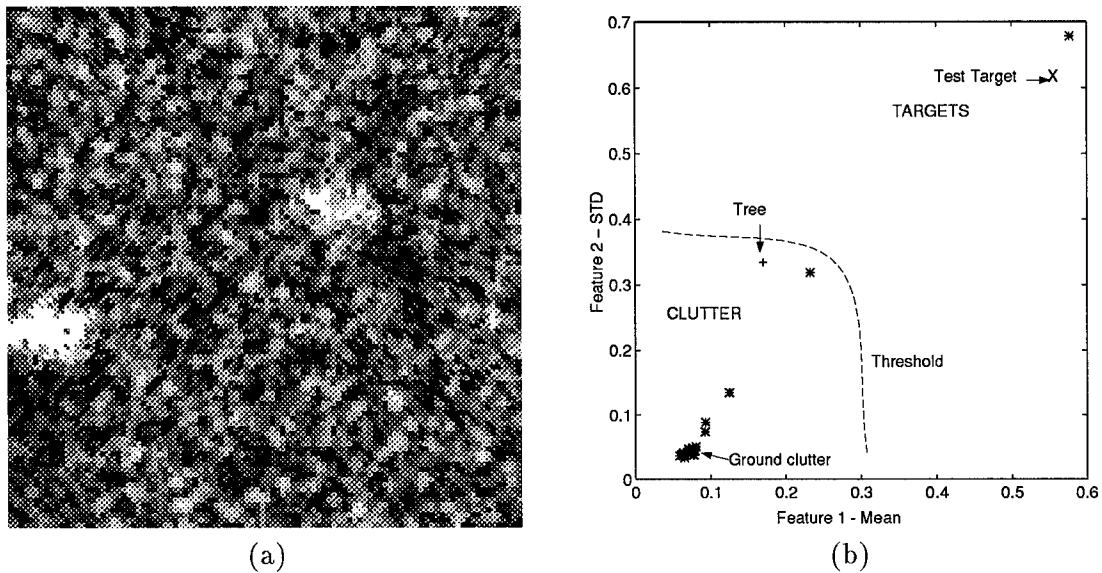


Figure 23. Discrimination of targets and clutter using the standard deviation and mean features. a) Image of a target in clutter, b) Plot of Mean vs STD

The results of testing the data against the mean, standard deviation, the 2-D correlation coefficient and the HH-HV correlation coefficient features on the entire target scene are shown in Figure 24. The HH at an aspect angle of  $-45^\circ$  was used to test for the best pair of discriminating features. For all features, targets have higher values than clutter, i.e. a target has a higher mean, standard deviation and correlation coefficient than clutter. Accordingly, in plots of one feature verses another, targets are located in the upper right

quadrant of the graph and most clutter values should appear below the targets (lower left section of graph).

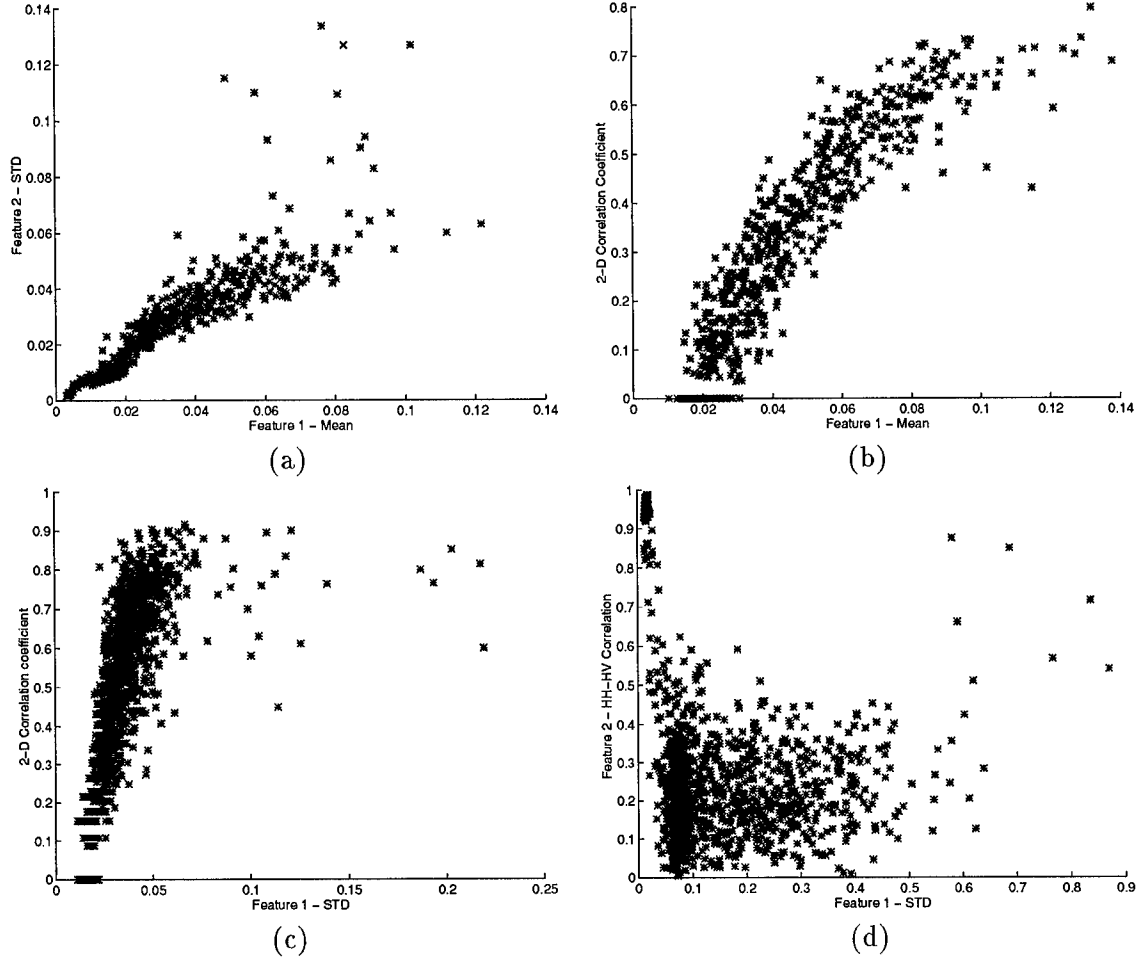


Figure 24. Feature plots (a) STD Vs Mean, (b) 2-D Corr Coefficient Vs Mean, (c) 2-D Corr Coefficient Vs STD , and (d) HH-HV Corr Coefficient Vs STD.

The image used for testing contains five targets (refer Figure 13). Referring to Figure 24, the best pair of discriminating features is the standard deviation and the 2-D correlation coefficient. The mean feature combined with either of the standard deviation, the correlation coefficient, or the HH-HV correlation coefficient does not significantly separate targets from clutter false alarms. However, the main advantage of this set of features

is that they are easily and quickly calculated. The best result for testing of the HH-HV correlation coefficient feature with the other features was with the standard deviation feature (Figure 24 (d)). This combination did separate targets (upper right corner) from clutter false alarms (lower left) but not as successfully as the standard deviation and the 2-D correlation pair. The 2-D correlation coefficient shows that future work in computing fractal dimensions for the WASAR regions of interest shows promise. The discriminator in this research will use both: the standard deviation-correlation feature pair, for their performance; and the standard deviation-mean feature pair, for their ease of computation. Full results of testing the combined polarimetric and WASAR images are presented in Chapter IV.

### *3.4 Target and Clutter Analysis*

In this section the WASAR data is further analyzed in order to extract any other features or characteristics that will enable targets and clutter to be differentiated. First, polar plots are plotted of the target and clutter pixels to investigate the phase and the magnitude of the raw data for these two classes. Next, different types of clutter is investigated with respect to distribution, and polar plots. A 2-D correlation analysis is performed on targets, trees and grass to investigate their spatial distribution. Finally, ROC curves are plotted of the unprocessed images to determine relative probabilities of detection and false alarm for the different aspect angles and polarizations.

*3.4.1 Polar Plots of Targets and Clutter.* The WASAR data are complex. That is, each image pixel can be represented as a magnitude and a phase. A simple threshold

detector distinguishes a pixel as either a target class or a clutter class depending on the magnitude of the pixel under test. If the magnitude of the pixel exceeds the threshold a target is assumed. In this type of detector the phase information is ignored. In this section an analysis of target and clutter phase information is performed.

The phase analysis simply involves the direct polar plot of the magnitude and phase of target and clutter pixels. Target and clutter pixels were separated as described in Section 2.7. Figure 25 shows polar plots of the target pixels of Data Set 1 for all aspect angles and polarizations, and Figure 26 shows the polar plot for clutter. A polar plot of the clutter pixels is at Figure 26.

A comparison of the polar plots of clutter and targets shows that clutter pixels have widely varying (random) magnitude and phase, producing a circular polar plot. In contrast, the majority of target pixels have a larger magnitude and a smaller variance of phase angles. For example, the polar plot of the target pixels of the HH  $-45^\circ$  aspect angle image shows that the phase angle of most of the pixels is approximately  $45^\circ$ . Other good examples of this observation include the VV  $+15^\circ$  image and the  $+45^\circ$  VV and HV polar plots. This phase discriminating feature was investigated, however, early results did not provide any significant discriminating performance.

*3.4.2 Target and Terrain Clutter Analysis.* In this section an analysis of different types of terrain within the target scene of Data Set 1 is presented. Targets, trees and ground clutter (grass) are analyzed to determine their distribution and phase profile. In Section 3.2.1 it was shown that the overall distribution of clutter and targets is log-normal. However, within a large target scene there can be many different types of terrain. Clutter

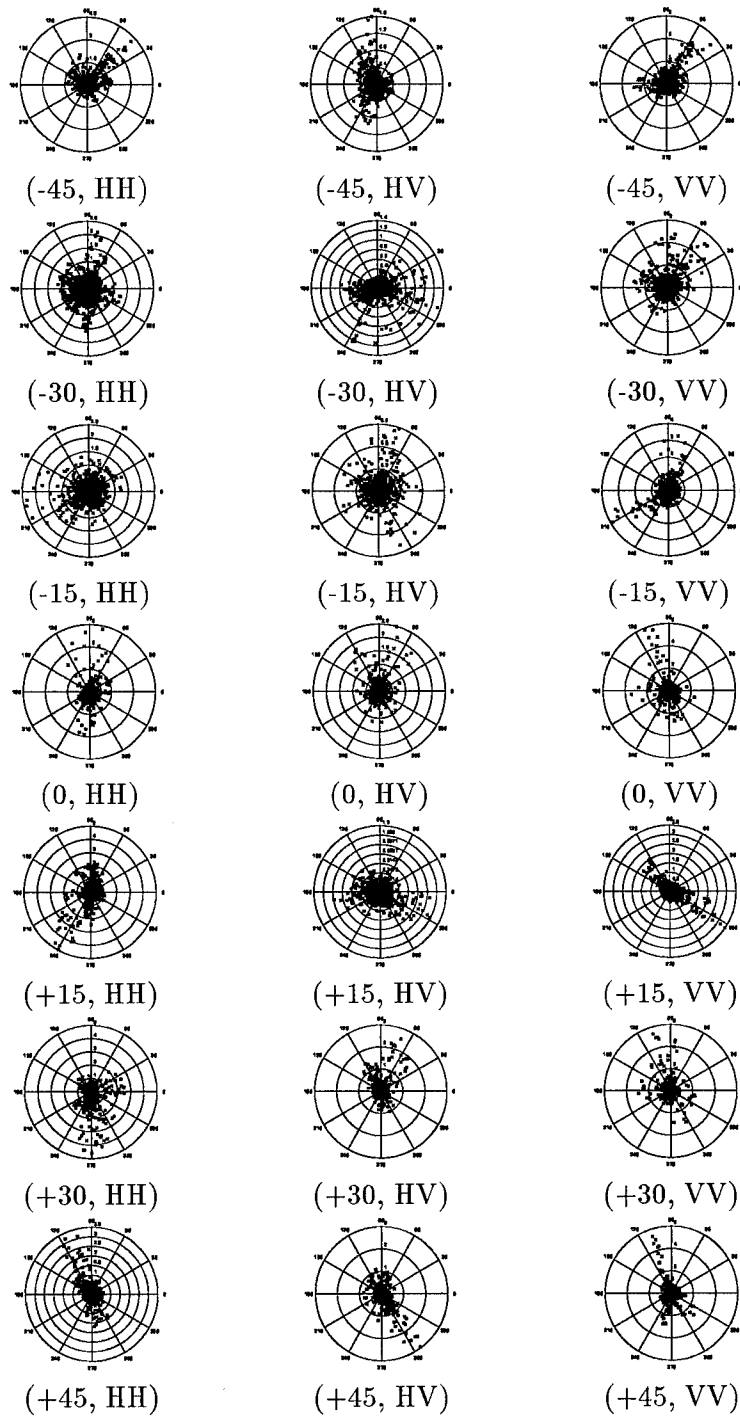


Figure 25. Polar Plots of Targets in Data Set 1

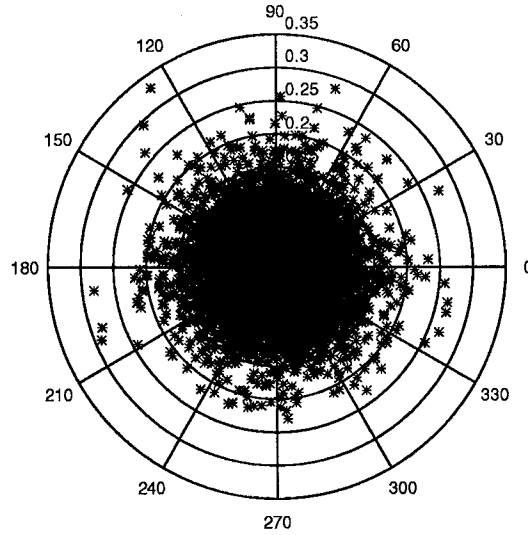


Figure 26. Polar plot of Clutter Pixels

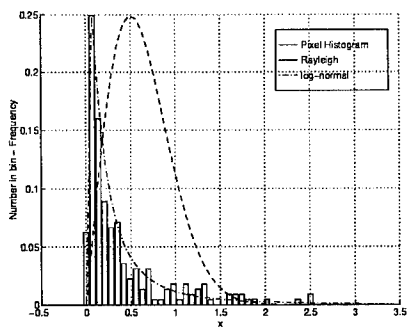
from different terrain has different statistics. A polarimetric-covariance and wide angle-covariance analysis performed in Section 3.2.5 showed that the covariance parameters of the man made targets were different to that of clutter. Using these same regions of targets, trees and grass, the pixels were histogrammed to determine their distribution and polar plots were taken to investigate their phase profile. Figure 27 shows images of the targets and clutter along with pixel intensity histograms and polar plots. This figure illustrates that the targets and trees have a log-normal distribution and the ground clutter is Rayleigh distributed. The polar plots show that both trees and grass have a uniform phase profile, whereas targets have a non-uniform phase profile.

*3.4.3 2-D Correlation analysis.* A 2-D correlation analysis of targets, trees and ground clutter was performed to investigate their spatial distribution. Figures 28 and 29 show images, 2-D mesh plots and surface plots of the 2-D autocorrelation of targets, trees

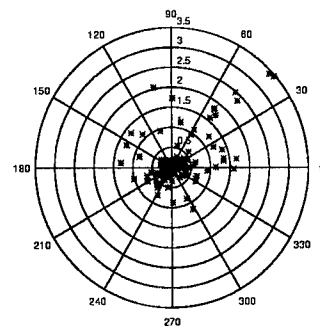




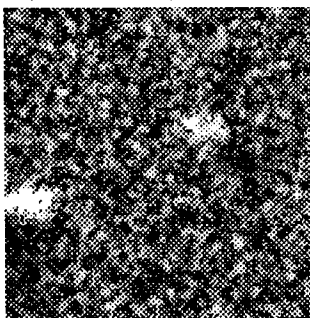
(a. Target (Close up))



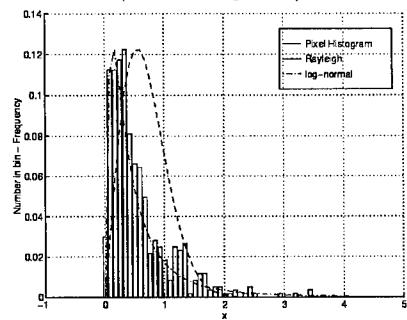
(a. Histogram)



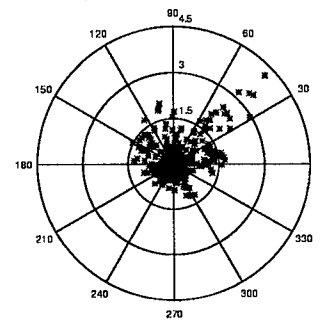
(a. Polar Plot)



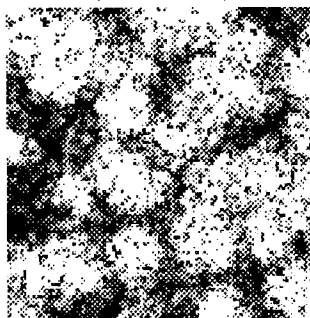
(b. Target)



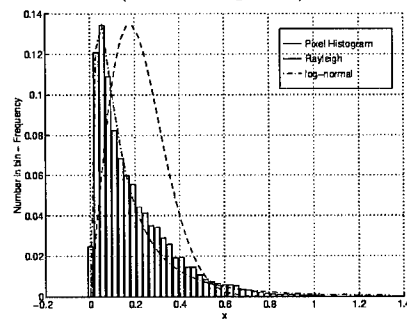
(b. Histogram)



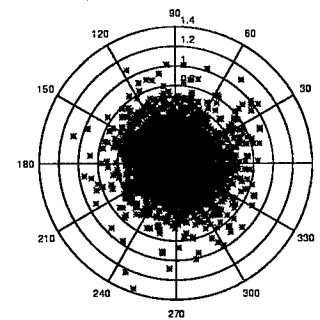
(b. Polar Plot)



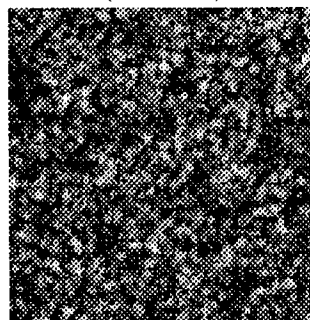
(c. Trees)



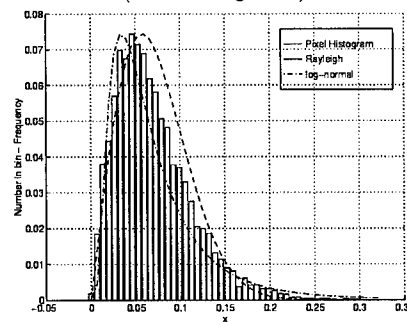
(c. Histogram)



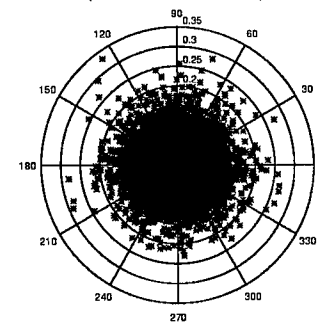
(c. Polar Plot)



(d. Ground Clutter)



(d. Histogram)

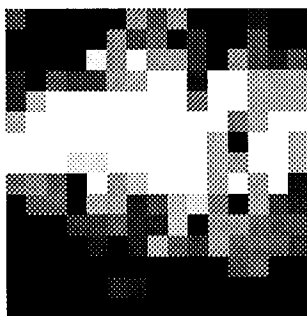


(d. Polar Plot)

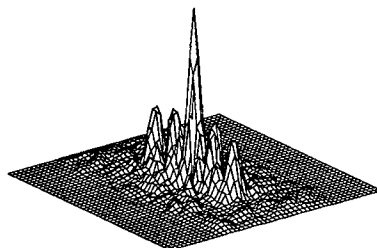
Figure 27. Terrain Clutter and Target analysis for: a) Target, b) Targets, c) Trees, and d) Ground Clutter.

and ground clutter. Referring to these figures, the targets have a unique 2-D correlation profile when compared to those of trees and ground clutter.

*3.4.4 ROC Curves.* As discussed in Section 2.5, ROC curves are plots of probability of detection ( $P_D$ ) versus probability of false alarm  $P_{fa}$ . They are used to quantify the performance of a detector. A plot of ROC curves of the unprocessed images for the different aspect angles and polarizations will show those images that have a high probability of detection and a low probability of false alarm. The further the ROC curve is above the chance line indicates the more likely targets in this image are to be detected. The ROC curves were computed by the following procedure. First, all the images were normalized so that the threshold level for the pixel intensities ranged from zero to one for all images. Next, target and clutter pixels in each image were extracted and directly histogrammed. The bins of the histograms represent the threshold level. For example, if there were 100 histogram bins, the bins would increment in threshold steps of 0.01 and the value in the target histogram vector would contain all the target pixel intensities within a particular threshold range. The target and clutter histograms were normalized such that they summed to one (i.e. discrete pdf). The probability of detection was computed by summing the bins of the target histogram from the threshold level to the end of the target histogram vector ( $P_D = \sum_{\text{thrsh}}^N \text{Targ}$ , where Targ is the vector containing the histogrammed target pixel intensities). Similarly, the probability of false alarm was computed by summing the clutter histogram vector from the threshold to the end of the clutter vector ( $P_{fa} = \sum_{\text{thrsh}}^N \text{Clut}$ , where Clut is the vector containing the histogrammed clutter pixel intensities).



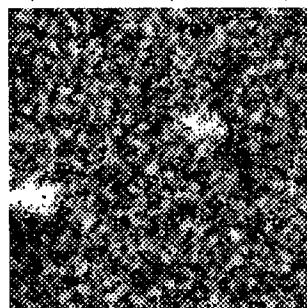
(a. Target (Close up))



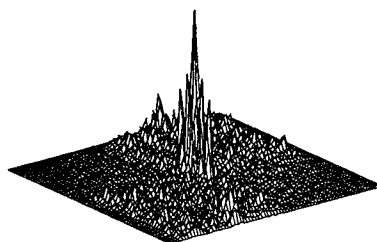
(a. 2-D Correlation)



(a. Surface plot)



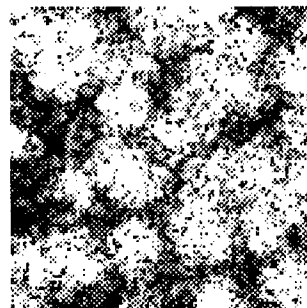
(b. Target and Tree)



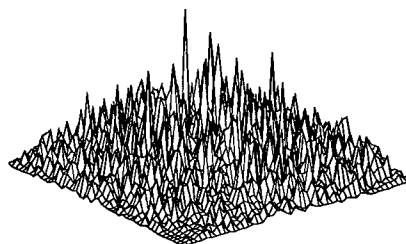
(b. 2-D Correlation)



(b. Surface Plot)



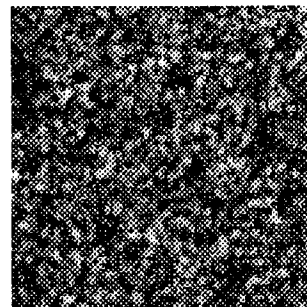
(c. Trees)



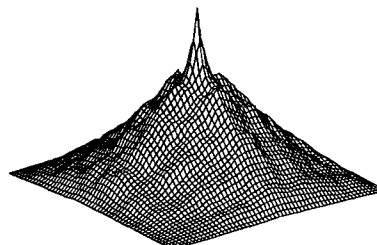
(c. 2-D Correlation)



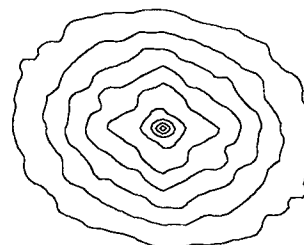
(c. Surface Plot)



(d. Ground Clutter)



(d. 2-D Correlation)



(d. Surface Plot)

Figure 28. 2-D Correlation analysis for: a) Target, b) Target plus Tree, c) Trees, and d) Ground Clutter.

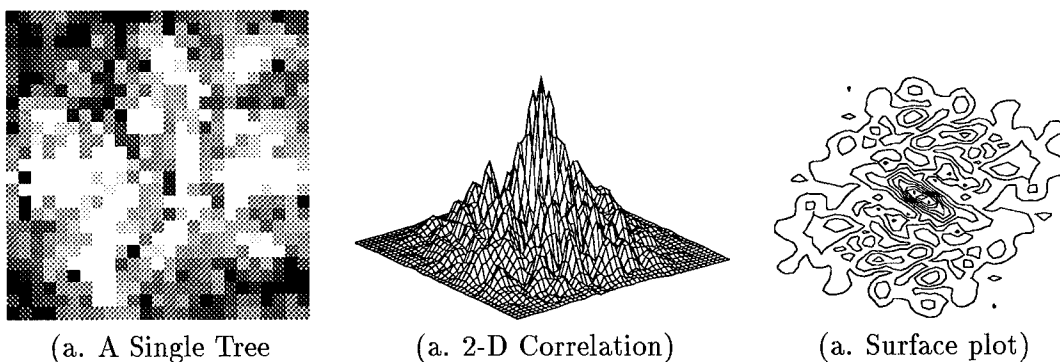


Figure 29. 2-D Correlation analysis for a single tree

Plots of ROC curves for all aspect angles and polarizations for Data Set 1 are at Figure 30. These plots show that the detectability of targets varies considerably at different aspect angles and polarizations. For example, the ROC curve of the HH image at aspect angle  $0^\circ$  is extremely good ( $P_D=0.8$  for a  $P_{fa}$  of 0.2), whereas, the ROC curve of the HV image at aspect angle  $-15^\circ$  is just above the chance line. These results reinforce the T/C results (refer Table 3) for the unprocessed images. That is, the largest T/C ratio was the HH image at an aspect angle of  $0^\circ$  and this image also provided the best ROC curve result. Similarly, the lowest T/C ratio was for the HV image at an aspect angle of  $-15^\circ$  and this image also gave the worst ROC curve result. Accordingly, the T/C metric and plots of ROC curves appear to be good metrics for assessing the improvement in target detection performance for the polarimetric and multi aspect angle algorithms. In addition, the T/C ratios and ROC results justify the requirement for a target detection system that provides the capability of multiple looks at a target scene in a single flyover. In Chapter IV, the results of detecting the combined polarimetric and WASAR images are presented. One of the methods used to quantify the improvement of the polarimetric and WASAR combining algorithms is a plot of the ROC curve of the combined (polarimetric or WASAR) image.

For comparison with the unprocessed images, the ROC curve of the HH image at aspect angle of  $+15^\circ$ , which has a typical ROC curve response, shall be used as a benchmark to show the improvement of each algorithm to the unprocessed images.

### 3.5 Clutter Models

The aim of generating clutter models with different statistical distributions is to obtain a thorough understanding of clutter phenomenology, and use the generated clutter to test target detection algorithms under different terrain conditions. As discussed previously, clutter from different terrain and grazing angles has different statistics. For example, the log-normal distribution has been found to be a good fit for sea clutter and land clutter at low grazing angles  $\leq 5^\circ$ , the Weibull clutter model is used for grazing angles between 1 and 30 degrees [20], and the Rayleigh model is used for clutter whose amplitude probability distribution encompass a limited dynamic range (i.e. bare ground surfaces, agricultural fields and dense forest canopies).

In this section Gaussian, Rayleigh and Weibull clutter models will be developed and generated. Where possible, the generated clutter will be compared to SAR clutter obtained from the XPATCH-ES program. For demonstration purposes the generated clutter will be added to clean polarimetric images (HH, HV and VV) of a T-72 tank.

*3.5.1 Clutter Model Theory.* High resolution SAR clutter can be statistically modelled by the product model [15, 12]. Using the product model, complex clutter samples are represented by the following equation

$$Y = X(I + jQ) \quad (31)$$

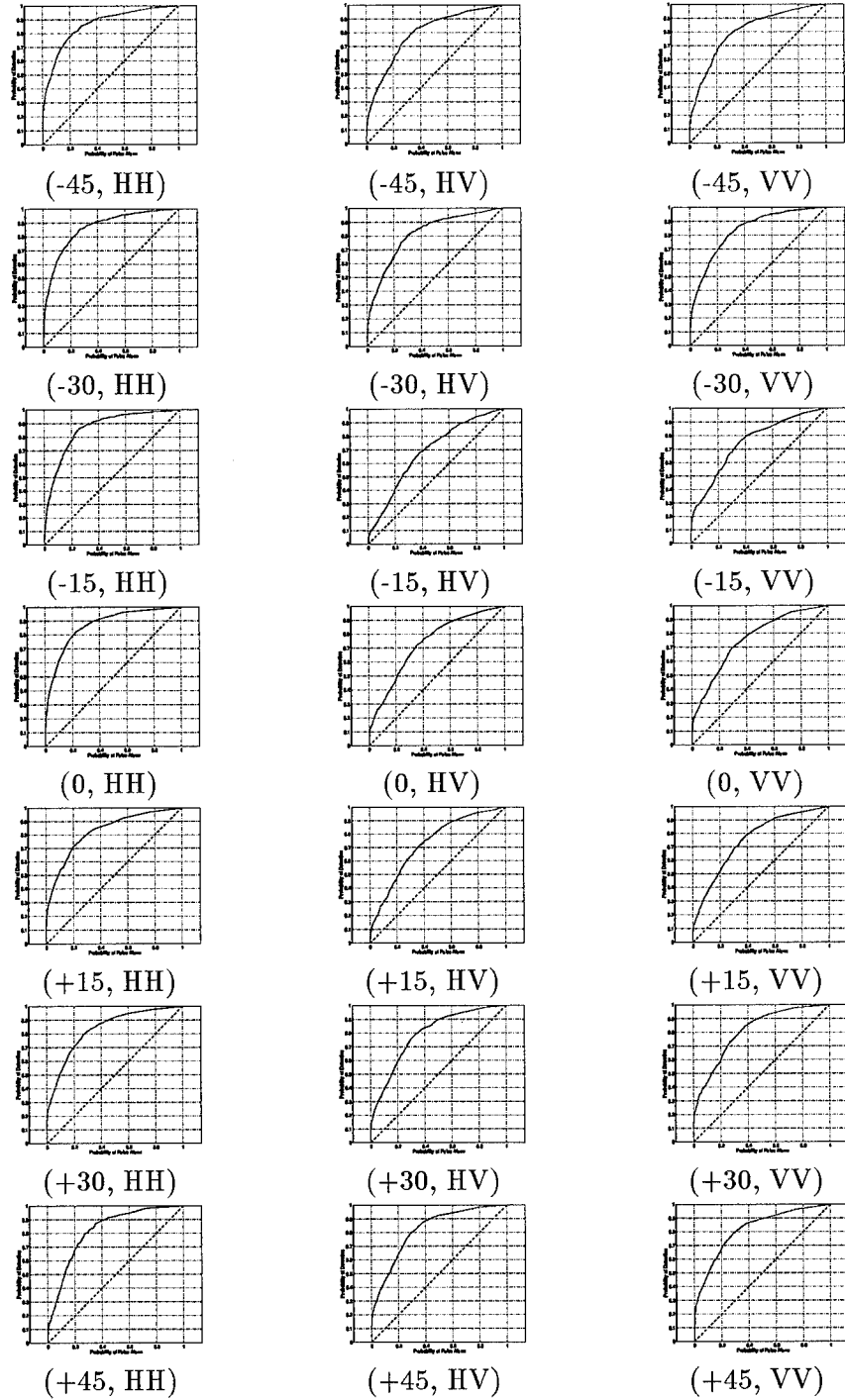


Figure 30. Plots of ROC curves for Data Set 1

where  $Y$  is the complex clutter sample,  $X$  is the texture or intensity component and  $(I + jQ)$  is the complex speckle component. The texture or intensity component  $X$ , which characterizes the distribution of the clutter is typically gamma, Weibull or log-normal distributed. The  $I + jQ$  is a zero mean complex Gaussian random variable representing the speckle component.

*3.5.1.1 Gaussian Clutter Model Theory.* A complex Gaussian clutter model is one in which the  $Y$  of Equation 31 is complex Gaussian. Fully polarimetric complex Gaussian clutter is defined as

$$Y = \begin{bmatrix} HH \\ HV \\ VV \end{bmatrix} = \begin{bmatrix} HH_i + jHH_q \\ HV_i + jHV_q \\ VV_i + jVV_q \end{bmatrix}. \quad (32)$$

The joint pdf of the complex Gaussian random variable is defined as

$$f(Y) = \frac{1}{\pi^3 |\Sigma|} \exp \left\{ -Y^\dagger \sum_Y^{-1} Y \right\} \quad (33)$$

where  $\sum_Y^{-1}$  is the polarization covariance matrix defined at Equation 29. For a Gaussian polarimetric clutter model Novak [15] has shown that the covariance matrix simplifies to the form shown in Equation 3.

*3.5.2 Gaussian Clutter Generator.* The first clutter model developed and generated is a Gaussian amplitude clutter generator. Gaussian distributed clutter was generated and added to the HH, HV and VV polarimetric images of a T-72 tank. SAR clutter is

not usually Gaussian distributed, however, a Gaussian clutter model is useful for testing different types of detectors and polarimetric algorithms.

Uncorrelated Gaussian clutter was generated by simply forming a  $512 \times 512$  matrix of zero mean gaussian random variables with variance of  $\sigma_c$ , in Matlab. Where the variance or the power of the noise is a variable selected by the operator. For demonstration purposes the noise variance was selected so as to hide the T-72 tank. A matlab function SNR.m was written (enclosed at Appendix A) that computes the average signal power of the pixel intensities of the T-72 image and determines the required noise variance for a given signal to noise ratio. For example, using just the target pixels of the T-72 HH image, and a desired signal to noise ratio of -9 dB, a noise variance of 0.0972 was computed. This noise variance value was used to generate the Gaussian noise which was then added to the T-72 polarimetric images. In Section 3.2.5 it was shown, through an analysis of the polarimetric covariance matrix, that the correlation between polarizations was small (refer Table 4). Further, for a Gaussian random process, uncorrelated random variables are independant. Accordingly, three independant Gaussian noise generators were used to generate polarimetric clutter. Figure 31 shows the three clean polarimetric images of the T-72 tank and Figure 32 shows the three polarimetric images with zero mean, 0.0972 variance, additive Gaussian noise. The Matlab code for the Gaussian clutter generator is at Appendix A (gauss-clut.m).

*3.5.3 Rayleigh Clutter Generator.* Complex Gaussian clutter has a Rayleigh amplitude probability distribution [19]. To generate complex Gaussian clutter is a simple case of combining two Gaussian random variables ( $X$  and  $Y$ ) with mean of  $\mu$  and standard



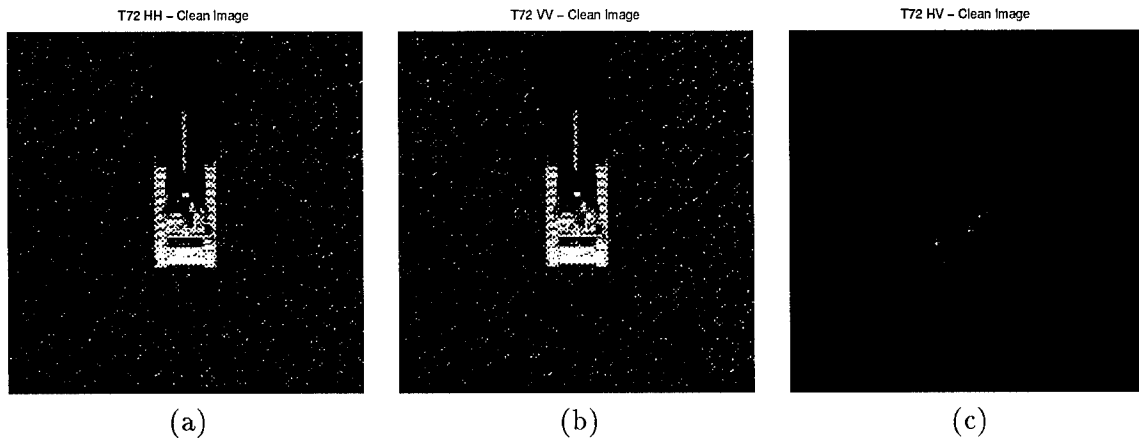


Figure 31. Clean Images of T-72 Tank (a) HH, (b) VV (c) VH

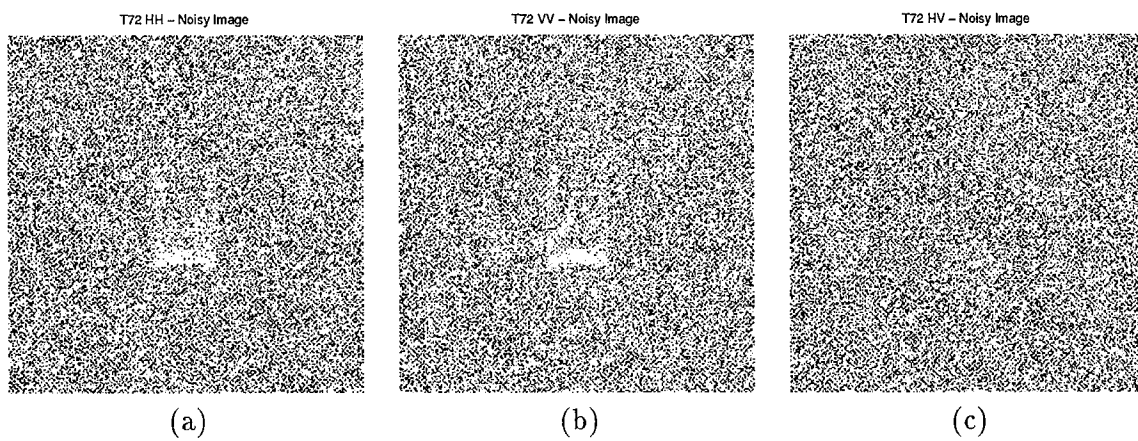


Figure 32. Noisy Images of T-72 Tank (a) HH, (b) VV (c) VH.

deviation of  $\sigma$  by the following equation

$$z = x + jy. \quad (34)$$

Thus, the amplitude of  $z$ , which is Rayleigh distributed, is

$$z = \sqrt{x^2 + y^2}. \quad (35)$$

To accurately model SAR clutter the generated clutter must be as close an approximation as possible to actual SAR clutter. To this end, generated clutter will be a good approximation of SAR clutter if it exhibits similar statistical properties as the SAR clutter. A statistical analysis of XPATCH-ES SAR clutter scenes will provide information describing the prominent statistical properties of the clutter data that can be used in the clutter generators. A simple statistical analysis involves determining the clutters' distribution and estimates of its various moments, such as the sample mean, sample standard deviation and the polarimetric covariance matrix. To summarize, a clutter model will be a good fit for SAR clutter if the model parameters, such as the distribution, mean and variance are set to those values obtained from a statistical analysis of actual SAR clutter scenes.

*3.5.3.1 Statistical Analysis of XPATCH-ES Clutter.* Data file "gs-f1000-000-d45rh", obtained from XPATCH-ES, consists purely of simple ground clutter (i.e. no targets or changes in terrain) . The image of this clutter scene is shown in Figure 34(a). A statistical analysis of this data was performed to obtain the clutters distribution, mean, standard deviation and covariance matrix. First, the distribution of the clutter scene was established. This was done by the same method outlined in Section 2.7. Figure 33 shows

a histogram plot of the pixel intensities with an overlaid plot of a Rayleigh pdf. As can be seen from Figure 33(a) the pixels are approximately Rayleigh distributed. Accordingly, this XPATCH-ES clutter scene can be used as benchmark for the Rayleigh clutter generator.

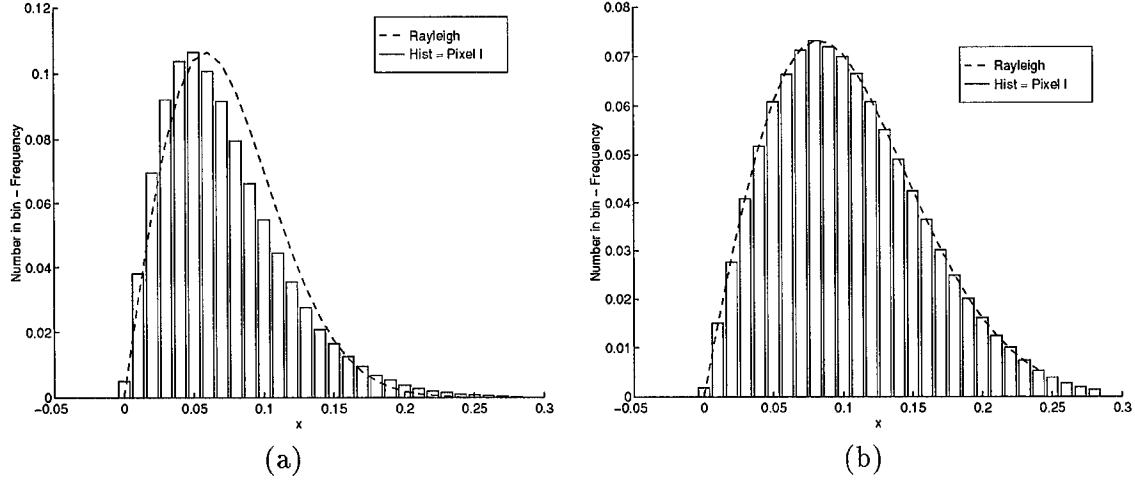


Figure 33. Histograms of pixel intensities for: (a) XPATCH-ES Clutter, and (b) Generated Clutter.

The sample mean and standard deviation of the XPATCH-ES clutter pixel intensities were calculated to be  $\mu=8.1284 \times 10^{-4}$  and  $\sigma = 0.0833$  respectively. The polarimetric covariance matrix of the clutter was computed to be

$$\Sigma_{polarXPATCH-ESClut} = 0.069 \begin{bmatrix} 1.00 + j0.00 & 0.0341 - j0.0867 & 0.2468 - j0.1821 \\ 0.0341 + j0.0867 & 0.2790 + j0.00 & 0.0271 + j0.0128 \\ 0.2468 + j0.1821 & 0.0271 - j0.0128 & .7464 + j0.00 \end{bmatrix}.$$

The correlation between the HH and HV returns and the other polarizations combinations for the XPATCH-ES clutter were computed using Equation 30 and the results are listed in Table 10. Rayleigh clutter was formed by creating two 512 x 512 matrices of Gaussian distributed zero mean 0.069 variance random variables in Matlab, and combin-

Table 10. Correlation coefficients between polarizations XPATCH-ES Clutter

$\rho_{hh-hv}$	$\rho_{hh-vv}$	$\rho_{hv-vv}$
0.1763	0.3551	0.0656

ing them according to Equation 35. The Matlab code of the Rayleigh clutter generator is at Appendix A (rayl-clutt.m). Figure 34 shows images of the generated Rayleigh distributed clutter and the XPATCH-ES clutter. A comparison of the two images shows that the XPATCH-ES image has more pixel intensity variation than the “smoother” generated clutter image. The main difference between the two images is that the XPATCH-ES clutter is more correlated than the uncorrelated generated clutter. The pixel to pixel correlation coefficient was computed to determine the amount of spatial correlation that exists with the ground clutter. The sample correlation coefficient quantifies the correlation or relationship between two random variables. Mathematically it is defined as

$$\rho_{xy} = \frac{\sum_{i=1}^n (X_i - \mu_x)(Y_i - \mu_y)}{\sqrt{\sum_{i=1}^n (X_i - \mu_x)^2 \sum_{i=1}^n (Y_i - \mu_y)^2}} \quad (36)$$

where  $(X_1, Y_1, \dots, X_n, Y_n)$  are the  $n$  pairs of observations, and  $\mu_x$  and  $\mu_y$  are the means of the two data sets. To calculate the correlation between neighboring pixels a Matlab function (pix-corr.m enclosed at Appendix A) was written that calculates the correlation coefficients between pixels for different sized windows within an image. For example, a 10 x 10 area within an image could be analysed to determine how correlated a pixel is with its immediate neighbours. Within the window under investigation  $\rho_{0,1}$  is the correlation coefficient of a pixel and its immediate right neighbour,  $\rho_{1,0}$  is the correlation coefficient of a pixel and the pixel directly below it, and  $\rho_{1,1}$  is the correlation coefficient of a pixel and the pixel down one and across to its right (diagonal element). A 10 x 10 window produces

a 5 x 5 matrix of correlation coefficients. A typical result using a 10 x 10 window from the data file “gsf1000d45rhh” SAR image is

$$\begin{bmatrix} \rho_{0,0} & \rho_{0,1} & . & . & \rho_{0,5} \\ \rho_{1,0} & \rho_{1,1} & . & . & \rho_{1,5} \\ . & . & . & . & . \\ . & . & . & . & . \\ \rho_{5,0} & . & . & . & \rho_{5,5} \end{bmatrix} = \begin{bmatrix} 1.000 & 0.5227 & 0.0719 & -0.0235 & -0.0463 \\ 0.5295 & 0.3115 & 0.0609 & -0.0324 & -0.0907 \\ 0.1397 & 0.1168 & 0.0187 & -0.0752 & -0.0950 \\ 0.0729 & 0.0732 & -0.0138 & -0.0448 & -0.0018 \\ 0.0811 & 0.0746 & -0.0300 & -0.0274 & 0.0176 \end{bmatrix} .$$

Using a 20 x 20 window the pixel to pixel correlation was recalculated and the correlation coefficients for the left-right, up-down, and diagonal are displayed graphically for the SAR image at Figure 34(a) and for the generated clutter at Figure 34(c). Comparing theses two plots the SAR image is more correlated (pixel to pixel) than the generated clutter scene. Different sized windows were taken from different areas within each of the clutter scene yielding similar result. The generated clutter can be correlated by using a two dimensional filter. The correlation function of the clutter is controlled by the transfer function of the filter. A simple schematic of a one-dimensional filter is shown in Figure 35.

In Figure 35, the input  $x(t)$  is related to the output  $y(t)$  according to the following equation:

$$y(t) = \int_{-\infty}^{\infty} h(t)x(t-\tau)d\tau \quad (37)$$

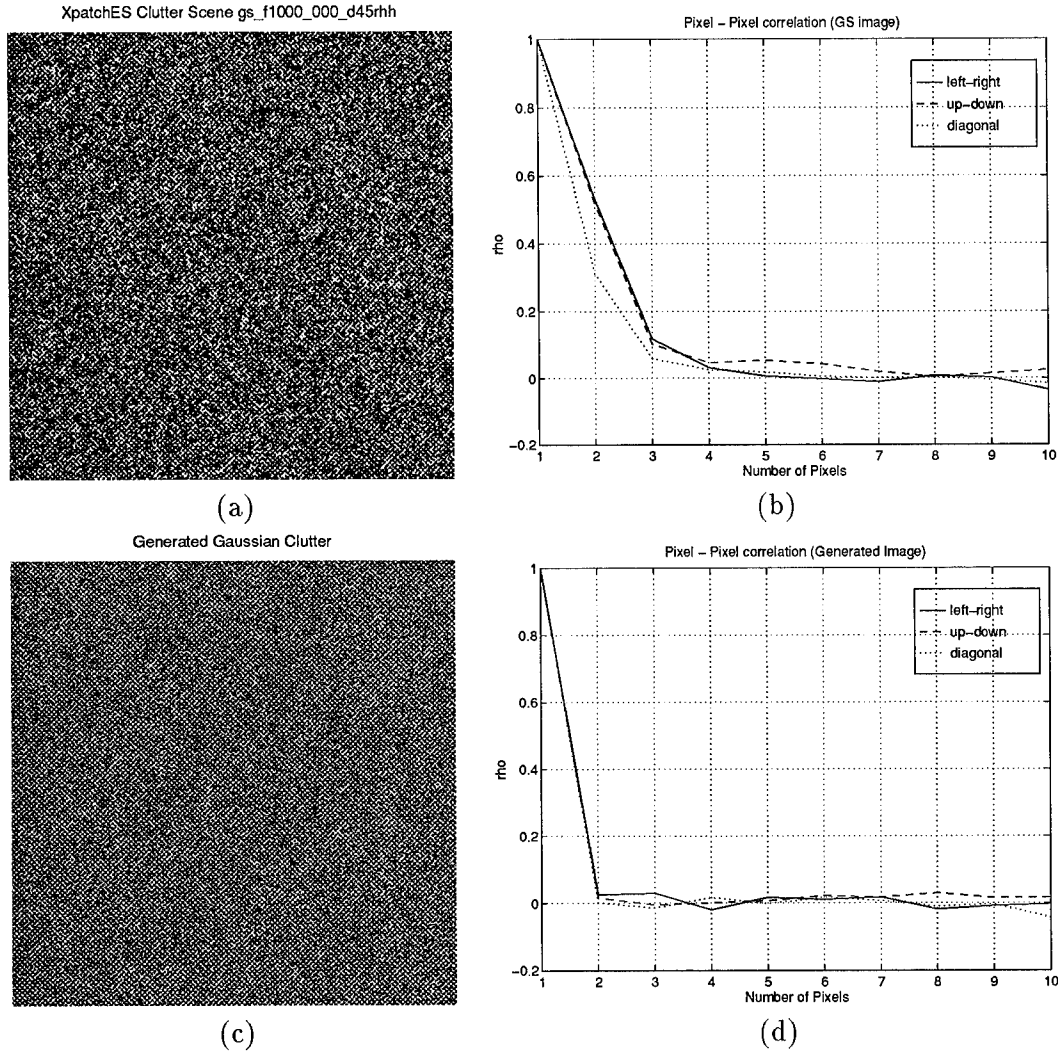


Figure 34. Images and Correlation Plots: (a) XPATCH-ES clutter scene (b) Pixel to Pixel correlation, (c) Generated clutter scene , and (d) Pixel to Pixel correlation.

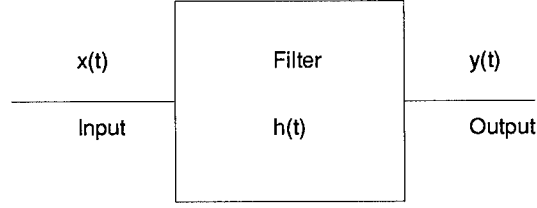


Figure 35. Simple Schematic of a Filter

where  $h(t)$  is the impulse response of the filter. The autocorrelation of  $x(t)$  is

$$R_{xx}(\tau) = E[x(t)x(t - \tau)]. \quad (38)$$

The autocorrelation of  $y(t)$  is

$$\begin{aligned} R_{yy}(\tau) &= E[y(t)y(t - \lambda)] \\ &= E \left[ \int_{-\infty}^{\infty} h(t)x(t - \tau)d\tau \int_{-\infty}^{\infty} h(t - \lambda)x(t - \tau - \lambda)d\tau \right] \\ &= E \left[ R_{xx}(\lambda) \int_{-\infty}^{\infty} h(t)d\tau \int_{-\infty}^{\infty} h(t - \lambda)d\tau \right]. \end{aligned} \quad (39)$$

Accordingly, the impulse response of the filter determines how correlated the clutter is. For a 2-D case a 2-D filter is used and as in the one dimensional example the impulse response of the filter determines the spatial correlation of the clutter.

**3.5.4 Weibull Clutter Generator.** The Weibull clutter generator is based on the transformation of a random variable with uniform distribution to a random variable with a Weibull distribution. The transformation is defined as [19]

$$w = F_w^{-1}(u) \quad (40)$$

where  $w$  is the required random variable,  $F_w^{-1}$  is the inverse cumulative distribution function of  $w$  (Weibull for this example) and  $u$  is a random variable with uniform distribution. Using the transformation defined at Equation 40, clutter or noise of any distribution can be formed providing the inverse cumulative distribution function of the required clutter exists. The Weibull cumulative distribution function is defined as

$$F(w) = 1 - \exp\left\{-\left(\frac{w}{\nu}\right)^\eta\right\} \quad (41)$$

where  $\eta$  and  $\nu$  are shape parameters. Applying the transformation (Equation 40) yields

$$w_i = \eta[-\ln(u_i)]^{\frac{1}{\nu}}. \quad (42)$$

Thus, uncorrelated Weibull clutter, with shape parameters  $\eta$  and  $\nu$ , can be generated by forming a matrix of random variables with uniform distribution and applying it to Equation 42. Using this technique Weibull clutter was generated. Figure 36 shows an image of the Weibull distributed clutter and a histogram of the pixel intensities. The Matlab code for the Weibull clutter generator is at Appendix A.

### 3.6 Summary

In this chapter an analysis of the XPATCH-ES data was performed. In addition, Gaussian, Rayleigh and Weibull clutter models were developed and generated. Generated clutter of different distributions is useful for testing and digitally simulating target detection systems in different types of terrain.



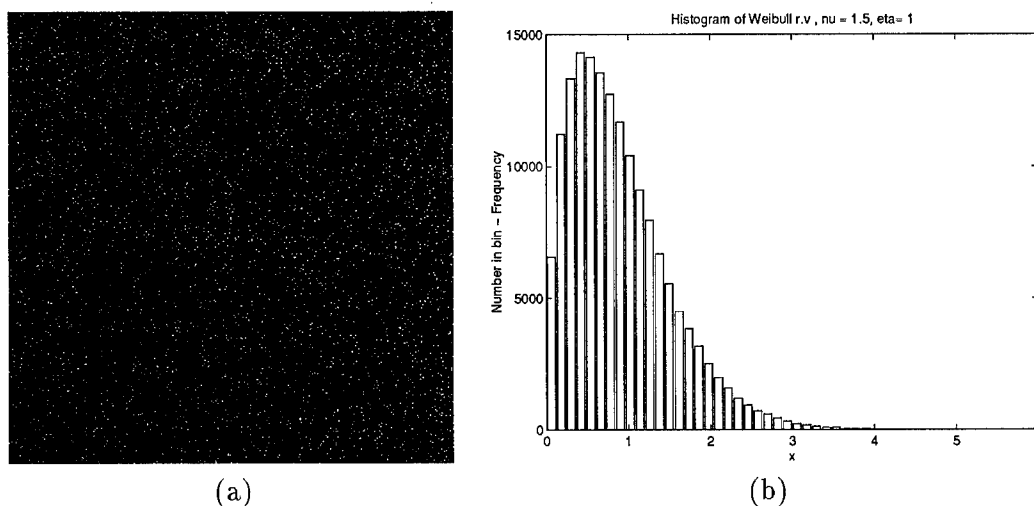


Figure 36. a) Image of Generated Weibull clutter, and b) Histogram of Pixels

The data analysis involved a statistical analysis and a feature extraction. From this analysis it was shown that the standard deviation is significantly larger for targets than clutter, and combined with the 2-Dimensional correlation coefficient are *good* features for discriminating targets and clutter false alarms. Polarimetric and wide angle covariance matrices (PCMs and WACMs) were formed and analyzed. Polarimetric covariance parameters of man made targets were shown to be different to those of clutter. Both covariance matrices have a definite structure. For the PCMs all the off diagonal elements are approximately zero, and the WACM for clutter was shown to be a diagonal matrix with uniform diagonal elements. Whereas for targets the main diagonal elements vary. An analysis of the WACM proved the assumption that trees and ground clutter are angle invariant, whereas targets 'look' different at even small changes in aspect angle. The covariance matrices developed and formed in this chapter shall be used with the polarimetric and WASAR algorithms derived in Chapter II. These results are presented in Chapter IV .

#### *IV. Results*

In this chapter the target detection capabilities of the polarimetric and wide angle algorithms are quantified. First, a polarimetric analysis is performed on four different polarimetric data sets. Polarimetric images are formed using the Average, Span, POW, PMF and PWF algorithms. The speckle and the target detection capabilities of each of these polarimetrically combined images shall be assessed and quantified using T/C ratios, S/M ratios, ROC curves, discriminator performance and plots of target and clutter pdfs. Then, a multi aspect angle analysis is performed on three multi aspect angle data sets. The wide angle images will be formed using the WASAR average, WWF and AWWF (for various sized pixel window) algorithms. The target detection performance of these algorithms shall be assessed using the same metrics listed above. A comparison between polarimetric and WASAR processing is performed with the aim of determining the best type of processing for target detection. Finally, images are generated by a combination of polarimetric and wide angle techniques. The resulting images shall be analyzed with respect to target detection performance.

##### *4.1 Polarimetric Processing*

This section provides the results of polarimetrically combining the HH, HV and VV images. The three polarimetric images were combined to produce a single image of a target scene. The polarimetric images were combined by five different algorithms: 1) Average, 2) Span, 3) POW, 4) PMF and 5) PWF. These algorithms are compared with respect to the T/C ratio, S/M metrics, plots of target and clutter pdfs, ROC curves and discriminator performance.

The S/M ratio is a metric that quantifies the picture quality. It measures the amount of speckle in an image. A low S/M ratio indicates a minimum speckle image. The T/C ratio indicates an improvement in target detection. A high T/C ratio is desirable. As discussed in Chapter II, the detection of targets embedded in clutter is a two class detection problem. The probability of detection is increased and the probability of false alarm is reduced if the distance between the means of the pdfs of the two classes (targets and clutter) is increased while keeping constant variance. Accordingly, the plots of the pdfs of the targets and clutter give a good indication of the target detection performance of the different polarimetric algorithms. If the polarimetric algorithm separates the target and clutter pdfs then it is theorized that this algorithm has improved target detectability. For ROC curves, a resultant high  $P_D$  with a low  $P_{fa}$ , the better is the polarimetric algorithm. Finally, for the discriminator, a good polarimetric algorithm is one that separates targets and clutter in feature space. The further the two classes are separated in feature space are the better the algorithm.

The PWF can be formed by either a direct estimation of the polarimetric covariance matrix and by combining the images via  $y = X^\dagger \Sigma_X^{-1} X$  or by using Equation 15 derived by Novak [15]. Better results were achieved using the direct estimation of the polarimetric covariance matrix method. Accordingly, the PCM and the WACM used for each data set shall be presented. The PWF algorithm produces an intensity image (i.e.  $y = X^\dagger \Sigma_X^{-1} X$ ). Therefore, all images that are not intensity images (such as the PMF and the unprocessed HH, HV and VV images) shall be converted to intensity images so that the effects of each algorithm can be effectively compared. For example, the  $HH$  image must be multiplied by  $HH^*$  to produce the  $|HH|^2$  which is an intensity image.

Four different data sets will be used to determine the performance improvements of polarimetrically combining the HH, HV and VV images. The first data set consists of just ground clutter with no targets (/xpatches/gsrotat [m30hh,m30hv,m30vv]). This data set is a polarimetric WASAR data set. That is, it contains HH, HV and VV images at aspect angles of  $-30^\circ$ ,  $0^\circ$  and  $30^\circ$ . It will also be used in the wide angle processing analysis. The second data set is a segment of the WASAR data set (Data Set 1 - HH, HV, and VV at an aspect angle of  $-15^\circ$ ) that contains only one target in ground clutter. Figure 37 shows images of the first two data sets. The third data set is the HH, HV and VV images at  $-30^\circ$  aspect angle of Data Set 1 (WASAR). The ground scene and polarimetric images of this data set are at Figures 11 and 13 respectively. The fourth data set consists of a more complex target scene containing twelve targets, corner reflectors, roads, fences, trees and ground clutter. The ground scene and polarimetric images (HH, HV and VV) of this more complex target scene are at Figure 38. The purpose of using different data sets with increasing levels of complexity, is to test the polarimetric algorithms under varying conditions. Further, stepping from a simple scene, to a scene containing one target at one orientation, to more complex scenes with multiple targets at various orientations, the number of variables is controlled and the effects of each algorithm can be assessed under the changing conditions.

*4.1.1 Polarimetric Data Set 1.* The first data set, although containing no targets, is analyzed to show the effect of each polarimetric algorithm on simple ground clutter. The polarimetric images of Data Set 1 were combined using the Average, Span, POW and the PWF. (The PMF was not used as there are no targets in the image.). The equations

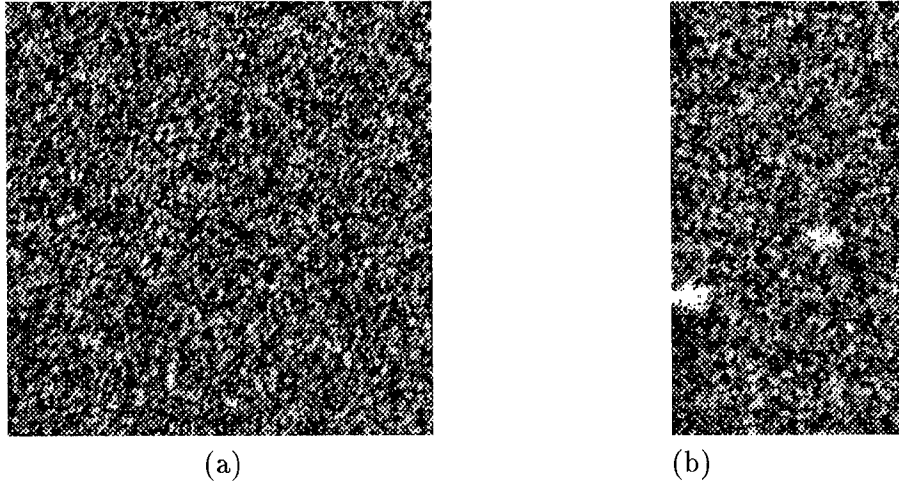


Figure 37. Images of: (a) Polarimetric Data Set 1, and (b) Polarimetric Data Set 2

for these algorithms are at Section 2.3 and the Matlab code for each algorithm is at Appendix A. The polarimetric covariance matrix for this data set is

$$\Sigma_{X-polarDS1} = 0.0064 \begin{bmatrix} 1.00 + j0.00 & 0.0358 - j0.0839 & 0.2357 - j0.1846 \\ 0.0358 + j0.0839 & 0.3010 + j0.00 & 0.0273 + j0.0101 \\ 0.2357 + j0.1846 & 0.0273 - j0.0101 & 0.7854 + j0.00 \end{bmatrix}.$$

The form of the PCM is in line with the polarimetric clutter matrices analyzed in Chapter III.

As the data set contains no targets, the only metrics that can be used to compare the polarimetric algorithms are the S/M ratio and the effect that each algorithm has on the clutter pdf. Table 11 shows the S/M ratios for each algorithm and Figure 39 shows plots of the clutter pdfs. Direct plots of the normalized histogrammed pixel intensities are used in this chapter rather than parametric estimates of the densities. This was done to show more accurately the effects of the processing.

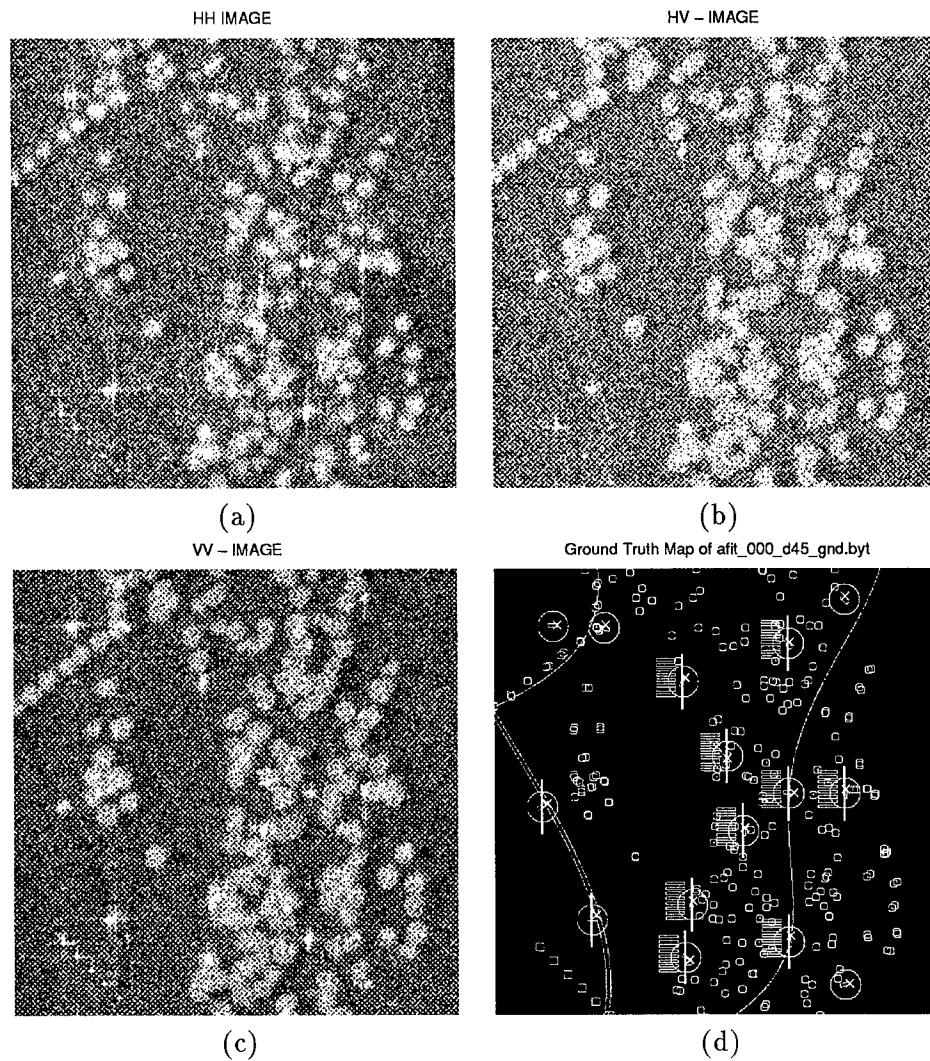


Figure 38. Polarimetric Images Polarimetric Data Set 4 (AFITF1000D45 data set): (a) HH, (b) HV, (c) VV, and (d) Ground truth map.

Table 11. S/M ratios for polarimetric Data Set 1

$ HH ^2$	$ HV ^2$	$ VV ^2$	Average	Span	POW	PWF
1.2667	1.0365	1.0652	0.8345	0.7731	0.7247	0.7267

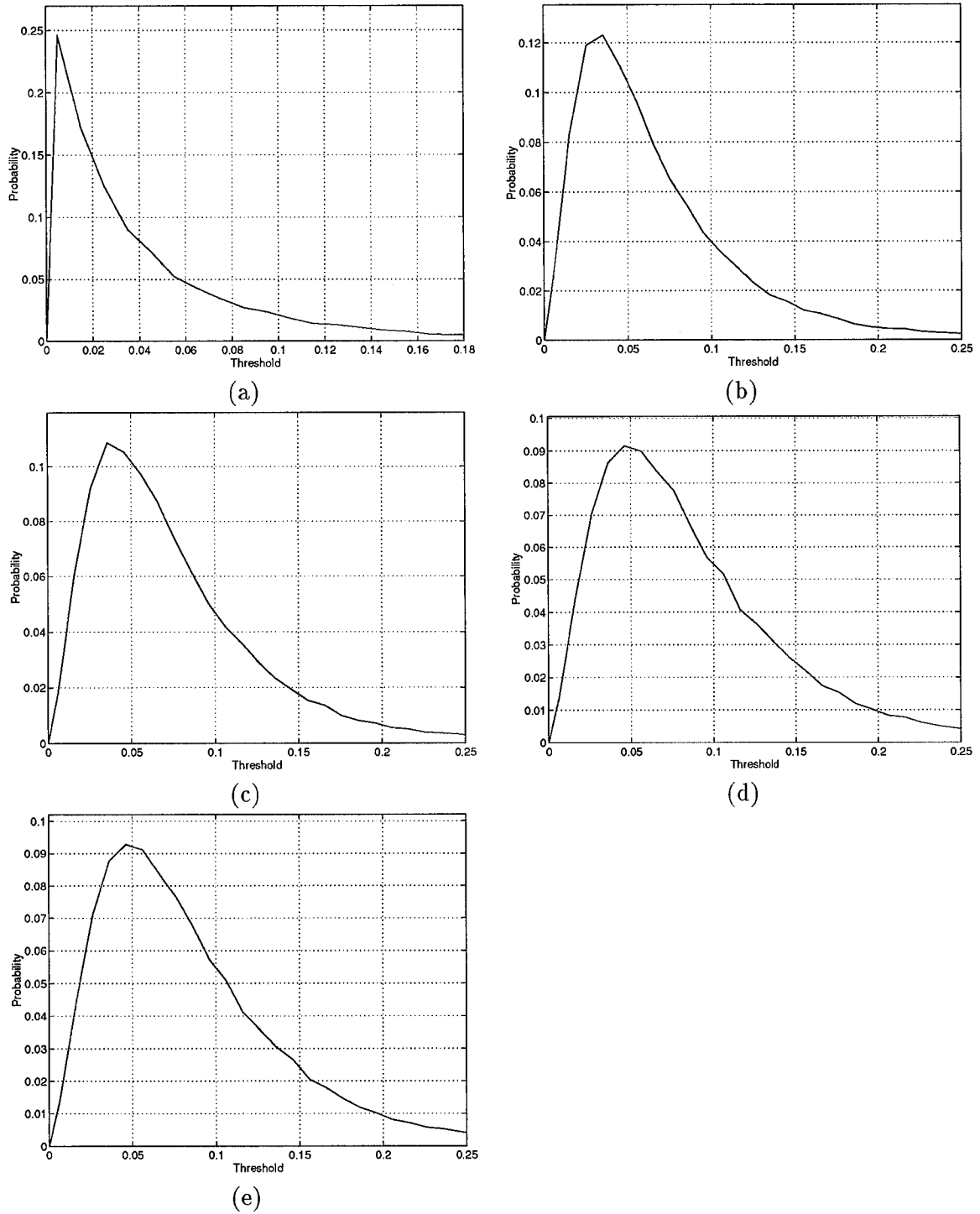


Figure 39. Clutter Pdfs of Polarimetric Data Set 1: (a)  $|HH|^2$ , (b) Average, (c) Span, (d) POW, and (e) PWF.

Referring to Table 11, the PWF and the POW algorithms produced the minimum speckle intensity images. This was expected as both of these algorithms were derived to reduce speckle by a Lagrange minimization of the S/M ratio. From Figure 39 it can be seen that all of the polarimetric algorithms actually spread the clutter pdfs. This is an undesirable effect for target detection purposes as the closer the target and clutter pdfs are the greater is the probability of clutter false alarms. Notwithstanding, a similar spread on the target pdf could increase the probability of detection.

*4.1.2 Polarimetric Data Set 2.* The polarimetric images of Data Set 2 were combined using the Average, Span, POW, PMF and the PWF algorithms. For this data set S/M and T/C ratios were computed; target and clutter pdfs (direct normalized histograms) were formed and plotted, and ROC curves were computed and plotted.

The polarimetric covariance matrix for this data set is

$$\Sigma_{X-polarDS2} = 0.0102 \begin{bmatrix} 1.00 + j0.00 & 0.0199 - j0.0834 & 0.3802 - j0.0135 \\ 0.0199 + j0.0834 & 0.2458 + j0.00 & -0.0622 + j0.0381 \\ 0.3802 + j0.0135 & -0.0622 - j0.0381 & 1.1733 + j0.00 \end{bmatrix}.$$

Comparing the two covariance matrices of polarimetric Data Sets 1 and 2, the  $E\{|HH|^2\}$  for Data Set 2 is larger than that of Data Set 1 due to the target. The other observation is that the VV return is stronger than the HH return ( $E\{|VV|^2\} = 1.17E\{|HH|^2\}$ ). This is also a result caused by the target which provides a stronger return in the VV polarization than in the HH polarization.



Table 12. S/M and T/C ratios for Polarimetric Data Set 2

	$ HH ^2$	$ HV ^2$	$ VV ^2$	Average	Span	POW	PMF	PWF
S/M Ratios	7.68	5.23	16.14	10.80	10.11	8.47	15.33	7.58
T/C Ratios (dB)	18.58	15.74	22.36	20.21	19.85	18.97	21.86	19.34

Table 12 lists the S/M ratios and the T/C ratios for Data Set 2. In comparison to the S/M ratios of Data Set 1 (Table 11), the S/M ratios for this second data set are significantly higher due to the presence of the target. Further, there is more range in the values of the S/M ratios for the unprocessed images (i.e.  $|HV|^2=5.2324$ ,  $|VV|^2=16.1430$ ). However, when comparing the polarimetric methods of combining the three images, the PWF has the lowest S/M ratio, indicating a minimum speckle image was formed. The T/C ratios indicate that the VV image with no processing, provides the best target detection performance using this metric. This strong VV return is evident in the polarimetric covariance matrix. The polarimetric matched filter which was derived by maximizing the T/C metric also provides good target detection performance. However, as previously stated, the problem with this algorithm is that it uses *a priori* knowledge of the target's location to form the target covariance matrix. The average and the span algorithms, which are the simplest methods of combining the polarimetric images, have better target detection performance (using this metric and excluding the PMF algorithm) than the other polarimetric algorithms. Figure 40 shows plots of target and clutter normalized histograms. These plots are not the true pdfs of the target and clutter, they are direct plots of the clutter and pixel histograms where the bin size for each is different. This was done so that the effect of each algorithm on the target histograms (which contain a smaller number of pixels with a larger variance) could be seen. Referring to Figure 40, the most obvious difference between the plots of the target and clutter histograms is that the variance of the target histograms is

significantly larger than that of the clutter histograms. This discriminating characteristic was discussed in detail in Chapter III. Referring to Figure 40(e), the PMF algorithm has effectively reduced the clutter variance compared to the other polarimetric algorithms.

Figure 41 shows plots of ROC curves for each polarimetric algorithm. As expected, for such an easily detectable target, all the ROC curves show high probability of detection with very small probabilities of clutter false alarms. The best result using this metric is the polarimetric average (Figure 41(b)) which shows a  $P_D=0.9$  for a  $P_{fa}=0.1$ .

The final test of the target detection performance of each polarimetric algorithm is the discriminator. For this data set, each image (formed by the different polarimetric algorithms) was detected using a constant threshold and then applied to the discriminator. The threshold level was set at the mean of the pixel intensities plus one standard deviation ( $\mu + \sigma$ ). The 2-D correlation coefficient and the standard deviation feature pair were used in the discriminator, and a target template of 16 x 10 pixels was used. Figure 42 shows the results of testing each algorithm in the discriminator. For all algorithms the target and clutter have been clearly separated. The PMF mapped the target, tree and ground clutter into tight clusters within their respective areas in feature space. All of the polarimetric algorithms reduced the number of clutter false alarms compared to the unprocessed image.

In summary, for this simple single target data set the following observations are made. The PWF algorithm produced the minimum speckle (lowest S/M ratio) image of all of the polarimetric combining algorithms. It was noted through an analysis of the PCM that the VV return for this data set was higher than either the HH or HV returns. This was due to the target and the T/C ratios confirmed this (i.e.  $|VV|^2$  T/C ratio approximately 4 dB

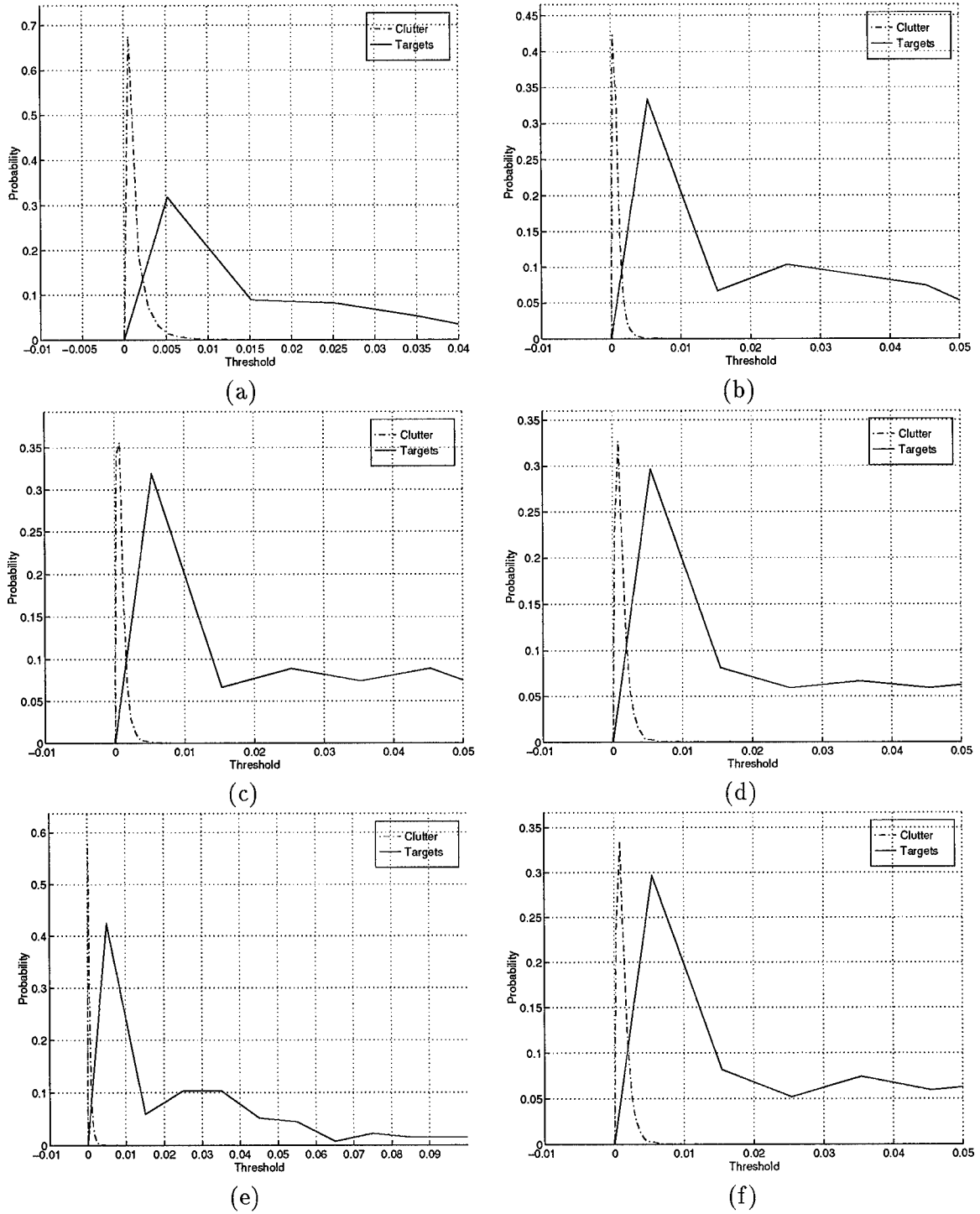


Figure 40. Target and Clutter Pdfs of Data Set 2: (a)  $|HH|^2$ , (b) Average, (c) Span, (d) POW, (e) PMF, and (f) PWF.

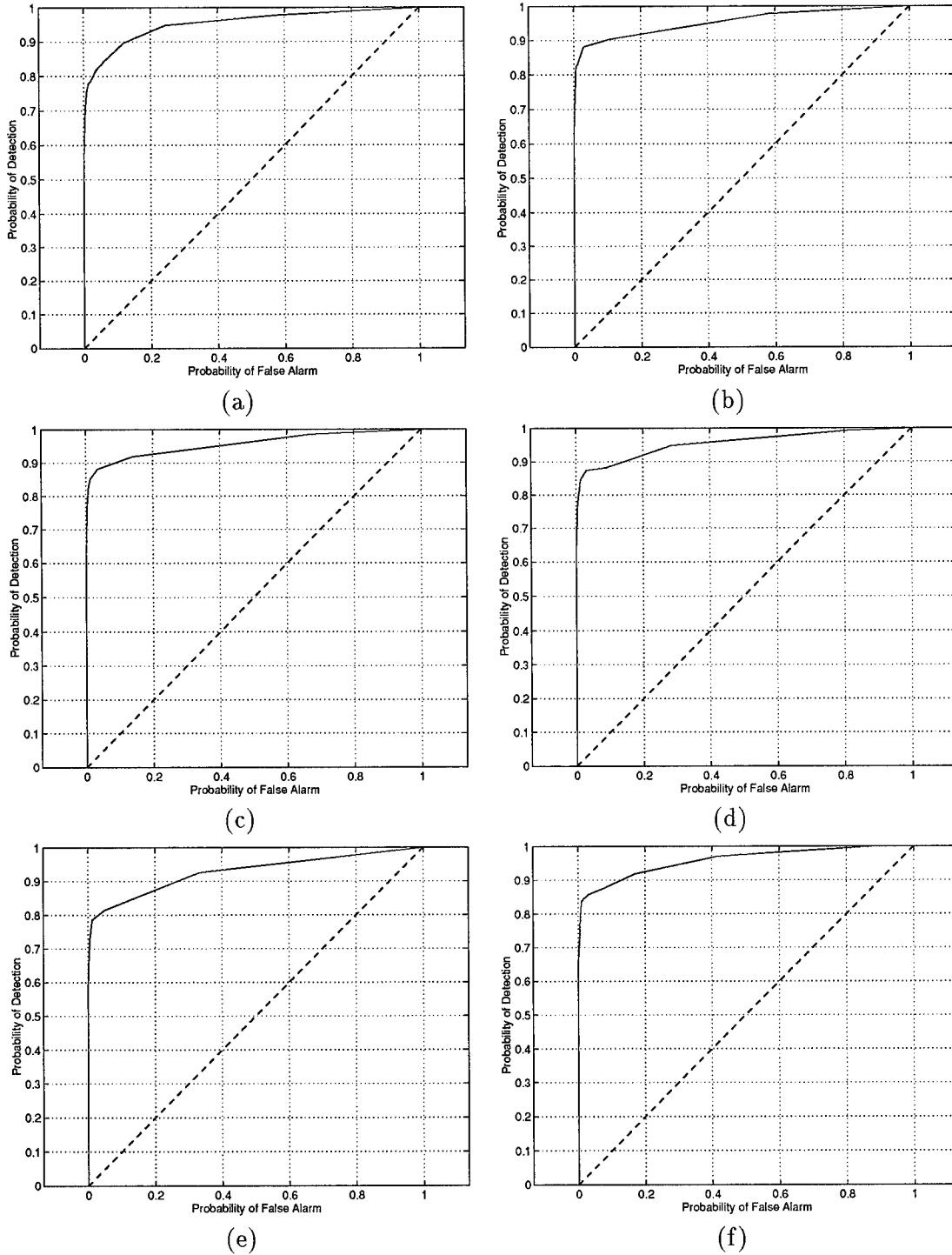


Figure 41. ROC curves for Polarimetric Data Set 2: (a)  $|HH|^2$  (b) Average, (c) Span, (d) POW, (e) PMF, and (f) PWF.

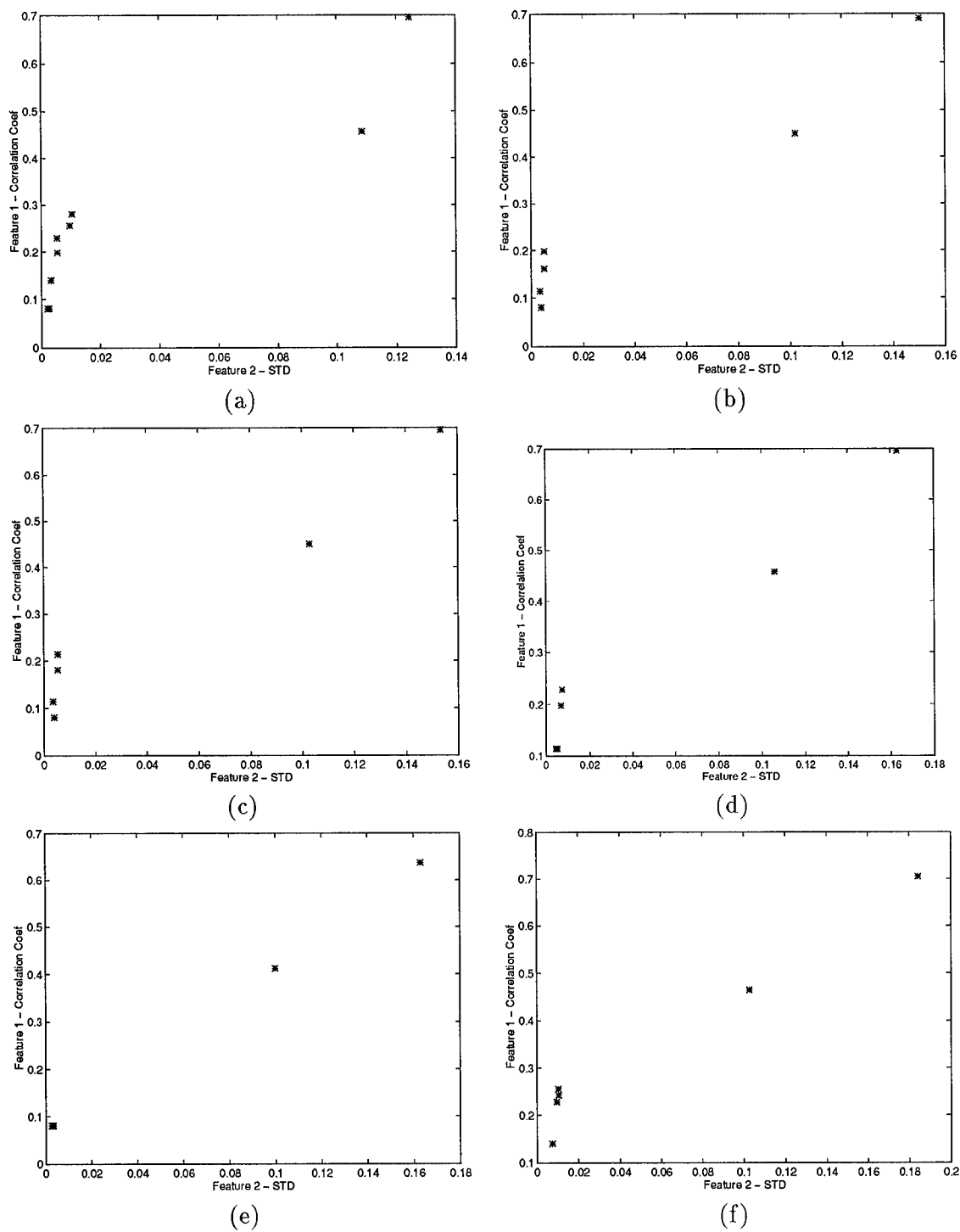


Figure 42. Discriminator Results for Polarimetric Data Set 2: (a)  $|HH|^2$  (b) Average, (c) Span, (d) POW, (e) PMF, and (f) PWF.

larger than the  $|HH|^2$  T/C ratio). Plots of the clutter and target histograms, ROC curves and discriminator results for all algorithms were, as expected, extremely good.

*4.1.3 Polarimetric Data Set 3.* This data set is the first complete and more complex target scene. It contains five targets at various rotations, and two different types of clutter terrain (trees and ground clutter).

The polarimetric covariance matrix for this data set is

$$\Sigma_{X-polarDS3} = 0.0374 \begin{bmatrix} 1.00 + j0.00 & 0.0055 + j0.0847 & 0.0160 + j0.1099 \\ 0.0055 - j0.0847 & 0.3623 + j0.00 & 0.0229 + j0.0120 \\ 0.0160 - j0.1099 & 0.0229 - j0.0120 & 0.8756 + j0.00 \end{bmatrix}.$$

Once again the form of the PCM is in line with previous results. The combined polarimetric images using the average, span, POW, PMF and the PWF polarimetric algorithms, for both data sets, are shown in Figure 43. The HH image for both data sets has been included for comparison purposes so that the visual effects of the different polarimetric techniques can be observed. Referring to Figure 43, the PWF image is the clearest and most defined image. That is, the trees and targets look brighter (whitened) and more defined than in any of the other polarimetric images. This is because the PWF algorithm was derived by minimizing the S/M ratio to produce an intensity image having a minimum amount of speckle.

The S/M and T/C ratios were calculated for each algorithm and the results are listed in Table 13. As expected the PWF and the POW images have the lowestest S/M ratios (minimum speckle image). The T/C ratios of all the algorithms are relatively close,

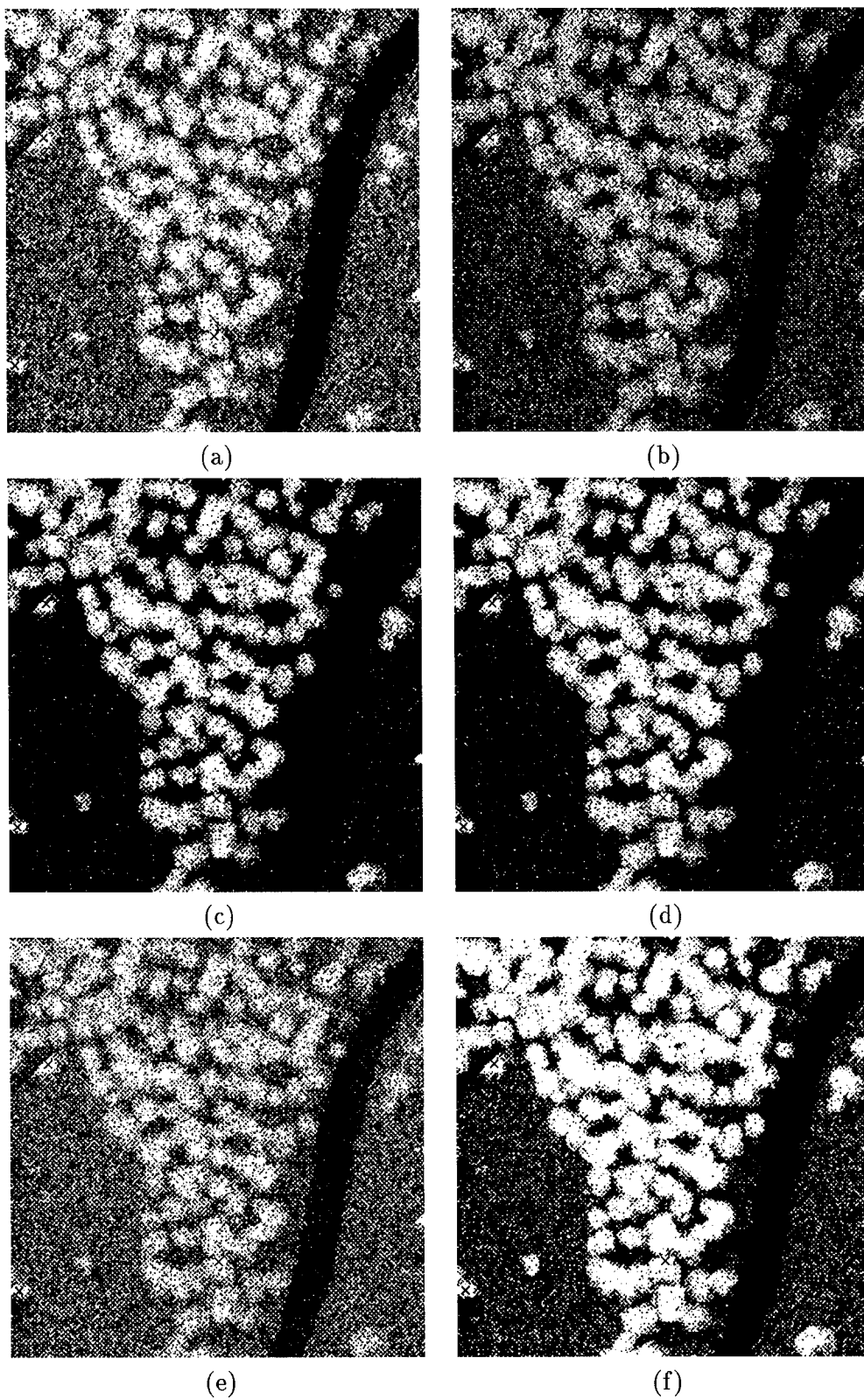


Figure 43. Combined Polarimetric Images of Data Set 3 using the: (a)  $|HH|^2$  (b) Average, (c) Span, (d) POW, (e) PMF, and (f) PWF.

Table 13. S/M and T/C ratios Polarimetric Data Set 3

	HH	HV	VV	Average	Span	POW	PMF	PWF
S/M Ratio	2.86	2.76	3.06	2.41	2.34	2.33	2.66	2.32
T/C Ratio (dB)	10.35	9.97	11.04	10.58	10.50	10.47	10.87	10.49

however, they are on average 0.5 dB lower than the maximum unprocessed T/C ratio (VV).

Figure 44 shows plots of clutter and target normalized histograms. The structure of the clutter histogram in this data set is different than the clutter histograms seen in the previous two data sets. That is, it consists of a high narrow peak at low threshold values, corresponding to the ground clutter, and a longer tail corresponding to the trees at higher threshold levels. The tail, with its higher valued pixel intensities (trees) is the main cause of clutter false alarms. Referring to Figure 44, the target and clutter normalized histograms for all of the polarimetric algorithms have not been significantly separated. The T/C values reinforce this observation.

Plots of ROC curves for each algorithm are at Figure 45. As was the case for the T/C ratios there is not a large noticeable difference in target detectability between the different algorithms.

The results of testing each polarimetrically combined image in the discriminator are shown at Figure 46. These results show that the PWF, POW and the Span algorithms have effectively separated targets from clutter false alarms. The clutter false alarms are more tightly clustered (in feature space) so that a threshold level of 0.05 (standard deviation) would effectively eliminate the majority of clutter false alarms. Hence, although the PWFs' target detection performance was below that of the average and PMF algorithms, it appears



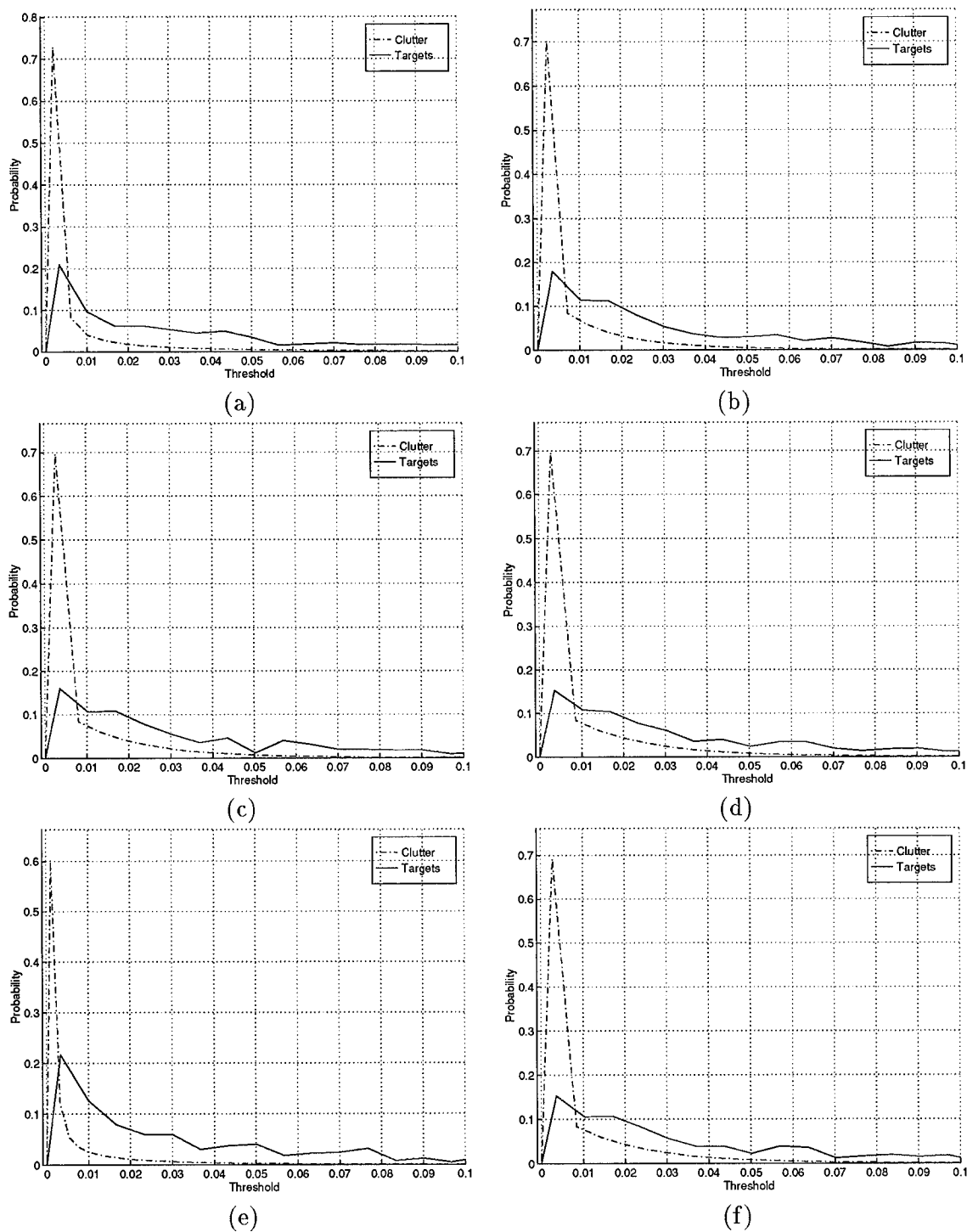


Figure 44. Target and Clutter Pdfs of Data Set 3: (a)  $|HH|^2$ , (b) Average, (c) Span, (d) POW, (e) PMF, and (f) PWF.

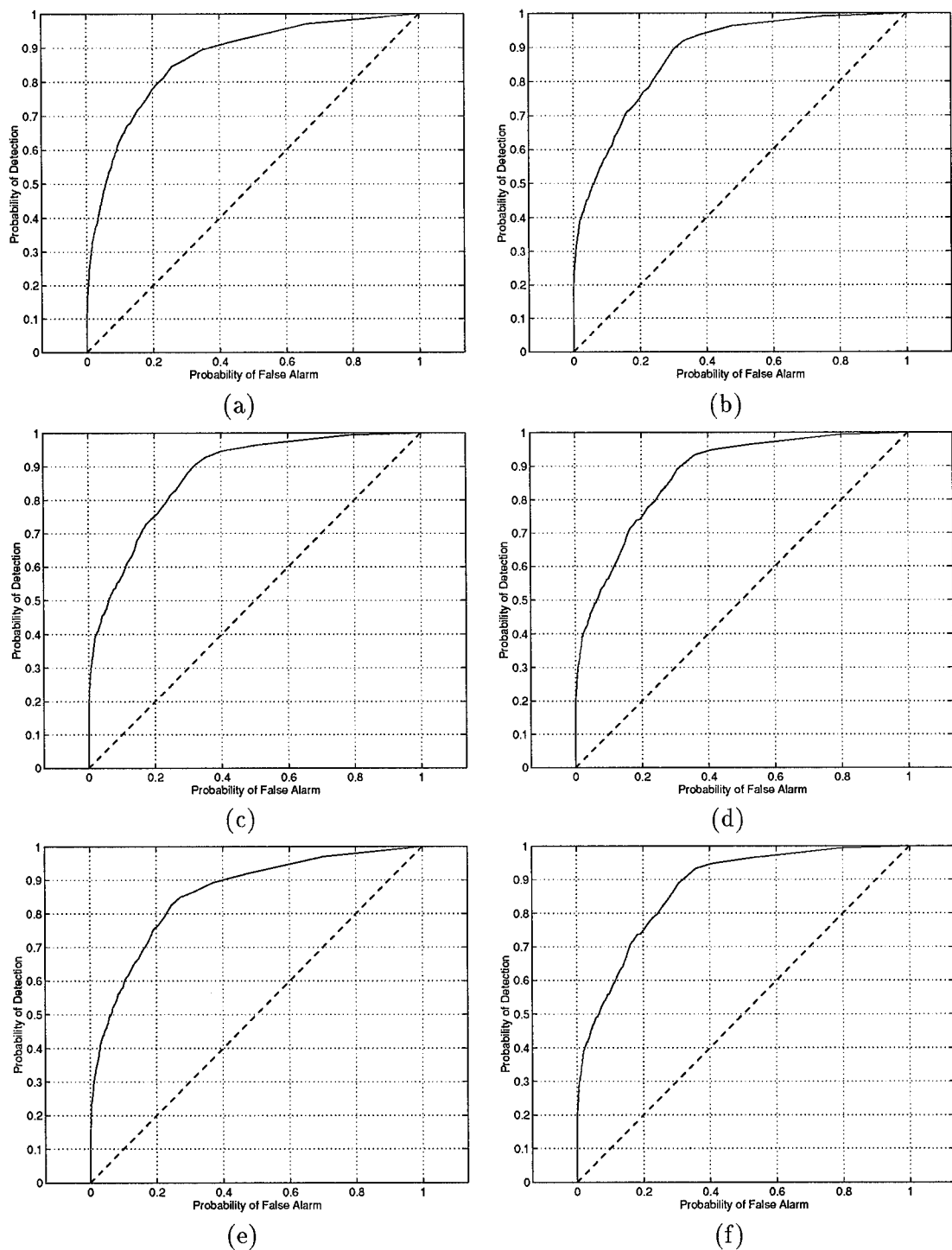


Figure 45. ROC curves for Polarimetric Data Set 3: (a)  $|HH|^2$  (b) Average, (c) Span, (d) POW, (e) PMF, and (f) PWF.

Table 14. S/M and T/C ratios Polarimetric Data Set 4

	HH	HV	VV	Average	Span	POW	PMF	PWF
S/M Ratio	18.91	6.62	16.94	15.53	14.23	11.68	11.90	11.58
T/C Ratio (dB)	17.06	9.35	15.48	16.05	15.65	14.68	14.10	14.69

to be an effective discriminating algorithm using the standard deviation and 2-d correlation coefficient features.

*4.1.4 Polarimetric Data Set 4.* The last polarimetric data set is the most complex. It contains twelve targets, man made clutter (fences, corner reflectors), and different regions of natural clutter.

The polarimetric covariance matrix for this data set is

$$\Sigma_{X-polarDS1} = 0.0064 \begin{bmatrix} 1.00 + j0.00 & 0.0135 - j0.0460 & -0.1008 - j0.0692 \\ 0.0135 + j0.0460 & 0.1797 + j0.00 & 0.0124 - j0.0079 \\ -0.1008 + j0.0692 & 0.0124 - j0.0079 & 0.5893 + j0.00 \end{bmatrix}.$$

The polarimetric images formed by each algorithm are displayed at Figure 47 Referring to Figure 47, the PWF image is the clearest and most defined. The S/M and T/C ratios were calculated for each algorithm and the results are listed in Table 14. As expected the PWF and the OW images have the lowesest S/M ratios (minimum speckle image). The T/C ratios show that the polarimetric average and span algorithms have the highest T/C ratios.

Figure 48 shows plots of clutter and target normalized histograms. All of these plots show that there is a lot of overlap between the two pdfs. None of the algorithms have effectively separated the two pdfs.

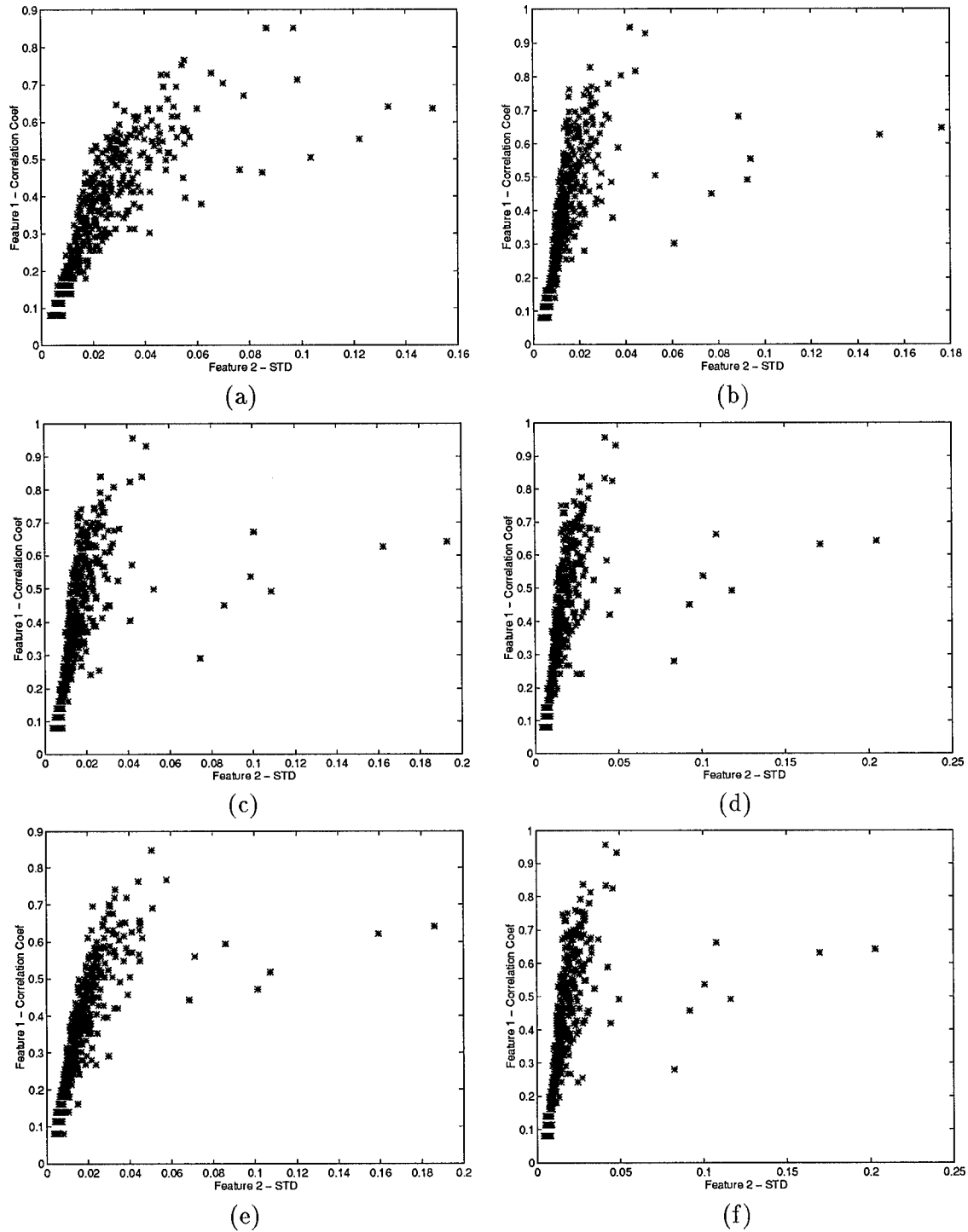


Figure 46. Discriminator Results for Polarimetric Data Set 3: (a)  $|HH|^2$  (b) Average, (c) Span, (d) POW, (e) PMF, and (f) PWF.

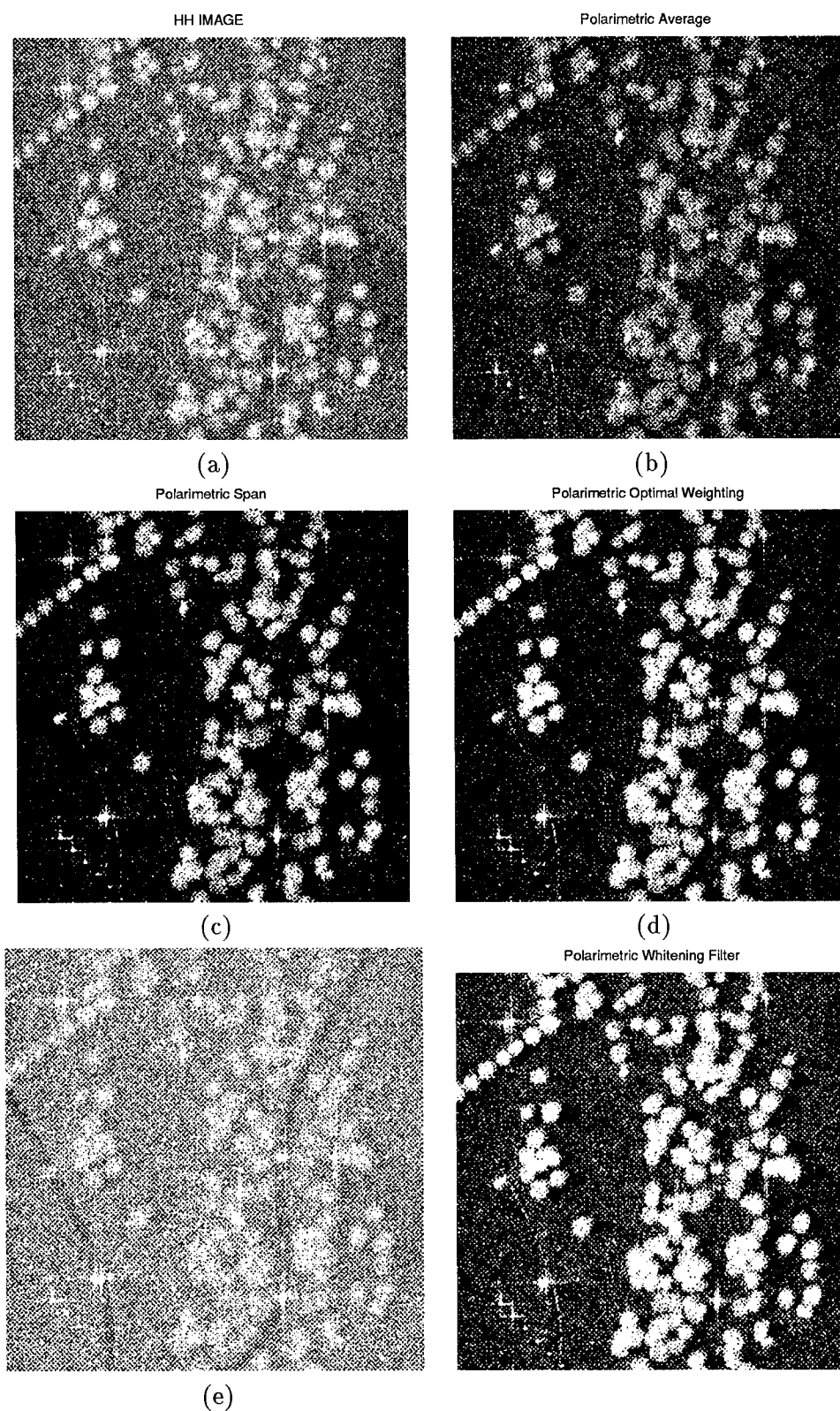


Figure 47. Combined Polarimetric Images of Polarimetric Data Set 4 using: (a)  $|HH|^2$ , (b) Average, (c) Span, (d) POW, (e) PMF, and (f) PWF.

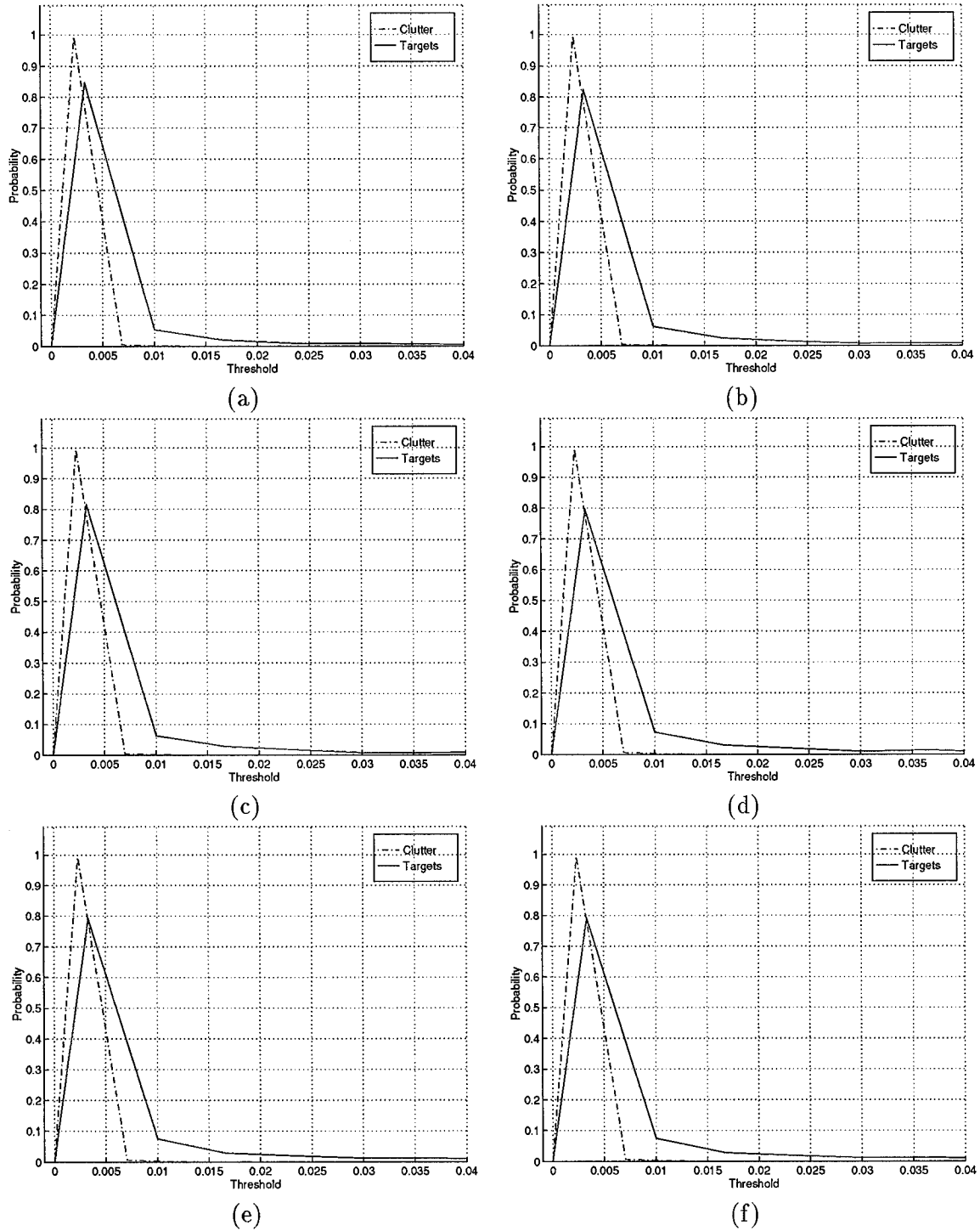


Figure 48. Target and Clutter Pdfs of Data Set 4: (a)  $|HH|^2$ , (b) Average, (c) Span, (d) POW, (e) PMF, and (f) PWF.

Plots of ROC curves for each algorithm are at Figure 49. As was the case for the T/C ratios there is not a large noticeable difference in target detectability between the different polarimetric algorithms.

The results of testing each polarimetrically combined image in the discriminator are shown at Figure 50. This target scene contains a lot more man made clutter (i.e. corner reflectors, fences etc.), hence, the separation is not as defined as it was for Data Set 3 which contains only natural clutter. Notwithstanding, a low standard deviation threshold would effectively eliminate the majority of ground clutter false alarms.

*4.1.5 Target Detection of Polarimetric Algorithms.* Target detection of the different polarimetric images was performed using a constant threshold. This technique involves setting a threshold and testing each pixel within an image with respect to this threshold value. If the PUT exceeds the threshold, a target is declared. As discussed in Section 2.5, at a low threshold all the targets should be detected, however, a low threshold will also generate a large number of false alarms. Increasing the threshold level decreases the number of false alarms but the number of targets detected also decreases. The threshold is set according to system operating requirements (i.e. trade off between number of false alarms and the number of missed detections). All of the images generated from the different techniques were normalized such that the amplitudes of the pixel intensities ranged from zero to one. Figure 51 shows plots of each polarimetric image at the same threshold level of 0.2. The 'x' in the images indicates pixel areas that exceed the threshold and the 'o' shows the actual locations of the targets. The target detection algorithm (Detect.m in Appendix A) would score a hit if one or more pixels in a pixel window of 16 x 10 pixels exceeded the

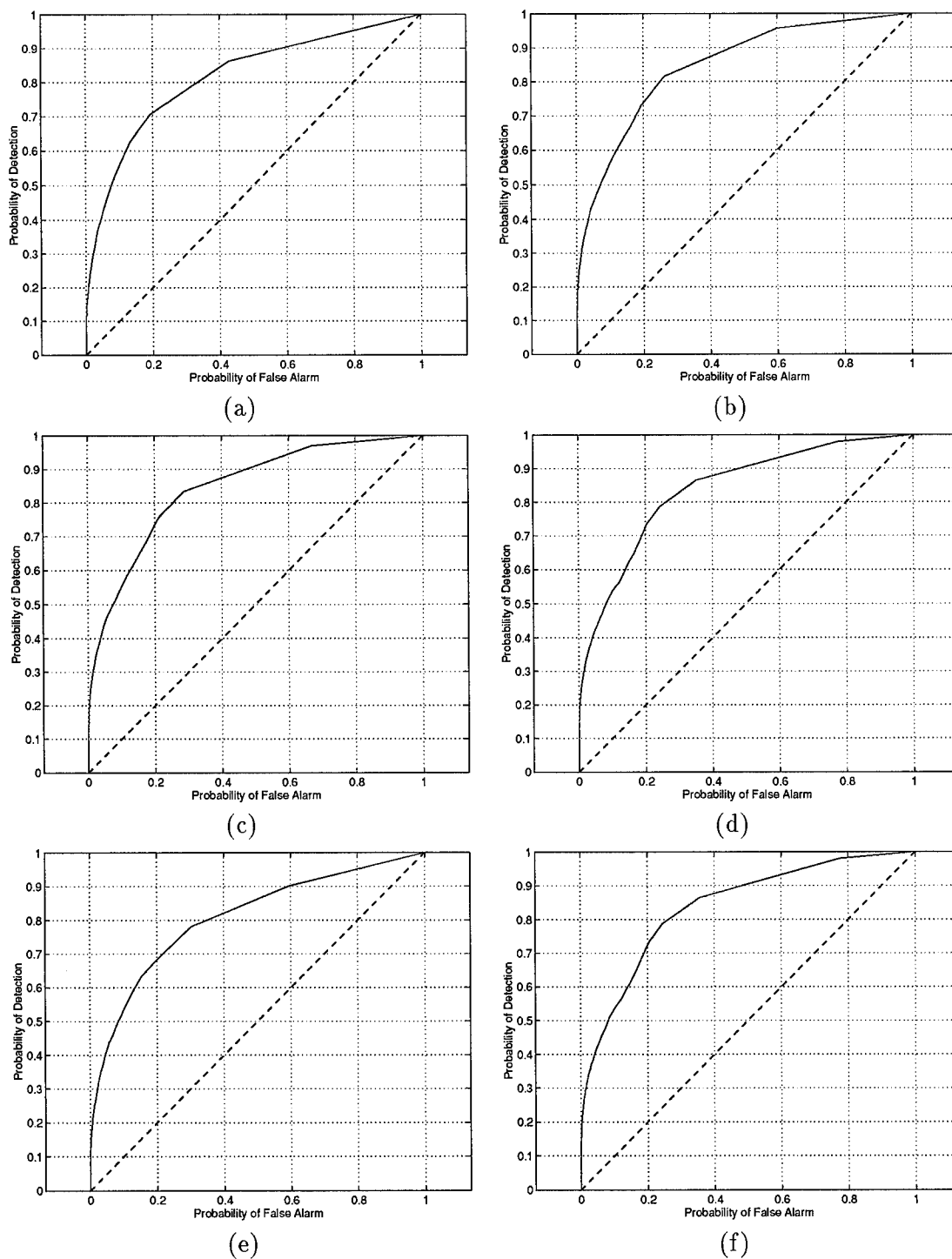


Figure 49. ROC curves for Polarimetric Data Set 4: (a)  $|HH|^2$  (b) Average, (c) Span, (d) POW, (e) PMF, and (f) PWF.



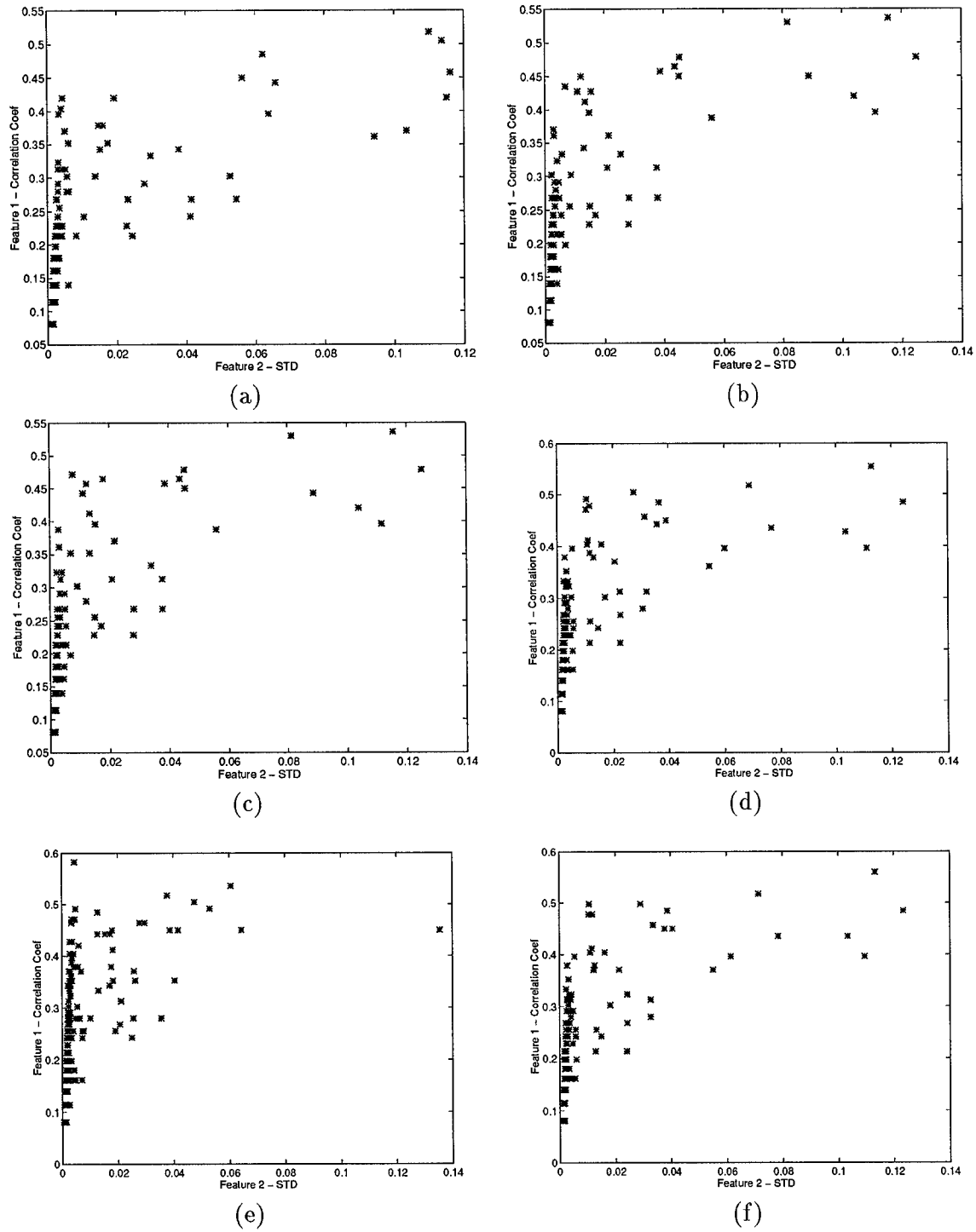


Figure 50. Discriminator Results for Polarimetric Data Set 4: (a)  $|HH|^2$  (b) Average, (c) Span, (d) POW, (e) PMF, and (f) PWF.

threshold. This technique eliminated multiple hits within an area of interest. Referring to Figure 51, all targets were detected in all of the images. However, the number of false alarms, at this low threshold, is high for the  $|HH|^2$ , average and PMF images and zero for the POW, PWF and Span images. If the threshold level is increased, the number of false alarms for the  $|HH|^2$ , average and PMF images decreases until no false alarms are recorded, and the number of missed detections for the POW, PWF and Span images increases. Figure 52, which shows plots of threshold verses detected targets and false alarms, graphically illustrates this point. These plots show that for all the images formed from the different polarimetric algorithms a range of threshold values is reached where all targets are detected for no false alarms. This technique is not suitable for quantifying target detection performance between algorithms. The T/C ratio, ROC curves and discriminator performance are more suitable metrics for assessing and quantifying improvement and hence will be the metrics focused on for assessing the target detection algorithms.

*4.1.6 Discussion of Polarimetric Processing.* The analysis performed in this section showed that the polarimetric algorithms did not provide any significant improvement in target detection performance. The PWF image had the lowest S/M ratio indicating a minimum speckled image was formed. Figures 43 and 47 illustrate this point. The T/C ratios for all polarimetric algorithms were lower than the maximum T/C ratio of the unprocessed images (refer Tables 12, 13 and 14). Plots of target and clutter normalized histograms and ROC curves also did not indicate any significant improvement in target detection over the unprocessed images. However, the discriminator results showed that the PWF, POW and Span algorithms effectively separated targets from clutter false alarms in

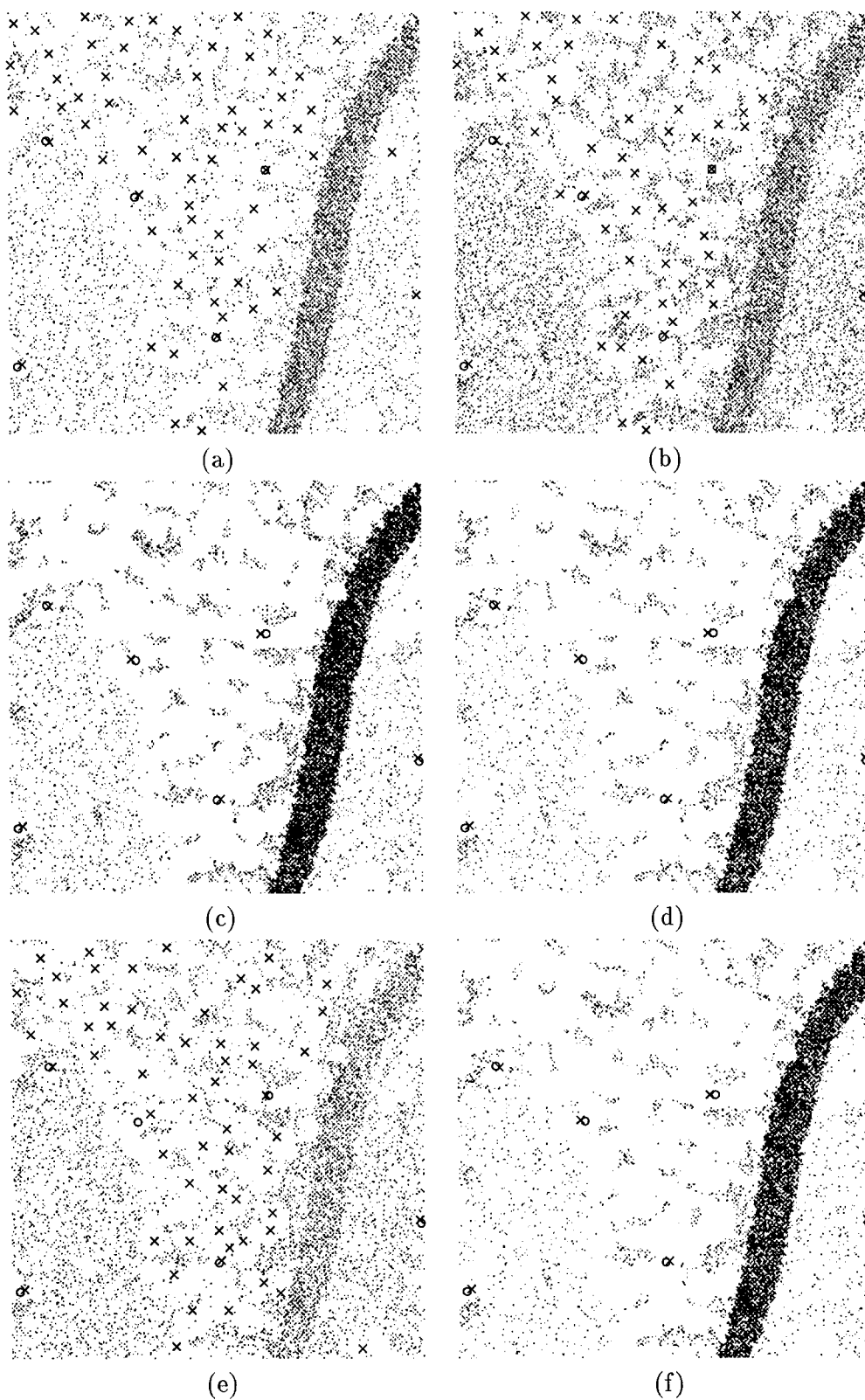
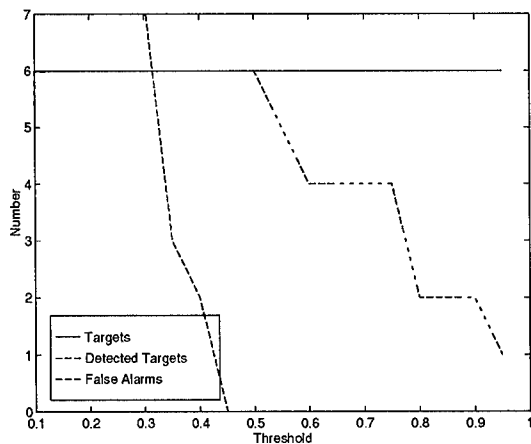
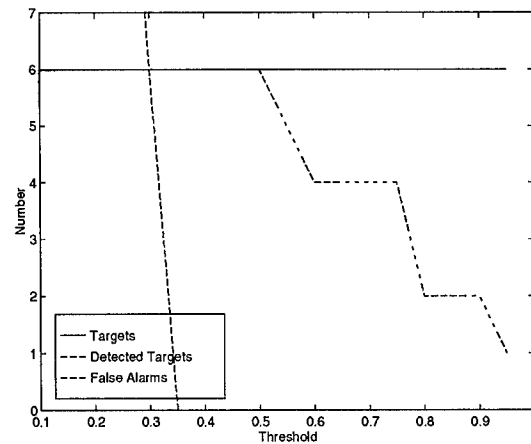


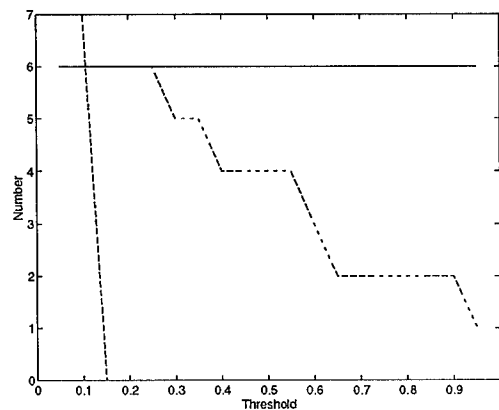
Figure 51. Target detection performance of polarimetric Data Set 3 using a constant threshold for: (a) HH , (b) Average, (c) Span, (d) POW, (e) PMF and (f) PWF.



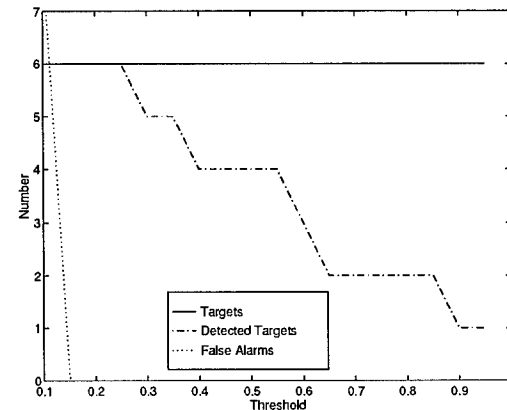
(a)



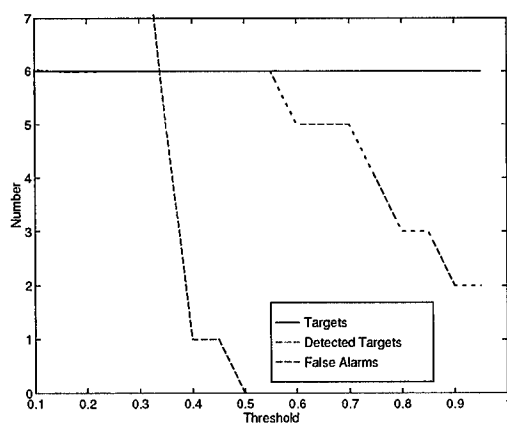
(b)



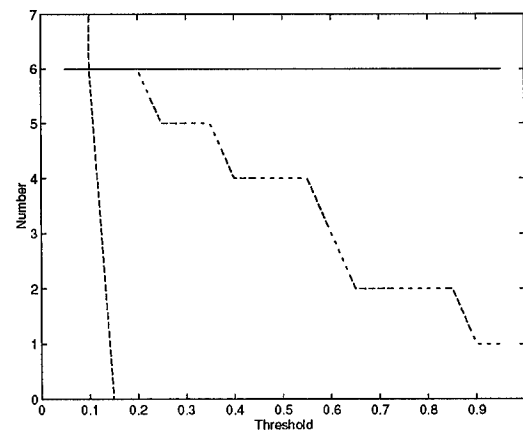
(c)



(d)



(e)



(f)

Figure 52. Target detection performance of Data Set 3 using a constant threshold for: (a) HH, (b) Average, (c) Span, (d) POW, (e) PMF, and (f) PWF.

feature space. Results from the use of a constant threshold detector showed that all targets were detectable (in a range of thresholds) for no clutter false alarms. At low thresholds, the PWF, POW and Span images had the minimum number of clutter false alarms when compared to the other polarimetric algorithms. However, this technique was considered unsuitable for comparing the algorithms.

#### 4.2 Wide Angle Processing

This section provides the results of combining the images at different aspect angles into the one image for target detection purposes. Three wide angle algorithms are investigated: 1) Average, 2) WWF, and 3) AWWF. The wide angle matched filter was not tested because this algorithm relies on *a priori* information of target locations. For the AWWF, algorithm results are presented for two cases: 1) a window size of 20 x 20 pixels; and 2) a window size of 10 x 10. The algorithms are compared with respect to S/M ratios, T/C ratios, target and clutter pdfs, ROC curves and discriminator performance.

Three wide angle data sets have been used for this analysis. Wide angle Data Set 1 comes from the same set of images used for the polarimetric analysis. The full data set contains 9 images (HH, HV and VV at aspect angles of  $-30^\circ$ ,  $0^\circ$  and  $+30^\circ$ ). The image contains no targets, it contains simple ground clutter, and the HH set of the images shall be used (i.e. 3 images HH @  $-30^\circ$ , HH @  $0^\circ$  and HH @  $+30^\circ$ ). The second data set is a segment of the WASAR data set that contains only one target in simple ground clutter. This data set contains seven images and the HH subset shall be used (i.e. 7 images HH @  $-45^\circ$ , HH @  $-30^\circ$ , HH @  $-15^\circ$ , HH @  $0^\circ$ , HH @  $+15^\circ$ , HH @  $+30^\circ$  and HH @  $+45^\circ$ ). Figure 37 shows images of these first two data sets. The third data set is the WASAR

Table 15. S/M ratios for Wide Angle Data Set 1

$ HH ^2$ -30°	$ HH ^2$ 0°	$ HH ^2$ 30°	Average	WWF
1.2667	1.2738	1.2664	0.7302	0.7307

Data Set1. The ground scene and polarimetric images of this data set are at Figures 11 and 13 respectively. The HH set of images at the 7 different aspect angles shall be used.

*4.2.1 Wide Angle Data Set 1.* This data set contains no targets. The purpose of this analysis is to confirm the results obtained in the analysis of wide angle clutter covariance matrices and investigate the S/M ratio for the unprocessed images and for each wide angle algorithm.

The WACM for this data set is

$$\Sigma_{X-WACM-DS1} = 0.0064 \begin{bmatrix} 1.00 + j0.00 & -0.0071 - j0.0059 & 0.0042 + j0.0067 \\ -0.0071 + j0.0059 & 1.0126 + j0.00 & 0.0070 + j0.0015 \\ 0.0042 - j0.0067 & 0.0070 - j0.0015 & 0.9527 + j0.00 \end{bmatrix}.$$

The form of this covariance matrix is as expected. That is, the return at different aspect angles for ground clutter is relatively constant. S/M ratios were computed for each unprocessed image and for each wide angle algorithm. The results are at Table 15.

The S/M ratios illustrate that the Average and the WWF have reduced the speckle compared to the unprocessed images, and there appears to be no difference between the two algorithms. For the ‘*no target*’ condition the WACM is simply an identity matrix. Accordingly, the WWF and the average algorithm are the same for the ‘*no target*’ condition.

*4.2.2 Wide Angle Data Set 2.* This data set contains seven images (aspect angles  $-45^\circ$  to  $-45^\circ$  in  $-15^\circ$  increments). The target scene contains one target and one tree in ground clutter. The Average, WWF, AWWF (20 x 20 pixels) and the AWWF (10 x 10 pixels) are used to form a single image for target detection testing. For this data set S/M ratios and T/C ratios are computed and the algorithms are evaluated by plotting target and clutter pdfs, ROC curves and discriminator performance.

The WACM for this data set is

$$\Sigma_{X-WACM-DS2} = 0.0527 \begin{bmatrix} 0.5228 & 0.0473 & 0.1082 & 0.0218 & 0.0587 & 0.0437 & 0.0385 \\ 0.0473 & 0.3778 & 0.0601 & 0.0715 & 0.0514 & 0.0186 & 0.0482 \\ 0.1082 & 0.0601 & 0.3715 & 0.0239 & 0.0552 & 0.0473 & 0.0124 \\ 0.0218 & 0.0715 & 0.0239 & 1.0000 & 0.2687 & 0.1617 & 0.0181 \\ 0.0587 & 0.0514 & 0.0552 & 0.2687 & 0.7121 & 0.1853 & 0.0752 \\ 0.0437 & 0.0186 & 0.0473 & 0.1617 & 0.1853 & 0.7712 & 0.0245 \\ 0.0385 & 0.0482 & 0.0124 & 0.0181 & 0.0752 & 0.0245 & 0.3295 \end{bmatrix}.$$

Referring to the angle covariance matrix, the largest values are along the main diagonal of the matrix. The maximum value occurs in the middle of the matrix which corresponds to the  $0^\circ$  aspect image. The form of the WACM is in line with the results of a target WACM presented in Chapter III. That is, the diagonal elements of the WACM vary for different aspect angles.

The S/M and T/C ratios were calculated for each algorithm and the results are listed in Table 16. The S/M results show that the WWF produces the image with the smallest S/M ratio of all the wide angle combining algorithms. The T/C ratios show that the

Table 16. S/M and T/C ratios Wide Angle Data Set 2

	Ave	WWF	AWWF-1	AWWF-2
S/M	9.44	9.32	13.87	15.63
T/C (dB)	20.87	20.80	24.34	24.68

AWWF with a non overlapping window size of 10 x 10 pixels has a 3.8 dB improvement over the average algorithm and a 1.6 dB improvement over the strongest unprocessed image (HH @ 0°). Comparing this result to the polarimetric algorithms (refer Table 12), for the exact same target scene, the AWWF (10 x 10 pixel window) has an improvement of 2.8 dB over the PMF (which uses *a priori* knowledge of the targets location), and a 4.5 dB improvement over the next best (average) polarimetric combining algorithm. Accordingly, using the T/C metric, wide angle processing - in particular the AWWF - provides significantly better target detection performance than the other polarimetric algorithms. Figure 53 shows selected regions of the unprocessed image and the AWWF (10 x 10 pixel window) image. This figure illustrates the enhancement effect of all the pixels within a pixel window containing a target.

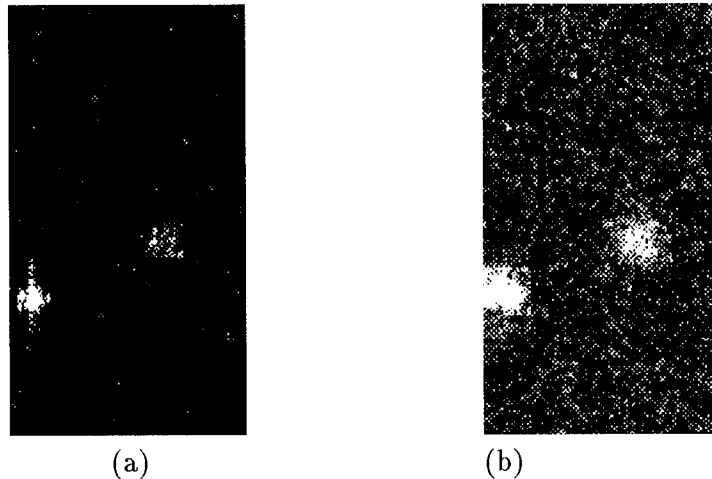


Figure 53. Images of: (a)  $|HH|^2$  0°, and (b) AWWF (10 x 10 pixels)



Figure 54 shows plots of clutter and target normalized histograms of each wide angle algorithm for wide angle Data Set 2. The HH image at an aspect angle of  $+15^\circ$  is used as a reference. These plots show that the wide angle algorithms have increased the variance of the targets pdf. That is, for the unprocessed image (Figure 54(a)) the mean value of the target histogram is closer to the clutters. Whereas, the mean value of the target histograms, for the wide angle algorithms, is further away from the clutter pdf. Thus, these algorithms have separated the two pdfs.

Plots of ROC curves for each algorithm are at Figure 55. Referring to this set of plots, a major difference can be seen between the unprocessed image  $|HH|^2 +15^\circ$  and the wide angle algorithms. The AWWF (10 x 10 pixels) ROC curve is clearly the best result for this data set. This algorithm provides a significantly higher  $P_D$  for a very low  $P_{fa}$ . Further, all the wide angle algorithms show significantly better results than the polarimetric algorithms (refer polarimetric ROC curves Figure 41). Accordingly, using the ROC curves as a measure of target detection performance also confirms the T/C results that the wide angle algorithms out perform the polarimetric algorithms.

The results of testing each polarimetrically combined image in the discriminator, using a pixel window of 16 x 8 pixels are shown at Figure 56. Referring to Figure 56, these plots show that the AWWF (for both window sizes) algorithm, combined with the threshold detector and discriminator, effectively eliminated all but one ground clutter false alarm, the tree is displayed centrally (in feature space) between the ground clutter and the target, and the single target is shown in the top right hand corner of the feature plot (i.e. high correlation coefficient and high standard deviation). Thus, the discriminator

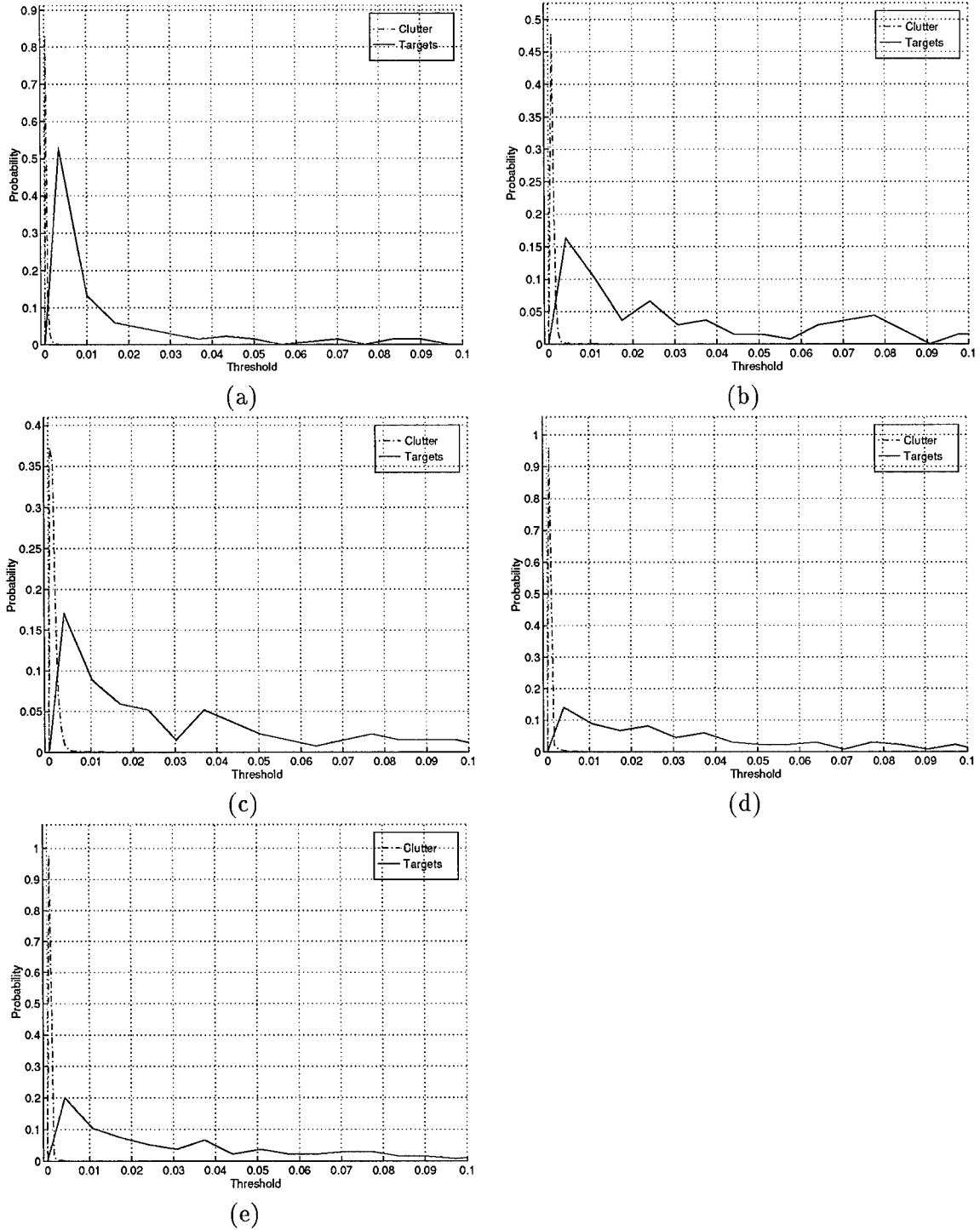


Figure 54. Target and Clutter Pdfs of Wide Angle Data Set 2: (a)  $|HH|^2 + 15^\circ$ , (b) Average, (c) WWF, (d) AWWF (20 x 20) pixels, and (e) AWWF (10 x 10 pixels).

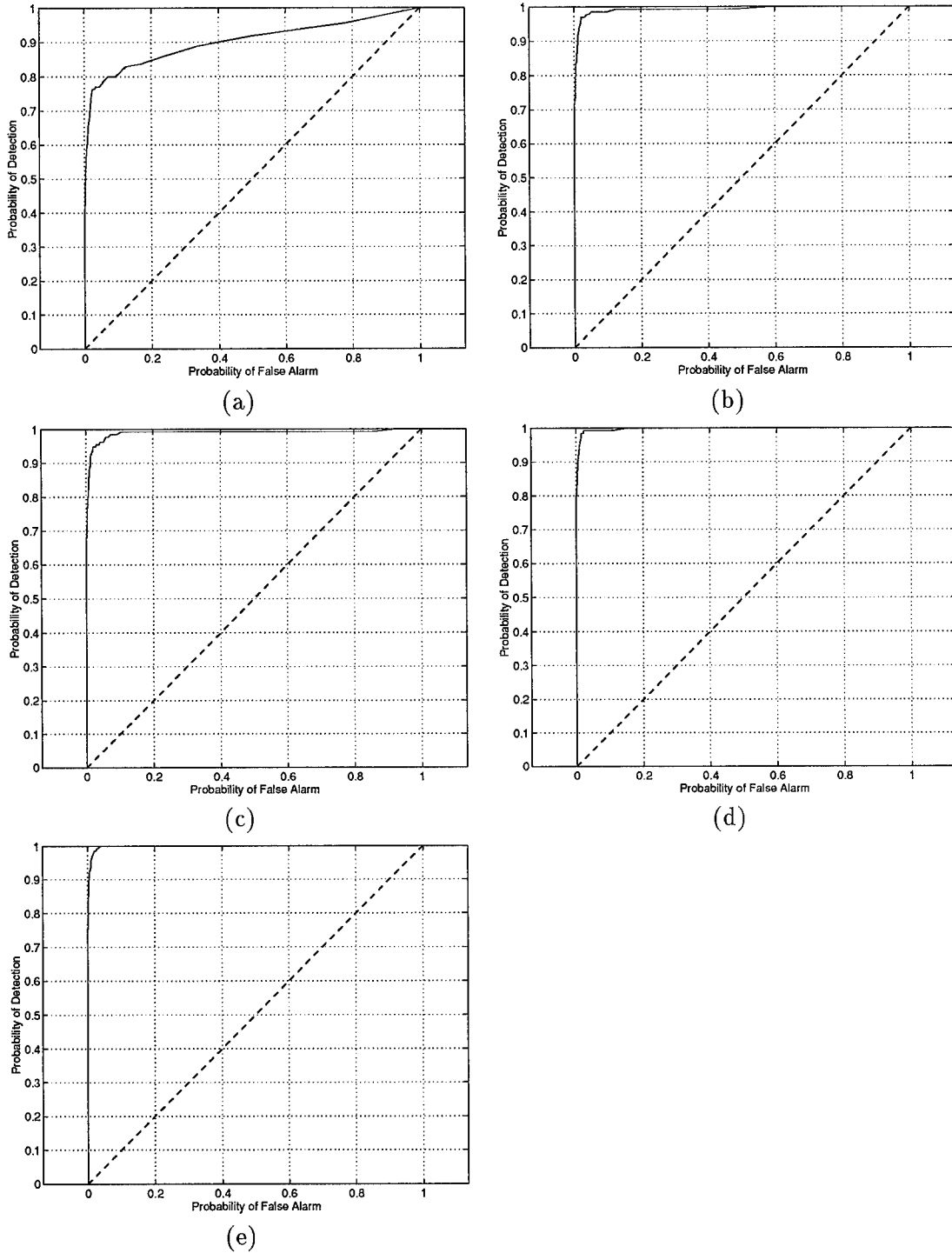


Figure 55. ROC curves for Wide Angle Data Set 2: (a)  $|HH|^2 + 15^\circ$  (b) Average, (c) WWF, (d) AWWF (20 x 20 pixels), (e) AWWF (10 x 10 pixels) Filter.

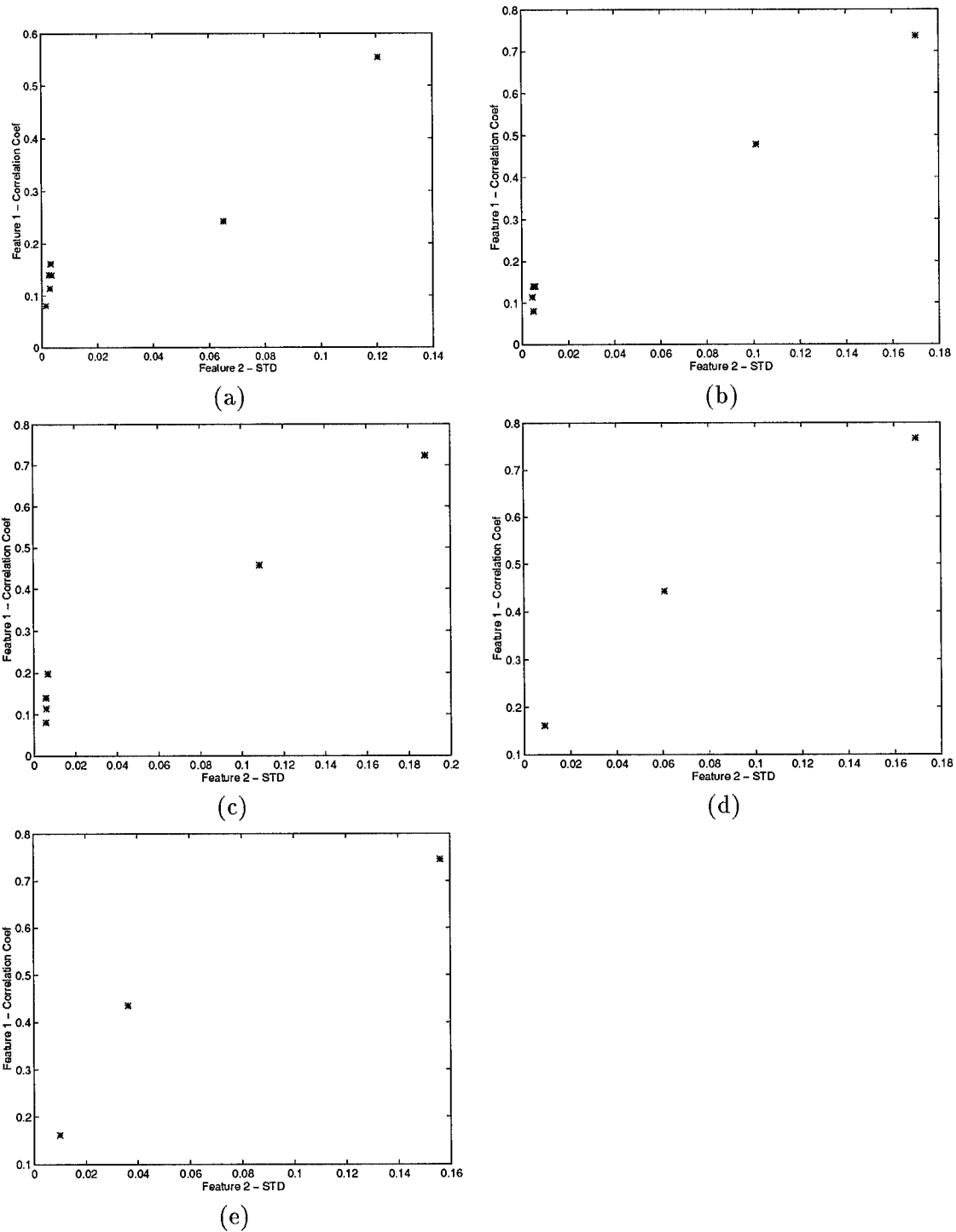


Figure 56. Discriminator Results for Polarimetric Data Set 4: (a)  $|HH|^2$  (b) Average, (c) WWF (d) AWWF (20 x 20 pixels), and (e) AWWF (10 x 10 pixels)

also shows that the wide angle algorithms discriminate targets from clutter false alarms more effectively than do the polarimetric algorithms.

*4.2.3 Wide Angle Data Set 3.* This final wide angle data set contains seven images (aspect angles  $-45^\circ$  to  $45^\circ$  in  $15^\circ$  increments). The target scene is more complex, containing five targets and two different terrain categories. The Average, WWF, AWWF-1, and AWWF-2 algorithms are used to combine the seven images into the one image for target detection testing. Testing of this wide angle image involves computing S/M and T/C ratios, plotting target and clutter histograms, ROC curves and discriminator output curves.

The WACM for this data set is

$$\Sigma_{X-WACM-DS3} = 0.0436 \begin{bmatrix} 0.8996 & 0.0088 & 0.0290 & 0.0211 & 0.0057 & 0.0047 & 0.0089 \\ 0.0088 & 0.8565 & 0.0127 & 0.0101 & 0.0067 & 0.0075 & 0.0113 \\ 0.0290 & 0.0127 & 0.8885 & 0.0123 & 0.0102 & 0.0077 & 0.0064 \\ 0.0211 & 0.0101 & 0.0123 & 1.0000 & 0.0228 & 0.0117 & 0.0031 \\ 0.0057 & 0.0067 & 0.0102 & 0.0228 & 0.9222 & 0.0369 & 0.0155 \\ 0.0047 & 0.0075 & 0.0077 & 0.0117 & 0.0369 & 0.9620 & 0.0014 \\ 0.0089 & 0.0113 & 0.0064 & 0.0031 & 0.0155 & 0.0014 & 0.8289 \end{bmatrix}.$$

Referring to the angle covariance matrix, the largest values are along the main diagonal of the matrix. The maximum value occurs in the middle of the matrix which corresponds to the 0 degree aspect image. This form of the WACM is in line with the

Table 17. S/M and T/C ratios for Wide Angle Data Set 3

	Ave	WWF	AWWF-1	AWWF-2
S/M	3.0926	4.2938	13.87	15.63
T/C (dB)	13.20	14.58	16.14	16.21

results of a target and clutter WACM presented in Chapter III. That is, the diagonal elements of the WACM are approximately uniform.

The S/M and T/C ratios were calculated for each algorithm and the results are listed in Table 17. The S/M results show that the Average produces the image with the smallest S/M ratio of all the wide angle combining algorithms. The T/C ratios show that the AWWF with a non overlapping window size of 10 x 10 pixels has a 3 dB improvement over the average algorithm, however it is 0.23 dB less than the best unprocessed images T/C ratio (HH @ 0°). This unusual result is due to a very high HH 0° return. The S/M ratio for the HH 0° is considerably higher than the S/M ratios of the images at other aspect angles. Further, an examination of the intensity image of the HH @ 0° (refer Figure 58) reveals bright glints where the targets are located. The VV and HV data sets were tested and the AWWF (10 x 10) T/C ratio showed an improvement of 1.8 dB over the strongest return for the HV data set and a 0.4 dB improvement over the strongest HV return.

Comparing the T/C results to the polarimetric algorithms (refer Table 12), for the exact same target scene, the AWWF (10 x 10 pixel window) has an improvement of 5.34 dB over the PMF (which uses a priori knowledge of the targets location), and a 5.72 dB improvement over the PWF. Accordingly, using the T/C metric wide angle processing, in particular the AWWF provides significantly better target detection performance than the polarimetric algorithms.

Figure 58 shows the images formed from the different wide angle algorithms. These images highlight the following points. First, the average algorithm destroys the quality of the image, however, the averaging effect highlights the targets and reduces the intensity of the trees and ground clutter. The WWF, on the other hand, maintains the image's quality and shows a 1.38 dB improvement in T/C ratio over the WASAR average. Finally, the AWWF significantly highlights the target's location by enhancing all the pixels in the location of the target, leaving squares of high intensity pixels. The smaller windowed AWWF has primarily enhanced the target and not the surrounding clutter (refer Figure 58 (e)).

For a square non overlapping window, the optimum window size was determined by decreasing the window size from 60 x 60 pixels down to 2 x 2 pixels and computing the T/C ratio for each AWWF image formed. Using this method the optimum sized window was determined to be a 10 x 10 pixel window. This result is graphically illustrated in Figure 57 which is a plot of T/C ratio versus window size.

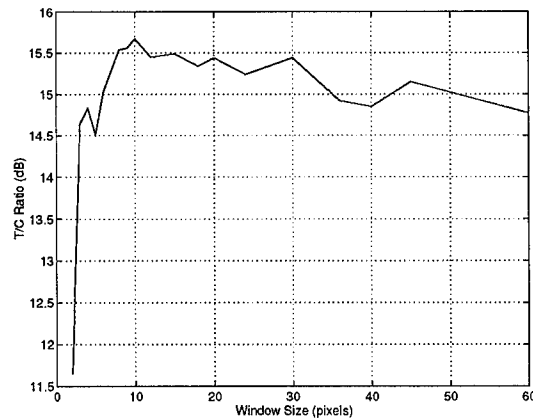


Figure 57. Plot of Window Size versus T/C Ratio

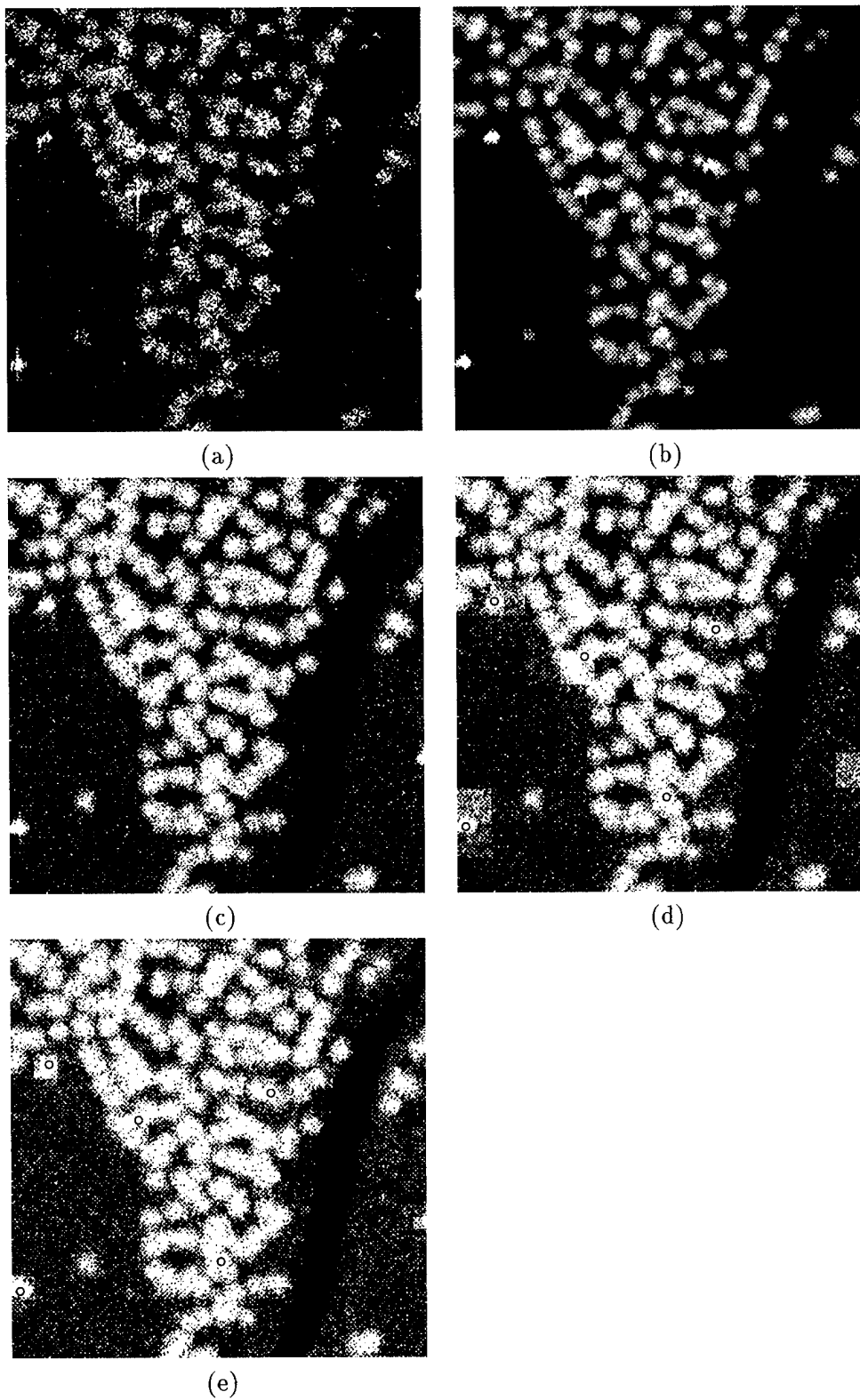


Figure 58. Combined Wide Angle Images of Data Set 3 using the: (a)  $|HH|^2$   $0^\circ$  (b) Average, (c) WWF, (d) AWWF (30 x 30 pixels), and (e) AWWF (10 x 10 pixels).



Figure 59 shows plots of clutter and target normalized histograms of each wide angle algorithm for wide angle Data Set 2. The HH image at an aspect angle of  $+15^\circ$  is used as a reference. All of the wide angle algorithms have effectively separated the target and clutter pdfs.

Plots of ROC curves for each algorithm are at Figure 60. Referring to this set of plots, a big difference can be seen between the unprocessed image  $|HH|^2 +15^\circ$  and the wide angle algorithms. As was the case with wide angle Data Set 2, the AWWF (10 x 10 pixels) ROC curve is clearly the best result for this data set. This algorithm provides a significantly higher  $P_D$  for a very low  $P_{fa}$ . Further, all the wide angle algorithms show significantly better results than the polarimetric algorithms (refer polarimetric ROC curves Figure 45). Accordingly, using the ROC curves as a metric of target detection performance also confirms the T/C results that the wide angle algorithms out perform the polarimetric algorithms.

The results of testing each polarimetrically combined image in the discriminator, using a pixel window of 16 x 8 pixels are shown at Figure 61.

*4.2.4 Summary of Wide Angle Processing.* The wide angle algorithms showed better T/C ratios and ROC curve results for the same target scenes than all of the polarimetric algorithms. Figure 62 is a plot of ROC curves of WASAR Data Set 1 for the AWWF, WWF, PWF algorithms and the  $|HH|^2 +15^\circ$  unprocessed image. From this figure, the AWWF algorithm provides the best target detection performance of all the wide angle and polarimetric algorithms investigated. The simpler WWF also provides a significant improvement in target detection compared to the polarimetric algorithms. This

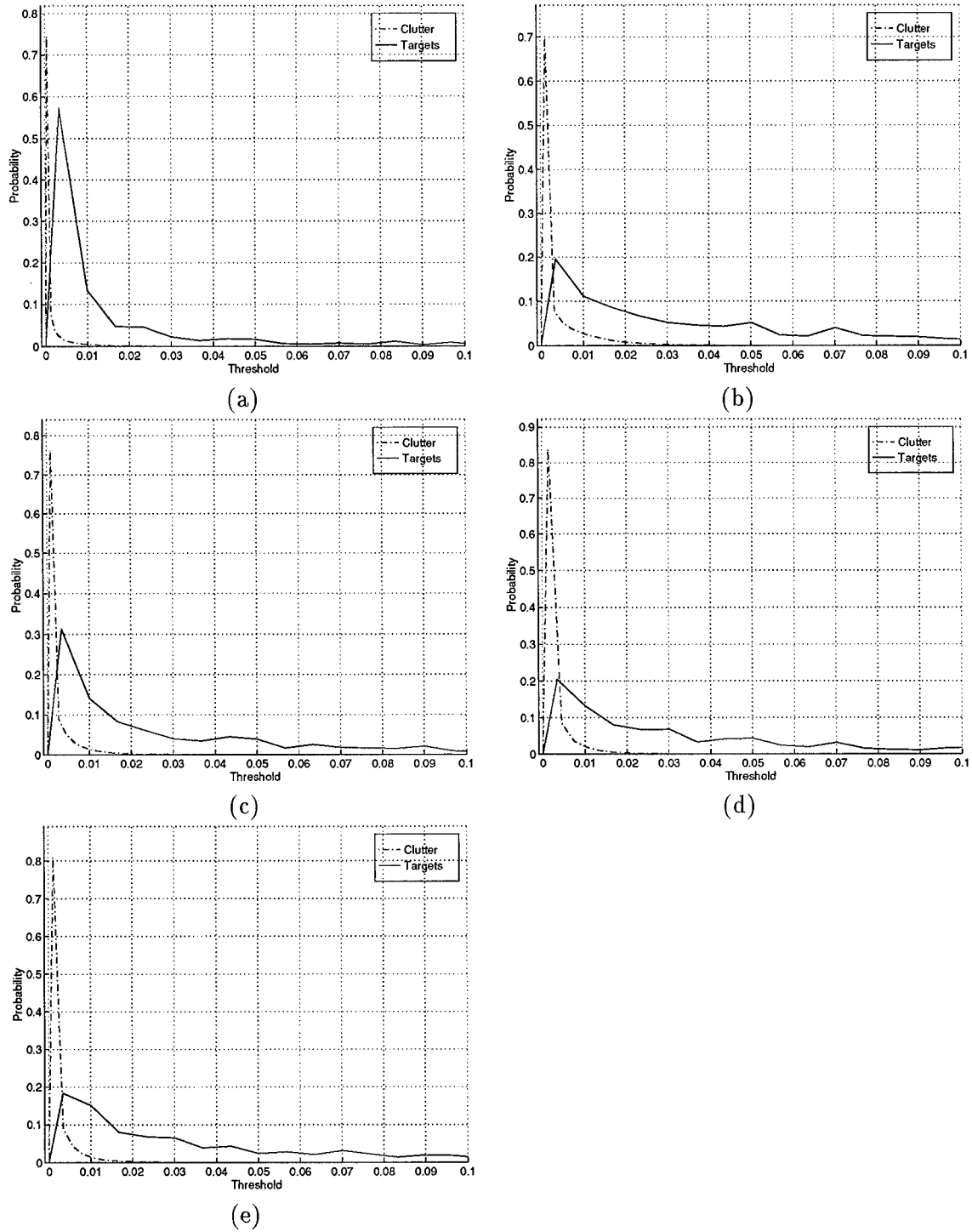


Figure 59. Target and Clutter Pdfs of Wide Angle Data Set 3: (a)  $|HH|^2 + 15^\circ$ , (b) Average, (c) WWF, (d) AWWF (30 x 30) pixels, and (e) AWWF (10 x 10 pixels).

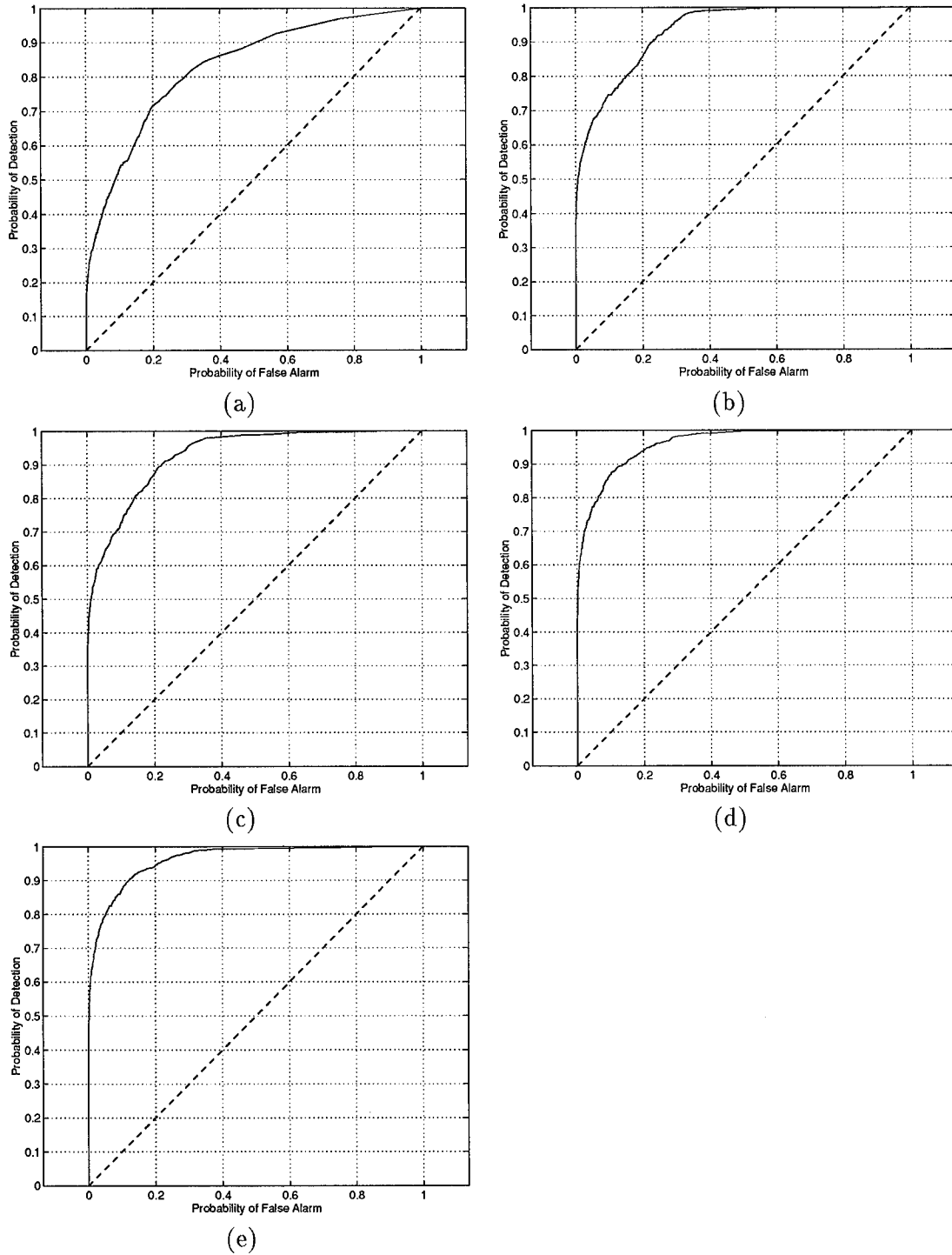


Figure 60. ROC curves for Wide Angle Data Set 3: (a)  $|HH|^2 + 15^\circ$  (b) Average, (c) WWF, (d) AWWF (30 x 30 pixels), (e) AWWF (10 x 10 pixels) Filter.

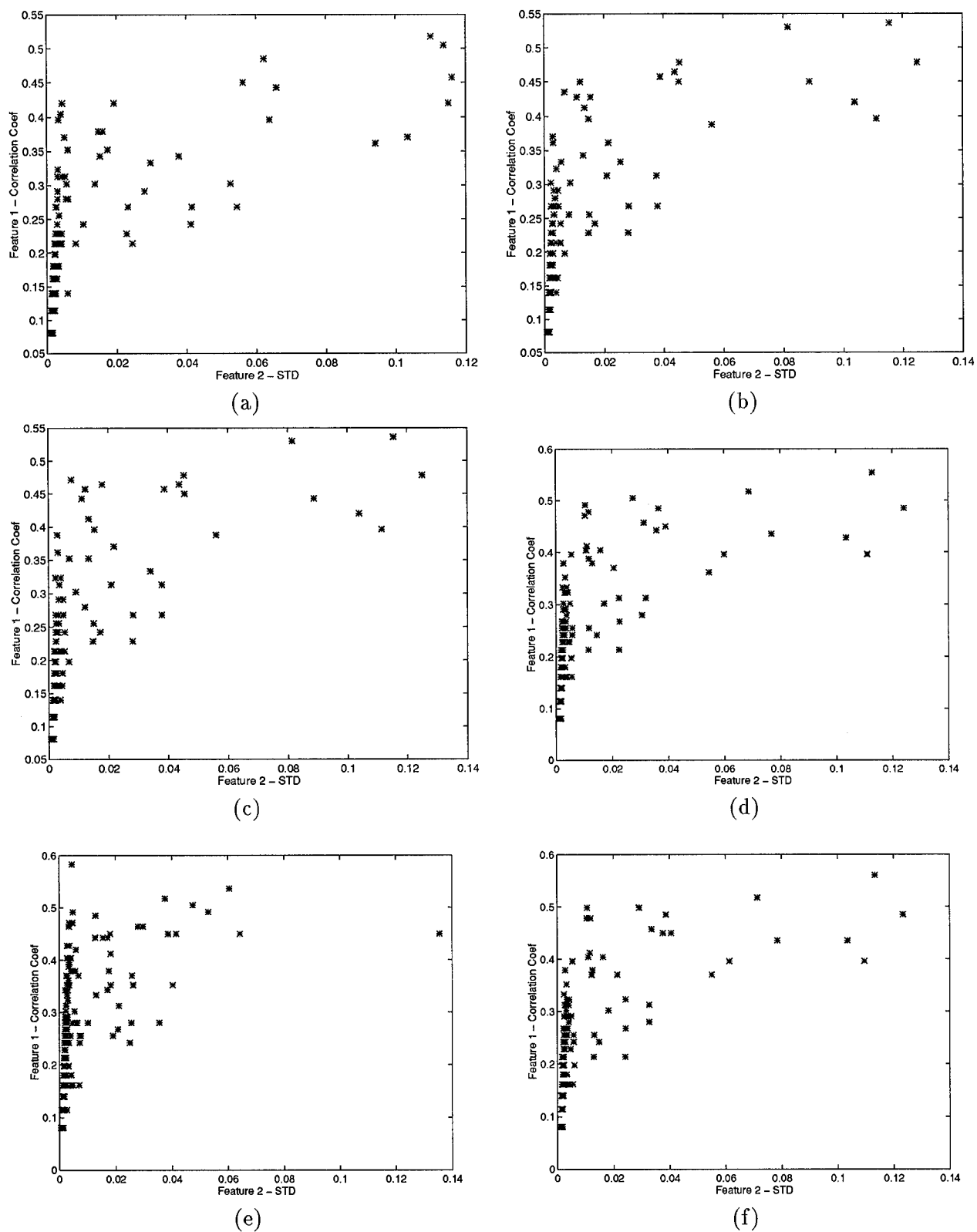


Figure 61. Discriminator Results for Polarimetric Data Set 3: (a)  $|HH|^2$  (b) Average, (c) Span, (d) Optimal Weighting, (e) Polarimetric Matched Filter, and (f) Polarimetric Whitening Filter.<sup>125</sup>

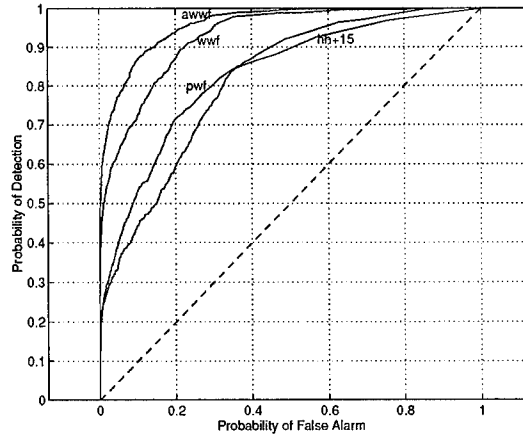


Figure 62. ROC curves of AWWF, WWF, PWF and  $|HH|^2 + 15^\circ$

comparison is based on seven different aspect images combined into the one image versus three different polarimetric images. In the following section a direct comparison of three different aspect images versus three polarimetric images is presented.

#### 4.3 Comparison of Polarimetric and Wide Angle Processing

In Section 4.2 it was shown primarily through the T/C ratio and ROC curves, that wide angle processing provided superior results to polarimetric processing. In this section, a direct comparison of three wide angle images versus three polarimetric images is presented. WASAR Data Set 1 shall be used for the analysis (i.e. 21 fully polarimetric images at 7 different aspect angles). For the wide angle images different combinations of three images at different aspect angles selected from the seven VV images of the WASAR data set shall be used. The different combinations of three images include the following: 1)  $-45^\circ : 0^\circ : +45^\circ$ , 2)  $-15^\circ : 0^\circ : +15^\circ$ , 3)  $-45^\circ : -30^\circ : -15^\circ$ , 4)  $+45^\circ : +30^\circ : +15^\circ$ , 5)  $-30^\circ : 0^\circ : +30^\circ$ , 6)  $-45^\circ : 0^\circ : +30^\circ$ , and 7)  $0^\circ : +30^\circ : +45^\circ$ . The combination with the highest T/C ratio shall be used to compare with a polarimetric set of images. Likewise, T/C

Table 18. T/C ratios for seven different polarimetric data sets

	-45°	-30°	-15°	0°	+15°	+30°	+45°
Ave (dB)	11.56	10.58	9.87	14.68	11.97	13.84	12.27
Span (dB)	11.28	12.27	9.44	14.27	11.52	13.60	12.32
PWF (dB)	11.01	10.49	9.23	13.85	11.05	13.46	12.36

Table 19. T/C ratios for wide angle aspect angle combinations

	1	2	3	4	5	6	7
Ave (dB)	12.59	11.78	10.81	12.94	12.89	12.68	13.61
WWF (dB)	13.40	12.22	11.22	13.48	13.52	13.34	14.30
AWWF (dB)	14.25	13.91	11.52	16.24	14.84	14.13	15.97

ratios shall be computed for the seven different polarimetric data sets and the polarimetric data set with the highest T/C ratio shall be used in the comparison. The polarimetric algorithms being tested include the Span, Average and PWF. The wide angle algorithms being tested include the Average, WWF and the AWWF (10 x 10 pixels). ROC curves for each algorithm are computed and plotted.

Table 18 lists the T/C ratios for the seven different polarimetric data sets for the Average, Span and PWF algorithms. In Table 18 the largest T/C ratio is the Average algorithm at 0° aspect angle (T/C=14.68).

Table 19 lists the T/C ratios for the seven different aspect angle combinations for the Average, WWF and the AWWF (10 x 10 pixels) algorithms.

Referring to Table 19, the AWWF provides the highest T/C ratio for all combinations of aspect angle images, followed by the WWF. The WWF provides, on average, 0.5 to 1 dB improvement over the simple average algorithm whereas the AWWF provides 2-3 dB improvement over the average algorithm.

A comparison between the T/C ratios of the polarimetric algorithms and the wide angle algorithms shows that the maximum T/C ratio occurs for the AWWF (16.24 dB). Further, most of the T/Cs exceed the T/C ratios of the wide angle algorithms exceed the T/C ratios of the polarimetric algorithms (refer Tables 18 and 19).

Figure 63(a) shows plots of ROC curves for the best wide angle algorithm (AWWF) and the best polarimetric algorithm (Average). This plot also confirms the T/C ratio results that the wide angle algorithms investigated, in particular the AWWF, provide superior target detection performance to the polarimetric algorithms.

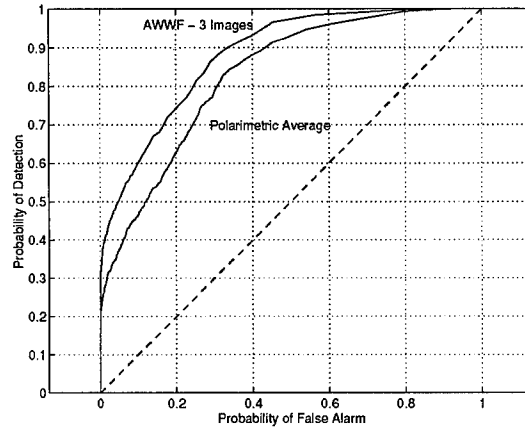


Figure 63. Direct Comparison of Wide Angle and Polarimetric Algorithms

#### 4.4 Combination of Polarimetric and Wide Angle Algorithms

This section describes a study that combined the polarimetric and multi aspect angle images using different combinations of the polarimetric and wide angle algorithms investigated by this research. The objective of this study was to determine the optimum method of combining the 21 images of WASAR Data Set 1 for target detection purposes. Target detection performance is measured using the T/C ratio and plots of ROC curves.

Seven different combinations of polarimetric and wide angle algorithms were implemented. The seven algorithms compared are as follows.

- *Algorithm 1:* Combine the three polarimetric images at different aspect angles using the PWF and then combine these seven images using the AWWF.
- *Algorithm 2:* Combine the seven polarimetric images at different polarizations using the WWF then combine these three images using the PWF.
- *Algorithm 3:* Combine the three polarimetric images at different aspect angles using the Polarimetric Average and then combine these seven images using the Wide Angle Average.
- *Algorithm 4:* Combine the three polarimetric images at different aspect angles using the Polarimetric Average and then combine these seven images using the WWF.
- *Algorithm 5:* Combine all 21 images by forming a 21 x 21 polarimetric, wide angle covariance matrix and combine using  $y = X^\dagger \Sigma_X X$  where  $\Sigma_X$  is the wide angle covariance matrix.
- *Algorithm 6:* Combine the three polarimetric images at different aspect angles using the Span and then combine these seven images using the WWF.
- *Algorithm 7:* Combine the three polarimetric images at different aspect angles using the Polarimetric Average and then combine these seven images using the AWWF.

Figures 64 and 65 show the resultant images formed from each algorithm.

*Algorithms 1 and 7*, which use the AWWF algorithm, have effectively highlighted the targets within the target scene by enhancing all the pixels around the targets' locations



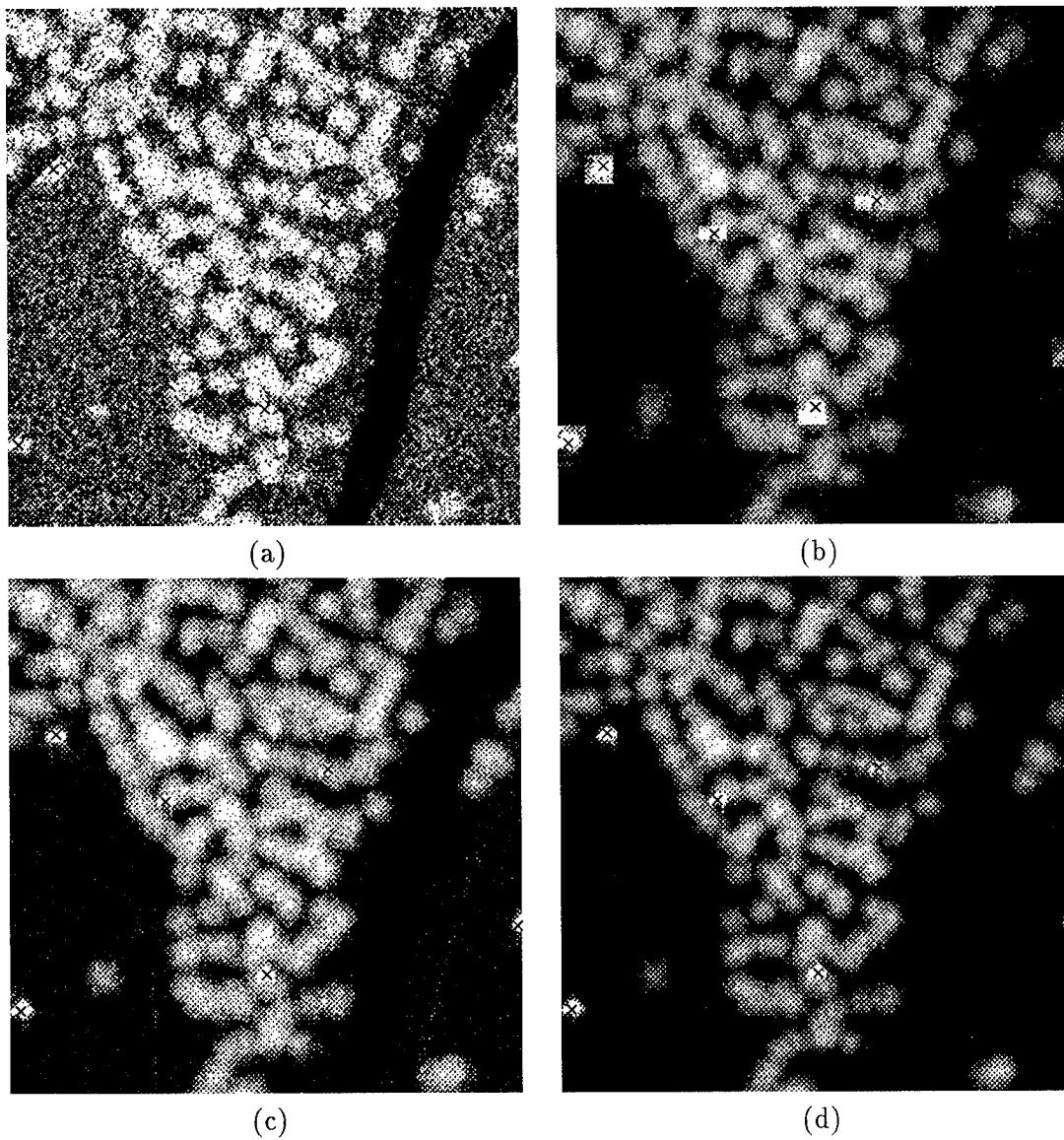


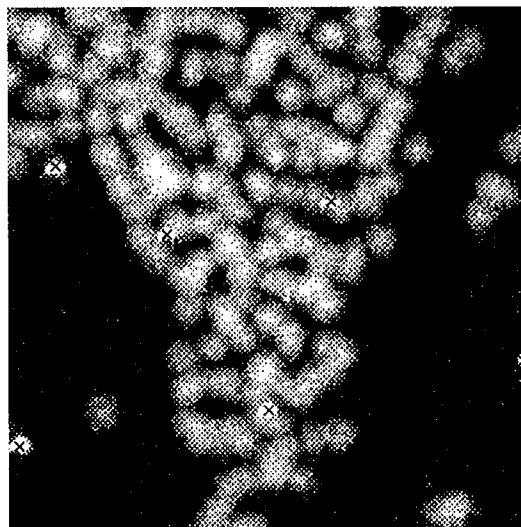
Figure 64. Images formed from Algorithms: (a) Unprocessed HH -45°, (b) 1, (c) 2, and (d) 3.



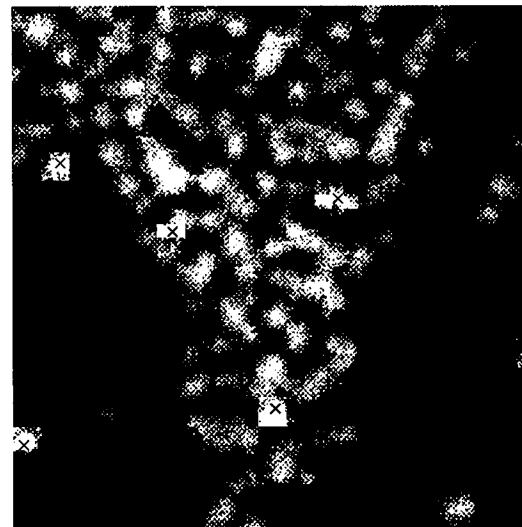
(a)



(b)



(c)



(d)

Figure 65. Images formed from Algorithms: (a) 4, (b) 5, (c) 6, and (d) 7.

Table 20. T/C ratios (dB) for the Seven Polarimetric and Wide Angle Combining Algorithms

ALG 1	ALG 2	ALG 3	ALG 4	ALG 5	ALG 6	ALG 7
29.03	25.25	27.75	25.26	14.01	24.83	30.13

(refer Figures 64(a) and 65(c)). The other algorithms have also significantly highlighted the targets compared to the unprocessed image (Figure64(a)).

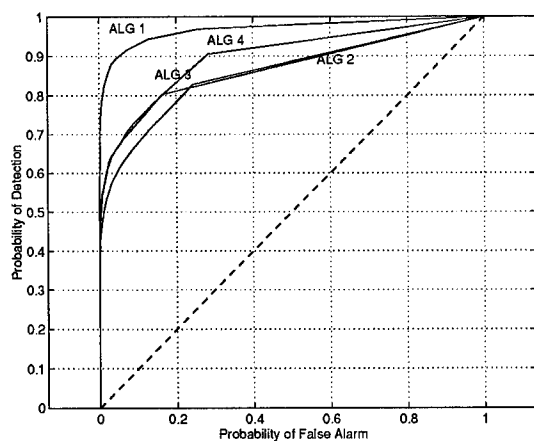
Table 20 lists the T/C ratios for each algorithm. These results show that *Algorithm 7* is the best combination, of those investigated, of polarimetric and wide angle algorithms for target detection. *Algorithm 7* provides 13.7 dB improvement in T/C ratio compared to the maximum T/C ratio of the unprocessed images ( $|HH|^2 0^\circ = 16.43$  (dB)).

Figure 66 shows plots of ROC curves for the seven algorithms. These results confirm the T/C result that *Algorithm 7* is the best method investigated of combining the 21 images for target detection purposes.

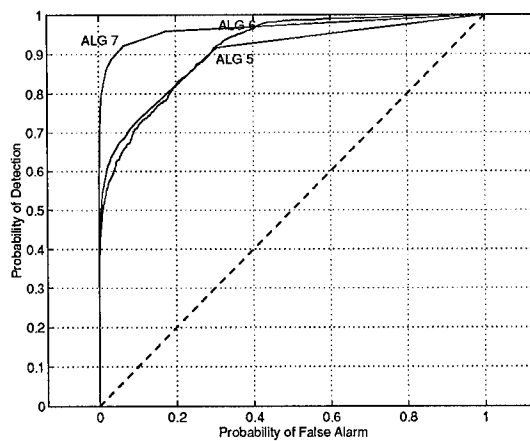
#### 4.5 Summary

In this Chapter the results of applying the XPATCH-ES WASAR data to the polarimetric and wide angle algorithms investigated by this research has been presented. From the limited amount of data analyzed the following conclusions appear to hold:

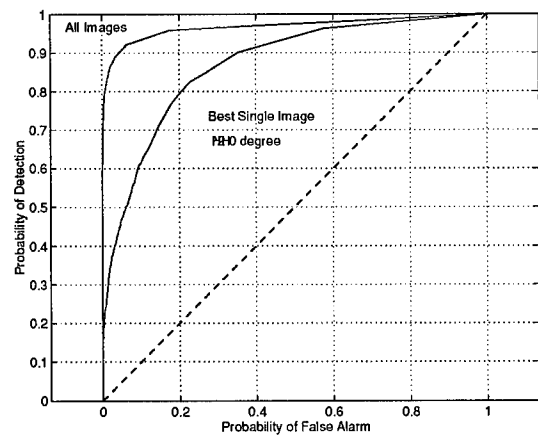
- Wide angle processing provides superior target detection performance to polarimetric processing.
- The AWWF algorithm, developed during the course of this research, proved to be an effective method of combining multi aspect images for target detection.



(a)



(b)



(c)

Figure 66. ROC Curves for: (a) Algorithms 1, 2, 3 and 4, (b) Algorithms 5, 6 and 7 (c) Comparison between best unprocessed image ( $|HH|^2 0^\circ$ ) and Algorithm 7

- As expected, using more polarimetric and wide angle images increased target detectability. For example, the maximum T/C ratio for one image was 16.43 dB, using 21 images the T/C ratio increased to 30.13 dB, a processing gain of 13.7 dB. This result justifies further research into WASAR and reinforces the need for a radar system that provides the capability of multiple looks at a target scene.
- The standard deviation and 2-D correlation co-efficient features effectively discriminate targets from clutter false alarms.

## *V. Conclusion and Recommendations*

### *5.1 Introduction*

In this thesis target detection methods were investigated to detect ground targets embedded in clutter using WASAR images. Chapter II provides the theoretical background and the method. Chapter III presents a statistical analysis and feature extraction of the XPATCH-ES data. Chapter IV provides the results obtained for polarimetric algorithms, wide angle algorithms and combinations of both. This chapter summarizes the results of this research and provides suggestions for future work in this area. From the limited amount of data analyzed the following conclusions appear to hold.

### *5.2 Summary of Results*

*5.2.1 Statistical Analysis.* The statistical analysis provided the following significant results. First, the wide angle covariance analysis showed that the relative return strength for clutter was constant at different aspect angles, whereas the returns from the targets varied considerably at different aspect angles. That is, a tree looks the same at different aspect angles, however, a target looks considerably different. The AWWF was formulated on this significant result. Second, the polarimetric covariance parameters of the targets were shown to be different to that of clutter. The form of the polarimetric covariance matrix of the XPATCH-ES data was in line with published results [15]. Finally, it was shown that the standard deviation of target pixel intensities is significantly larger than for clutter. This characteristic is useful as a discriminating feature.

*5.2.2 Feature Extraction.* The feature extraction investigated the properties and attributes of the XPATCH-ES data that effectively separate targets from clutter false alarms. In particular, it was shown that the standard deviation and the 2-D correlation coefficient were good discriminating features. Using these features a simple discriminator was designed to test the polarimetric and wide angle algorithms.

*5.2.3 Clutter Models.* Gaussian, Rayleigh and Weibull clutter models were developed and generated. Generating clutter of different distributions is useful for testing and digitally simulating target detection systems in different types of terrain. It was shown that a clutter model will be a good fit for SAR clutter if the model parameters, such as the distribution, mean and variance are set to those values obtained from a statistical analysis of actual SAR clutter scenes.

*5.2.4 Polarimetric Processing.* Polarimetric processing provided the following results. First, the polarimetric average algorithm proved to be the best method of combining the polarimetric images. This algorithm is successful as it computes the variance of the polarimetric pixel intensities (i.e.  $\text{polarimetric average} = \frac{1}{3} \sum_{i=1}^3 |x_i|^2$ ), and it was shown through a statistical analysis of the XPATCH-ES data that the variance is an effective discriminating feature. Second, the PWF algorithm formed the minimum speckled image. Finally, the PWF, SPAN and POW algorithms effectively combined the polarimetric images and significantly reduced clutter false alarms in the discriminator.

*5.2.5 Wide Angle Processing.* The wide angle processing provided the following significant results. First, the AWWF algorithm developed during the course of this

research, and based on a statistical analysis of the XPATCH-ES data, proved to be an effective method of combining multi aspect angle images for target detection. Second, the WWF also formulated during the course of this research and based on a statistical analysis of the data, effectively combined wide angle images and increased target detectability. Finally, wide angle processing provided superior target detection performance to polarimetric processing.

*5.2.6 Combinations of Polarimetric and Wide Angle Algorithms.* It was shown that by using the polarimetric average algorithm (the best polarimetric algorithm) together with the AWWF (the best wide angle algorithm) provided the best combination (of those investigated) of the 21 XPATCH-ES images. Using this amalgamation resulted in a significant improvement in T/C ratio and target detectability (using ROC curves) over the unprocessed images.

### *5.3 Conclusion*

The results obtained in this thesis lead to the following conclusions:

- Wide Angle processing provides superior target detection performance to that of polarimetric processing.
- The additional information provided by polarimetric images at multiple aspect angles justifies the requirement for a target detection system that provides the capability of multiple looks at a target scene in a single flyover.

With these conclusions, this thesis meets the five objectives outlined in Section 1.2



#### 5.4 *Recommendations for Future Research*

The following suggestions are listed for future work in this research.

- Use non-parametric techniques to estimate target and clutter pdfs (i.e. Parzen or K-nearest neighbors techniques).
- Derive ML estimates of polarimetric and wide angle covariance matrices.
- Investigate spatial PWF, WWF and AWWF algorithms.
- Investigate the use of fractal dimensions as a discriminating feature.
- Derive mathematical form of wide angle covariance matrix.
- Prove the form (i.e. diagonal matrix with varying diagonal elements) of the target wide angle covariance matrix with actual multi-aspect image SAR data.
- Generate correlated Gamma and Weibull distributed clutter.
- Form adaptive WACM from immediate pixels rather than from non-overlapping windows.
- Branch into target recognition using WASAR data.
- Use WASAR features in clustering algorithms (Neural Networks)
- Use diagonal elements of WACM as a discriminating feature
- Validate WASAR data.
- Investigate the performance of the AWWF in man made clutter.
- Investigate the distribution of XPATCH-ES clutter at different grazing angles.

- Use the different frequency option in XPATCH-ES to generate images of a target scene at different frequencies and form Frequency covariance matrix.
- Derive multi frequency algorithms (i.e. FWF Frequency Whitening Filter)
- Combine Frequency, multi aspect angles and polarizations.
- Determine best type of Radar system to have i.e multi aspect angle or variable frequency.
- Analyze the target, tree and clutter combined polarimetric and wide angle covariance matrix ( $21 \times 21$ ) to determine if a unique form exists that distinguishes the target from the clutter covariance matrices.

## Appendix A. Matlab Code

This Appendix contains the Matlab code.

*Note: All print statements removed*

### \*\*\*\*FUNCTIONS\*\*\*\*

#### Standard Deviation to mean - Function

```
%*****  
% This function calculates the standard deviation  
% to mean ratio of an input matrix y  
% The input matrix must be a matrix of intensities.  
% That is  $y = |x|^2$   
% Output: sm a ratio
```

```
function [sm] = stom(y)  
y=normalize(y);  
sm=(std2(y)/mean2(y));
```

#### Polarimetric Average - Function

```
function [average] = ave(hh,hv,vv)  
average = ((hh.*conj(hh)) + (hv.*conj(hv)) + (vv.*conj(vv)))/3;
```

#### Polarimetric Span - Function

```
function [sp] = span(hh,hv,vv)  
  
sp = abs(hh).^2 + 2*(abs(hv).^2) + abs(vv).^2;
```

#### Optimally Weighted Algorithm - Function

```
function [y] = pow(hh,hv,vv)  
  
n=length(hh);  
sigma=1/(n*n)*sum(sum(hh.*conj(hh)));  
epsilon=(1/(n*n)*sum(sum(hv.*conj(hv))))/sigma;  
gamma=(1/(n*n)*sum(sum(vv.*conj(vv))))/sigma;  
rho=(1/(n*n)*sum(sum(hh.*conj(vv))))/sqrt((sigma^2)*gamma);  
k1=(1+abs(rho^2))/epsilon;  
k2=1/gamma;  
y = (hh.*conj(hh)) + k1*(hv.*conj(hv)) + k2*(vv.*conj(vv));
```

#### Polarimetric Whitening Algorithm function

```

function [y] = pwf(hh,hv,vv)
n=length(hh);
sigma=1/(n*n)*sum(sum(hh.*conj(hh)));
epsilon=(1/(n*n)*sum(sum(hv.*conj(hv))))/sigma;
gamma=(1/(n*n)*sum(sum(vv.*conj(vv))))/sigma;
rho=(1/(n*n)*sum(sum(hh.*conj(vv))))/sqrt((sigma^2)*gamma);
k1 = 1/(sigma * (1 - (abs(rho))^2));
k2 = 1/(sigma * epsilon);
k3 = 1/(sigma * (1 - (abs(rho))^2) * gamma);
k4 = (2 * abs(rho))/(sigma * (1 - (abs(rho))^2) * sqrt(gamma));

y = k1*(hh.*conj(hh)) + k2*(hv.*conj(hv)) + k3*(vv.*conj(vv))...
    - k4*(abs(hh).*abs(vv).*cos(angle(hh)-angle(vv)-angle(rho)));

%function computes the polarimetric covariance
%matrix.
%Input - 3 matrices hh, hv, vv
%Output - covm covariance matrix normalized to C(1,1)
% - rho correlation coefficients

function[covmat,rho]=covm(hh,hv,vv);
%%%%%%%%%%%%%%%%%%%%%%%%%%%%%%%%%%%%%%%%%%%%%%%%%%%%%%%%%%%%%%%%%%%%%%%%
[m,n]=size(hh);
rho=zeros(3,3);
X(:,1)=reshape(hh,n*m,1);
X(:,2)=reshape(hv,n*m,1);
X(:,3)=reshape(vv,n*m,1);
covariance=cov(X);

covmat=covariance./covariance(1,1)
c=abs(covariance);
for i=1:length(c)
for j=1:length(c)
rho(i,j)=(c(i,j)/sqrt(c(i,i)*c(j,j)));
end
end
return;
%%%%%%%%%%%%%%%%%%%%%%%%%%%%%%%%%%%%%%%%%%%%%%%%%%%%%%%%%%%%%%%%%%%%%%%%

% Function generates either the pwf or the wwf
% depending on input matrices.
% Calls - pcm which forms the covariance matrix
% Inputs - three images (nxn matrices)
% Output - pwf image or 3 angle wwf

```

```

%*****
function [y] = pwfc(hh,hv,vv)

[C,r]=pcm(hh,hv,vv);
C=abs(C);
[m,n]=size(hh);
for i=1:m
for j=1:n
x=[abs(hh(i,j)),abs(hv(i,j)),abs(vv(i,j))];
y(i,j)=x*inv(C)*conj(x');

end
end
return;

%*****
% Function that computes the AWWF image
% Inputs - 7 images and window size

function[y] =awwf(a1,a2,a3,a4,a5,a6,a7,win);
%
%

a1=a1(1:361,1:361);
a2=a2(1:361,1:361);
a3=a3(1:361,1:361);
a4=a4(1:361,1:361);
a5=a5(1:361,1:361);
a6=a6(1:361,1:361);
a7=a7(1:361,1:361);

y1=zeros(360,360);
for i=1:win:360
for j=1:win:360
temp1=a1(i:i+win,j:j+win);
temp2=a2(i:i+win,j:j+win);
temp3=a3(i:i+win,j:j+win);
temp4=a4(i:i+win,j:j+win);
temp5=a5(i:i+win,j:j+win);
temp6=a6(i:i+win,j:j+win);
temp7=a7(i:i+win,j:j+win);
y(i:i+win,j:j+win)=awwf1(temp1,temp2,temp3,temp4,temp5,temp6,temp7);
end

```

```

end

% Program calculates image using all 21 polarimetric and wide
% angle algorithms

load rotcmplx;
% rotcmplx contains the 21 images different poles and aspect angles
[m,n]=size(a1);

for i=1:21
X(:,i)=reshape(eval(['a' num2str(i)]),n*m,1);
end

C=cov(X)
for i=1:m
for j=1:n
x=[a1(i,j),a2(i,j),a3(i,j),a4(i,j),a5(i,j),a6(i,j),a7(i,j),
    a8(i,j),a9(i,j),a10(i,j),a11(i,j),a12(i,j),a13(i,j),a14(i,j),
    a15(i,j),a16(i,j),a17(i,j),a18(i,j),a19(i,j),a20(i,j),a21(i,j)]';
xhat=conj(x');
y(i,j)=xhat*inv(C)*x;

end
end

% Function generates either the pwf or the wwf
% depending on input matrices.
% Calls - pcm which forms the covariance matrix
% Inputs - three images (nxn matrices)
% Output - pwf image or 3 angle wwf
%*****
function [y] = awwf1(a1,a2,a3,a4,a5,a6,a7)

[C,r]=wacm(a1,a2,a3,a4,a5,a6,a7);
C=abs(C/max(max(C)));
[m,n]=size(a1);
for i=1:m
for j=1:n
x=[(a1(i,j)),(a2(i,j)),(a3(i,j)),(a4(i,j)),(a5(i,j)),(a6(i,j)),(a7(i,j))];
y(i,j)=x*((inv(C))*conj(x'));

end
end
return;
%This function plots the cdf of a vector of rv's

```

```

function[cum]=cdf(x);

[m,n]=size(x);
bins=floor(min(x)).01:ceil(max(x));
[datr,b]=hist(real(x),bins);
datr=datr/(sum(datr));
[m,n]=size(datr);
A=ones(n,n);
A=tril(A);
cum=A*datr';

%This function computes the sample correlation coefficient

function[rho]=corr_coef(x,y)

mean_x=mean(x);
mean_y=mean(y);
denom=sqrt(sum((x-mean_x).^2)*sum((y-mean_y).^2));
rho=sum((x-mean_x).*(y-mean_y))/denom;
return;

%% FUNCTION detect.m
%This function detects possible targets that exceed the threshold
%The function returns an array that contains the targets co-ordinates.

function [target]=detect(Image,T)

Image=abs(Image);
mean_I=mean(mean(Image));
std_I=std(Image(:));
[m,n]=size(Image);
Window=10; %Determines the resolution of targets
wm=3; %wm & wn is a sub-window that is used to improve processing time
wn=3;
x=1;
%thrsh=T*std_I+mean_I
thrsh=T
if wm>1
for i=1:wm:m-wm
for j=1:wn:n-wn

if (Image(i:i+wm,j:j+wn)<=thrsh)
else

```

```

target(x,1)=i+ceil(wm/2);
target(x,2)=j+ceil(wn/2);
x=x+1;
end
end
end
%%

else [target(:,1),target(:,2)]=find(Image>=thrsh);
end
a=target;
for j=1:length(target)
x=0;
sum1=0;
sum2=0;
for i=1:length(target)
if (target(i,1)>a(j,1)-Window)&(target(i,1)<a(j,1)+Window)&(target(i,2)
>a(j,2)-Window)& (target(i,2)<a(j,2)+Window)
x=x+1;
sum1=sum1+target(i,1);
sum2=sum2+target(i,2);
end
end
target(j,1)=ceil(sum1/x);
target(j,2)=ceil(sum2/x);
end

for j=1:length(target)
for i=1:length(target)
if target(i,1)>=target(j,1)-Window&target(i,1)<=
target(j,1)+Window&target(i,2)>=target(j,2)-Window&
target(i,2)<=target(j,2)+Window&i~=j
target(j,1)=0;
target(j,2)=0;
end
end
end

target=target(find(target(:,1)>0&target(:,2)>0),:);
%*****

%*****
%      FUNCTION display.m
%*****
% Purpose: Log encodes the image, scales, and adjusts the intensity of

```



```

%      the image for display purposes.
%
% Called by: display1.m
%
% Quirks:
%   1) Intensity adjustments are hard-coded.
%
% NOTE:
%   MatLab displays the images as transposes, x and y coordinates are
%   reversed. In order to correct this so that target coordinates could
%   be plotted over the image and match, the image is transposed just
%   before displaying.
%
%*****

function display(X,fig,autoscale)

% Converting to dB and scaling
X = 20*log10(abs(X));

% Selecting maximum and minimum
if autoscale <= 0 % images are clipped at -50 and 20 dB
    minimum = -50;
    maximum = 20;
elseif autoscale == 1 % images are ranged between max and min pixels
    minimum = min(min(X));
    maximum = max(max(X));
end

% scaling
range = abs(maximum - minimum);
if range ~= 0
    X = round(((X - minimum)/range)*255);
else
    X = 0 * ones(size(X,1),size(X,2));
end

% clipping out of range values
if autoscale == 0
    [i,j] = find(X<0);
    for k = 1 : length(i)
        X(i(k),j(k)) = 0;
    end
    [i,j] = find(X>255);
    for k = 1 : length(i)

```

```

        X(i(k),j(k)) = 255;
    end
end

% correcting for Matlabs imaging axis transposition
X = X';

% Display image
figure(fig)
set(fig,'PaperPosition',[1,3,6,5.75],'NextPlot','new')
hold on
axis('xy','off')
colormap(gray)
if autoscale == 0
    image(X-75)
elseif autoscale == 2
    image(X-160)
elseif autoscale == -1
    image(X-150)
elseif autoscale == 1
    image(X-115)
elseif autoscale == -2
    image(X-50)
elseif autoscale == -3
    image(X-25)
elseif autoscale == -4
    image(X)
elseif autoscale == -5
    image(X+50)
elseif autoscale == -6
    image(X+75)

end
    hold off
axis('equal');
%*****

%Function plots different features enter image and window size

function[cor] =feature(Image>windowr>windowc);
%
%-----
%%%%%%%%%%%%%%%%%%%%%%%%%%%%%%%%%%%%%%%%%%%%%%%%%%%%%%%%%%%%%%%%%%%%%%%%
Image=abs(Image)./max(max(abs(Image)));

```

```

thrsh=mean2(Image)+std2(Image);
diim=dimage(Image,thrsh);

tvd=ones(windowr+1>windowc+1);

[m,n]=size(Image);
window=10; % Size of area surrounding targets
k=0;
for i=1>windowr:m>windowr
for j=1>windowc:n>windowc
k=k+1;
temp=Image(i:i>windowr,j:j>windowc);
%aa=zeros(windowr+1>windowc+1);
%[m,n]=find(temp>thrsh);
%aa(m,n)=temp(m,n);

temp1=diim(i:i>windowr,j:j>windowc);
cor(k)=corr2(tvd,temp1);
meanv(k)=median(median(temp));
stdv(k)=std2(temp);
hh(k)=mean2(temp.*conj(temp));
end
end

figure
plot(stdv,cor,'*')
ylabel('Feature 1 - Correlation Coef');
xlabel('Feature 2 - STD');
return

%%%%%%%%%%%%%%%%%%%%%%%%%%%%%%%%%%%%%%%%%%%%%%%%%%%%%%%%%%%%%%%%%%%%%%%%

function[clut] =gauss_clut(var,size);
%
%Simple Gaussian distributed clutter generator
%Inputs var - Variance of the noise
% size - size of clutter matrix required
%Output clutt - Gaussian Clutter (noise)

clut=sqrt(var)*(randn(size,size));
%complex Gaussian clutter
%cclut=sqrt(var)*(randn(size,size)+j*randn(size,size));
return
%Function gets clutter pixels

```

```

function[clutter] =get_targets(Image,xx1);
%
%

[tm,tn]=size(xx1);

Windowr=7; % Size of area surrounding targets
Windowc=4;
for i=1:tm
x=xx1(i,1);
y=xx1(i,2);
Image(x-Windowr:x+Windowr,y-Windowc:y+Windowc)=zeros((2*Windowr)+1,
                                                    (2*Windowc)+1);

end
clutter=(Image(find(Image~=0)));
return;

function[target] =get_targets(Image,xx1);
%
%

[tm,tn]=size(xx1);

Windowr=7; % Size of area surrounding targets
Windowc=4;
for i=1:tm
x=xx1(i,1);
y=xx1(i,2);
targ_matrix=Image(x-Windowr:x+Windowr,y-Windowc:y+Windowc);
targ=targ_matrix(:);
target=[target;targ];
end
return;

%program displays truth maps

fid=fopen('/home/marconi1/data/xpatches/gs_000_d45_gnd.bytxt');
gnd=fread(fid);
gnd=reshape(gnd,512,512);
display(gnd,1,0);
title('Ground Truth Map of gs_000_d45');
%print ground -deps

%plots direct histogram of the amplitude of the pixel intensity of targets

```

and clutter

```
function [] = histt(Image, target_loc, Maxx)

Image = abs(Image) ./ abs(max(max(Image)));

%Extract targets and form target vector
targets = get_targ(Image, target_loc);
%form clutter vector
clutter = get_clut(Image, target_loc);
[yc, xc] = hist(clutter, 150);
[yt, xt] = hist(targets, 150);
yc = yc ./ sum(yc);
yt = yt ./ sum(yt);
xc = [0, xc];
yc = [0, yc];
xt = [0, xt];
yt = [0, yt];

Maxyc = 1.1 * max(yc);
Maxyt = 1.1 * max(yt);
if Maxyc > Maxyt
    Maxy = Maxyc;
else
    Maxy = Maxyt;
end

figure
axis1 = axis;

hold on
plot(xc, yc, '-.');
plot(xt, yt);
hold off
%title('Plot of Target and Clutter pdfs -
        (cmplx - all angle pwf)');
axis([-0.001, Maxx, axis1(3), Maxy])
ylabel('Probability')
xlabel('Threshold')
legend('Clutter', 'Targets')
grid

function [image] = normalize(image)
image = abs(image) ./ max(max(abs(image)));
```

```

return;

%function computes the polarimetric covariance
%matrix.
%Input - 3 matrices hh, hv, vv
%Output - covm covariance matrix normalized to C(1,1)
% - rho correlation coefficients

function[covariance,rho]=covm(hh,hv,vv);
%%%%%%%%%%%%%%%%%%%%%%%%%%%%%%%%%%%%%%%%%%%%%%%%%%%%%%%%%%%%%%%%%%%%%%%%
[m,n]=size(hh);
rho=zeros(3,3);
X(:,1)=reshape(hh,n*m,1);
X(:,2)=reshape(hv,n*m,1);
X(:,3)=reshape(vv,n*m,1);
covariance=cov(X);
covariance(1,1);
covmat=covariance./covariance(1,1);
c=abs(covariance);
for i=1:length(c)
for j=1:length(c)
rho(i,j)=(c(i,j)/sqrt(c(i,i)*c(j,j)));
end
end
return;
%%%%%%%%%%%%%%%%%%%%%%%%%%%%%%%%%%%%%%%%%%%%%%%%%%%%%%%%%%%%%%%%%%%%%%%%
%% FUNCTION pdpfa determine hits and misses

function [No_hits,No_false_alarms]=pdpfa(Targets,Detections)

%*****Calculation of #hits & #False Alarms*****

[m,n]=size(Targets);
[mm,nn]=size(Detections);
Window=8;
No_hits=0;
for i=1:mm
for j=1:m
if ((Detections(i,1)>Targets(j,1)-Window)&
(Detections(i,1)<Targets(j,1)+Window)
&(Detections(i,2)>Targets(j,2)-Window)&
(Detections(i,2)<Targets(j,2)+Window))
No_hits=No_hits+1;

```

```

        else
    end
end
end
No_false_alarms=mm-No_hits;

%This function computes the pixel to pixel
correlation within an image

function[e]=pix_corr(Image,ws)

[th,Image]=cart2pol(real(Image),imag(Image));

x=Image(1:ws,1:ws);
x=reshape(x,1,ws*ws);

for i=1:ws
for j=1:ws
y=Image(i:ws-1+i,j:ws-1+j);
y=reshape(y,1,ws*ws);
e(i,j)=corrcoef(x,y);
end
end

%This function forms the pixel to pixel covarinace matrix

function[cov,X]=pix_cov(x)

[m,n]=size(x);
size_cov=9;
shift=3;
k=0;

for i=1:shift
for j=1:shift
k=k+1;
z=x(i:m-shift+i,j:n-shift+j);
eval(['X' num2str(k) ' = z;']);
end
end

for i=1:size_cov
for j=1:size_cov
y=eval(['X' num2str(i)]);

```

```

z=eval(['X' num2str(j)]);
y=reshape(y,1,(m-shift+1)*(n-shift+1));
z=reshape(z,1,(m-shift+1)*(n-shift+1));
X(:,i)=y';
cov(i,j)=mean(y.*conj(z));
end
end

function [y] = pwfc(hh,hv,vv)

Covariance_Matrix=0.086*[1,0,0.53;0,0.19,0;0.53,0,1.03];
[m,n]=size(hh);
for i=1:m
for j=1:n
x=[hh(i,j),hv(i,j),vv(i,j)];
y(i,j)=x*inv(Covariance_Matrix)*x';

end
end

%Polarimetric matched filter requires 3 polarimetric or wide angle
% images and Calls - pcmtc - generates pcm or wacm (3 angle);
% Inputs - 3 images (nxn matrix) xx1 target locations
% Output - Either pmf image or 3 angle wmf image
%*****

function [y] = pmf(hh,hv,vv,xx1)

%form covariance matrix
[Cc,Ct]=pcmtc(hh,hv,vv,xx1)
y=abs(inv(Cc)*Ct);
[V,D]=eig(y)
A=max(max(D))
[m,n]=find(D==A)
h=(V(:,m))

[m,n]=size(hh);
for i=1:m
for j=1:n
x=[hh(i,j),hv(i,j),vv(i,j)];
y(i,j)=x*conj(h);

end
end

```



```

%*****
function[clut] =rayl_clut(var,size);
%
%Simple Gaussian distributed clutter generator
%Inputs var - Variance of the noise
% size - size of clutter matrix required
%Output clutt - Gaussian Clutter (noise)

a=sqrt(var)*(randn(size,size));
b=sqrt(var)*(randn(size,size));
clut=sqrt(a.^2+b.^2);
return
function rerror=re(datat,data)

norma=norm(datat,'fro');
normb=norm(data,'fro');
data=data*(norma/normb);

rerror=norm(datat-data,'fro')/norm(datat,'fro');

% Function computes ROC curves for target and clutter
% Input - Image to be tested and target locations
% Output - provides plot of Pd Vs Pfa

function []=roc(Image,target_loc)

% Normalize so that pixel intensities range from 0 to 1
Image=abs(Image)./max(max(abs(Image)));

clutter=get_clut(Image,target_loc);
targets=get_targ(Image,target_loc);

pixel_bins=[0:.0001:.02,.02:.001:1];
[n1,x1]=hist(clutter,pixel_bins);
[n2,x2]=hist(targets,pixel_bins);
xcn=[0 x1]./max(x2);
clut=[0 n1]./sum(n1);
xtn=[0 x2]./max(x2);
targ=[0 n2]./sum(n2);
chance=0:.1:1;
p_fa=zeros(length(pixel_bins)+1,1);
p_d=zeros(length(pixel_bins)+1,1);
for i=1:length(pixel_bins)+1
    p_fa(i)=sum(clut(i:length(clut))));

```

```

        p_d(i)=sum(targ(i:length(targ)));
    end
%figure
%if flag==1
%plot(p_fa,p_d,'-.')
%else
plot(p_fa,p_d);
%end
axis([0 1 0 1])
axis('equal')
hold on
plot(chance,chance,'r--')
xlabel('Probability of False Alarm')
ylabel('Probability of Detection')
grid
return;

```

```

function var=snr(signal,snr_d)

```

```

[m,n]=size(signal);
sig_power=((norm(signal,'fro')^2)/(n*m));
noise_power=10*log10(sig_power)-snr_d;
var=10^(noise_power/10)

```

```

%*****
% This function calculates the t/c ratio of a matrix
% Input must be a matrix of intensities.
% Inputs - Image and targets (matrix containing target coordinates)
% Output - target to clutter ratio in dB (tc)
%*****

```

```

function [tc] = ttoc(Image,targets)
Image=normalize(Image);
t=get_targ(Image,targets);
c=get_clut(Image,targets);
tm=mean(t);
cm=mean(c);
tc=10*log10(tm)-10*log10(cm);
return;

```

```

% This function computes the Wide Angle Covariance Matrix (WACM);
% Input: 7 matrices at different aspect angles (a1 ....)
% Output: Covariance matrix (c) normalized to 0 degree return

```

```

% and rho - correlation coefficients

function[covariance,rho] = wacm(a1,a2,a3,a4,a5,a6,a7)

[m,n]=size(a1);

for i=1:7
X(:,i)=reshape(eval(['a' num2str(i)]),n*m,1);
end

covariance=cov((X));
covariance(4,4);
covariance=covariance./covariance(4,4);

c=abs(covariance);
for i=1:length(c)
for j=1:length(c)
rho(i,j)=(c(i,j)/sqrt(c(i,i)*c(j,j)));
end
end
return;
%%%%%%%%%%%%%%%%%%%%%%%%%%%%%%%%%%%%%%%%%%%%%%%%%%%%%%%%%%%%%%%%%%%%%%%%

function [average] = wave(a,b,c,d,e,f,g)

average = ((a.*conj(a)) + (b.*conj(b)) + (c.*conj(c)) +
(d.*conj(d))+(e.*conj(e)) + (f.*conj(f)) + (g.*conj(g)))/7;

%*****

%function uses ffts to calculate cross convolution (biased)

function Cxx =zcorr2(X,Y)

[m,n]=size(X);

%determine correct length for fft

lx = 2*m;
lxb2 = log10(lx)/log10(2);
fftsz = 2^ceil(lxb2);

%flip the Y matrix for correlation

```

```

Y=fliplr(Y);
Y=flipud(Y);

fx=fft2(X,fftsz,fftsz);
fy=fft2(Y,fftsz,fftsz);

disp('Calculate fc')

fc=fx.*fy;
Cxx=ifft2(fc);
Cxx=Cxx(1:2*m-1,1:2*m-1);

%mesh(abs(Cxx))

%function [data]=weibull(data,b,alpha)

alpha=1;
b=1.5;
x=rand(400,400);
F=(alpha*(-log(x))).^(1/b);
%data=data+F;

figure
hist(F(:),50)
title(['Histogram of Weibull r.v,nu = ',
,num2str(b),', eta=',num2str(alpha)])
ylabel('Number in bin - Frequency')
xlabel('x')
print histweib -deps

function[]=histt(Image,targets,fig)
[tm,tn]=size(targets);
Window=5; % Size of area surrounding targets
%Form target vector
for i=1:tm
x=targets(i,1);
y=targets(i,2);
targ_win=Image(x-Window:x+Window,y-Window:y+Window);
targ=targ_win(:);
target=[target;targ];

```

```

end
%Extract targets from image
for i=1:tm
x=targets(i,1);
y=targets(i,2);
Image(x-Window:x+Window,y-Window:y+Window)=
zeros((2*Window)+1,(2*Window)+1);
end
Image=abs(Image(find(Image~=0)));
bins1=.000001:.1:3;
%histogram clutter pixels
[datr1,b1]=hist(abs(Image),bins1);
datr1=datr1/(sum(datr1));
datr1=datr1(1:(length(datr1))-1);
b1=b1(1:(length(b1))-1);
%calculate mean and variance of clutter pixels
s1=std(log(abs(Image)));
mm1=mean(log(abs(Image)));
%plot log-normal curve over histogram
f2=(1./(sqrt(2*pi)*s1.*bins1)).*exp(-((log(bins1)-(mm1)).^2)/(2*(s1^2)));
f2=(f2.*max(datr1))./max(f2);
bins=.000001:.1:3;
[datr,b]=hist(abs(target),bins);
datr=datr/(sum(datr));
datr=datr(1:(length(datr))-1);
b=b(1:(length(b))-1);
s=std(log(abs(target)));
mm=mean(log(abs(target)));
f1=(1./(sqrt(2*pi)*s.*bins)).*exp(-((log(bins)-(mm)).^2)/(2*(s^2)));
f1=(f1.*max(datr))./max(f1);
figure(fig)
hold on
plot(bins,f1,'-.');
plot(bins1,f2);
hold off
title('Plot of Target and Clutter pdfs - (cmplx - all angle pwf)');
ylabel('Number in bin - Frequency')
xlabel('x')
legend('Targets','Clutter')
grid
%print pwfpdfs -deps

```

## Bibliography

1. (1986), Jet Propulsion Laboratory. *Shuttle Imaging Radar-C Science Plan..* Technical Report 86-29, JPL Publication, 1986.
2. Boothe, R. R. *The Weibull Distribution Applied to Ground Clutter Backscatter Coefficient.* Technical Report RE-TR-69-15, U.S Army Missile Command, Redstone Arsenal, June 1969.
3. Chaney, R. D., et al. "On The Performance of Polarimetric Target Detection Algorithms." *Proceedings of the IEEE 1990 International Radar Conference.* 520-525. May 7-10, 1990.
4. Daniel E. Kreithen, Shawn D. Halverson and Gregory J. Owirka. "Discriminating Targets from Clutter," *The Lincoln Laboratory Journal*, 6(1):25-51 (1993).
5. Fukunaga, K., editor. *Introduction to Statistical Pattern Recognition.* Boston, MA: Academic Press, inc., 1990.
6. Greenstein, L. J., et al. *A Comprehensive Ground Clutter Model for Airborne Radars.* Technical Report, ITT Institute Chicago, IL, September 1969.
7. Halverson, S. D., et al. "A Comparison of Ultra-Wideband SAR Target Detection Algorithms," *SPIE Proceedings, SPIE-2230*(1):144-157 (1994).
8. Held, D. N. "The NASA/JPL multifrequency, multipolarization airborne SAR system." *In Proceedings of the International Geoscience and Remote Sensing Symposium.* Sept 1988.
9. Holm, William A. "Applications of polarimetry to Target/Clutter Discrimination in Millimeter Wave Radar Systems," *SPIE Polarimetry: Radar, Infrared, Visible, and X-ray*, (1317):148-153 (1990).
10. Jakeman., E. and K. D. Ward. "A model for non-Rayleigh sea Clutter," *IEEE Transactions on Antennas and Propagation* (November 1976).
11. Knurr, K. *Processing of Wide-Angle Synthetic Aperture Radar Signals for Target Detection.* MS thesis, Air Force Institute of Technology, Winter 1993.
12. Lee, J. "Speckle Analysis and Smoothing of SAR Images," *Computer Graphics and Image Processing*, (17):24-32 (1981).
13. Li, J. and E. G. Zelnio. "Target Detection with Synthetic Aperture Radar and Coherent Subtraction," *SPIE Proceedings, SPIE-2230*(1):1023- 1044 (1994).
14. Novak, L. M. "Generating Correlated weibull Random Variables for digital Simulations," *In Proceedings of IEEE Decision and Control Conference, San Diego, CA*, 156-160 (1973).
15. Novak, L. M. and M. C. Burl. "Optimal Speckle Reduction in Polarimetric SAR Imagery," *IEEE Transactions on Aerospace and Electronic Systems, AES-26*(2):293-305 (March 1990).
16. Novak, L. M., et al. "Optimal Polarimetric Processing for Enhanced Target Detection," *IEEE Transactions on Aerospace and Electronic Systems, AES-29*(1):234-243 (January 1993).

17. Novak, L. M., et al. "Studies of Target Detection Algorithms That Use Polarimetric Radar Data," *IEEE Transactions on Aerospace and Electronic Systems*, AES-25(2):150-165 (March 1989).
18. Oliver, C. J. and R. J. Tough. "On the Simulation of Correlated K-Distribution Random Clutter," *Optica Acta*, 33(3):156-160 (1981).
19. Papoulis, A. *Probability, Random Variables, and Stochastic Processes*. New York: McGraw-Hill, 1984.
20. Schleher, D. C. "Radar Detection in Weibull Clutter," *IEEE Transactions on Aerospace and Electronic Systems*, AES-12(6):763-743 (July 1977).
21. Sechtn, M. B. and M. C. Burl. "Multiple Image Processing to enhance stationary target detection," *SPIE Proceedings*, SPIE-1630(1):86-97 (1992).
22. Sekine, M. and T. Musha. "A New Weibull CFAR in Radar Systems," *Proceedings of the International Symposium on Noise and Clutter Rejection in Radar and Imaging Sensors*, 573-577 (1989).
23. Skolnik, M. I. *Introduction to Radar Systems*. New York: McGraw-Hill, 1980.
24. Sullivan, R. "Polarimetric X/L/C-band SAR." *In Proceedings of the IEEE National Radar Conference*. 1988.
25. Sumner, R. *Investigation of Target Detection Methods to Detect Ground Targets in Synthetic Aperture Radar (SAR) Images*. MS thesis, Air Force Institute of Technology, Winter 1994.
26. Trunk, G. V. and S. F. George. "Detection of targets in Non Gaussian Sea clutter," *IEEE Transactions on Aerospace and Electronic Systems*, AES-6:620-628 (1970).
27. Ulaby, F. T. and M. C. Dobson, editors. *Handbook of Radar Scattering Statistics for Terrain*. Norwood, MA: Artech House, inc., 1989.

### *Vita*

Wayne Mclaggan was born in Melbourne, Australia in 1963. He completed high school at Caulfield Grammar School in Melbourne, Australia. In 1982 Wayne joined the Royal Australian Air Force. In 1984, after completing training as a radio technician, Wayne served with No. 34 Squadron (VIP Transportation), Canberra, Australia.

In 1988 he was sponsored by the RAAF to complete a Bachelor of Electronic Engineering at the University of Canberra. On graduation in 1990, Wayne received his commission as an Electrical Engineering officer in the Royal Australian Air Force.

In 1990, he was posted as a Systems Engineer to Headquarters Logistics Command (HQLC), Melbourne, Australia.

From 1992 until coming to AFIT in 1993, Wayne established a RAAF Centre of Excellence for Communications, Navigation and Electrical specifications and standards at HQLC Melbourne, Australia.

Permanent address: R&D Flight  
EWSQN ARDU  
RAAF Base Edinburgh  
South Australia



# REPORT DOCUMENTATION PAGE

Form Approved

OMB No. 0704-0188

Public reporting burden for this collection of information is estimated to average 1 hour per response, including the time for reviewing instructions, searching existing data sources, gathering and maintaining the data needed, and completing and reviewing the collection of information. Send comments regarding this burden estimate or any other aspect of this collection of information, including suggestions for reducing this burden, to Washington Headquarters Services, Directorate for Information Operations and Reports, 1215 Jefferson Davis Highway, Suite 1204, Arlington, VA 22202-4302, and to the Office of Management and Budget, Paperwork Reduction Project (0704-0188), Washington, DC 20503.

1. AGENCY USE ONLY (Leave blank)		2. REPORT DATE March 1995	3. REPORT TYPE AND DATES COVERED Master's Thesis	
4. TITLE AND SUBTITLE Investigation of Ground Target Detection Methods in Fully Polarimetric Wide Angle Synthetic Aperture Radar Images			5. FUNDING NUMBERS	
6. AUTHOR(S) Wayne B. McLaggan				
7. PERFORMING ORGANIZATION NAME(S) AND ADDRESS(ES) Air Force Institute of Technology, WPAFB OH 45433-6583			8. PERFORMING ORGANIZATION REPORT NUMBER AFIT/GE/ENG/95M-02	
9. SPONSORING/MONITORING AGENCY NAME(S) AND ADDRESS(ES) Mike Bryant WL-AARA Wright Patterson AFB, OH 45433-7318			10. SPONSORING/MONITORING AGENCY REPORT NUMBER	
11. SUPPLEMENTARY NOTES				
12a. DISTRIBUTION / AVAILABILITY STATEMENT  Unlimited			12b. DISTRIBUTION CODE	
13. ABSTRACT (Maximum 200 words)				
Abstract				
<p>Target detection is a high priority of the Air Force for the purpose of reconnaissance and bombardment. This research investigates and develops methods to distinguish ground targets from clutter (i.e. foliage, landscape etc.) in Wide Angle Synthetic Aperture Radar (WASAR) images. WASAR uses multiple aspect angle SAR images of the same target scene. The WASAR data was generated from a pre-release software package (XPATCH-ES) provided by the sponsor (WL-AARA). A statistical analysis and feature extraction is performed on the XPATCH-ES data. Polarimetric and wide angle covariance matrices are estimated and analyzed. From an analysis of the wide angle covariance matrix it is shown that natural clutter has in general a uniform radar return for changing aspect angles, whereas the radar return for a target varies. Based on this analysis, two new wide angle algorithms, the WASAR Whitening Filter and the Adaptive WASAR Whitening Filter (AWWF) are developed. The target detection performance of polarimetric and multi aspect angle image combining algorithms are quantified using Receiver Operating Characteristic curves and target to clutter ratios. It is shown that wide angle processing provides superior target detection performance over polarimetric processing. Combinations of wide angle and polarimetric algorithms were used to achieve a 13.7 dB processing gain in target to clutter ratio when compared to unprocessed images of the target scene. This represents a significant improvement in target detection capabilities.</p>				
14. SUBJECT TERMS Wide Angle Synthetic Aperture Radar, Target Detection, Polarimetric SAR Images			15. NUMBER OF PAGES 179	
			16. PRICE CODE	
17. SECURITY CLASSIFICATION OF REPORT UNCLASSIFIED	18. SECURITY CLASSIFICATION OF THIS PAGE UNCLASSIFIED	19. SECURITY CLASSIFICATION OF ABSTRACT UNCLASSIFIED	20. LIMITATION OF ABSTRACT UL	